Abstract Book

ELyT Workshop 2026

Celebrating 10 Years of ELyTMaX & ELyT Global !

March 7-8, 2026

Extended Education & Research Building,

Tohoku University

Sendai, Japan

ELyT Workshop 2026

March 7-8, 2026 – Sendai, Japan

Celebrating 10 Years of ELyTMaX & ELyT Global !

General Program and Information

Saturday, March 7

8:30	9:00	Registration
9:00	9:10	Opening
9:10	10:25	Session 1
10:25	10:45	Break
10:45	12:00	Session 2

12:00	14:30	Poster session & Lunch

14:30	16:00	Session 3
16:00	16:20	Break
16:20	17:35	Session 4

18:30	20:00	Banquet

Sunday, March 8

9:00	10:45	Session 5
10:45	11:05	Break
11:05	12:35	Session 6
12:35	12:50	Closing

12:50	14:00	Lunch

14:00		Excursion (Optional)

Information for Poster Presenters:

- Poster size: A0
- Setup: **Morning of Saturday, March 7**, at the Meeting Room, 2nd Floor of IFS Building 1 (https://www.tohoku.ac.jp/map/en/?f=KH_C09)
  * Please bring your poster to the Meeting Room and display it in the provided poster frames.
- The posters will also be exhibited at the anniversary ceremony on Monday, March 9.

Venue

Registration & Oral Sessions

Extended Education & Research Building

6th Floor, Lecture Room A

https://www.tohoku.ac.jp/map/en/?f=KH_C07

*** Coffee Service (Bottles with lids only) ***

Located in the registration area.

Please note that food and drinks are prohibited in the Lecture Room A, unless they are in a bottle with a lid.

Poster Session & Lunch

IFS Building 1

2nd Floor, Meeting Room

https://www.tohoku.ac.jp/map/en/?f=KH_C09

***Banquet** (18:30-20:00 on Saturday)*

PICKS

* 10 min walk from Katahira Campus.

https://maps.app.goo.gl/nxK9zwN7DtN5N1VE8

(Optional) Excursion

Meeting Place and Time:

14:00 at the 1st Floor Entrance Hall, Extended Education & Research Building (Workshop Venue)

Option 1: Kokeshi Doll Painting Experience

Paint your own original Kokeshi doll, a famous traditional craft of the Tohoku region.

Location: Kokeshi no Shimanuki (10-minute walk (one-way) from Katahira Campus)
Fee: 1,000 JPY (Including materials) *Please pay on-site via cash or credit card.
Website: https://www.sentabi.jp/en/tours/1914

Option 2: Sendai Castle Ruins Walking Tour
Visit the historic site of Lord Date Masamune's fortress and enjoy a panoramic view of the city. * In case of heavy rain or snow, the event will be canceled.
Location: Sendai Castle Ruins (30-minute uphill walk (one-way) from Katahira Campus)
Fee: Free (Optional museum entry: 770 JPY)
Website: https://www.sentabi.jp/spots/60

TOHOKU UNIVERSITY
KATAHIRA CAMPUS MAP

North Gate (KITA-MON)

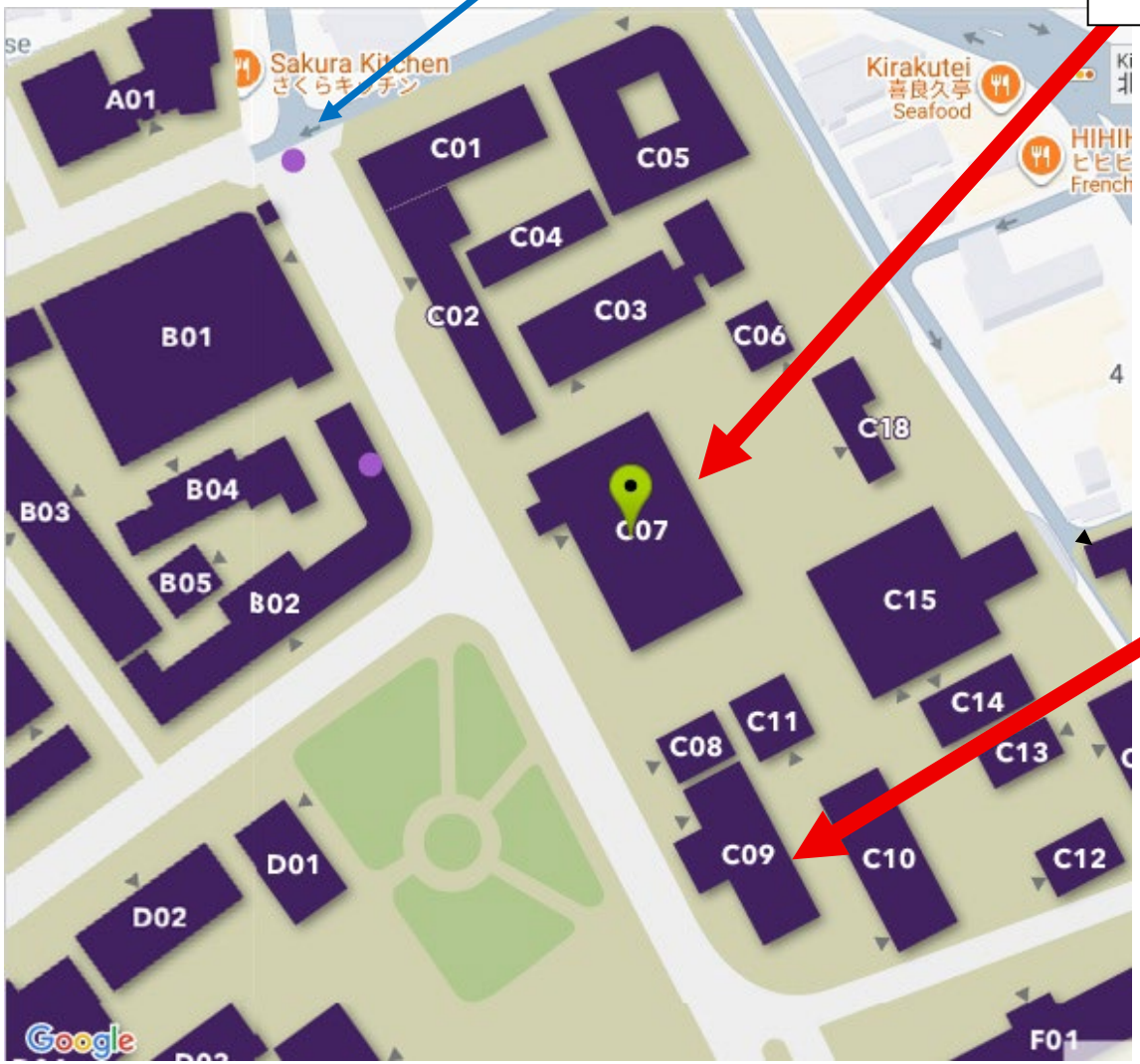

Extended Education & Research Building (C07)
6th floor Lecture Room A
- Registration & Workshop Venue -

IFS Building 1 (C09)
2nd floor Meeting Room
- Poser Session and Lunch Venue -

BBANQUET

18:30-20:00, Saturday, March 7

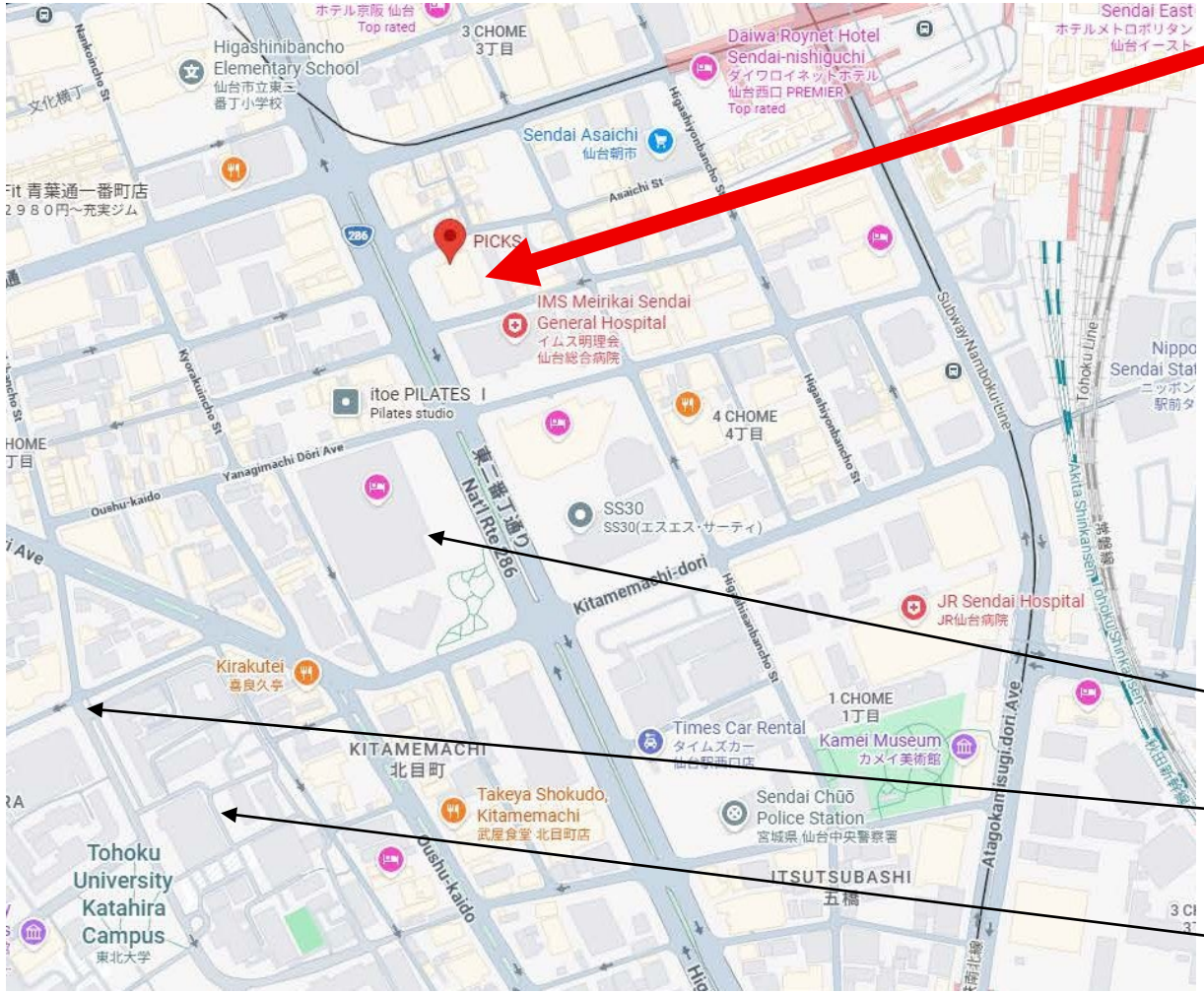

PICKS

1F, Urbannet Sendai-Chuo Building,
4 Chome-4-19 Central, Aoba Ward,
Sendai, Miyagi 980-0021

Westin Hotel

North Gate (KITA-MON) of Katahira Campus

Workshop Venue

Saturday, March 7th

		9:00	9:10	Opening
Advanced Materials & Structural Integrity	Chairpersons: Prof. Y. Sato and Prof. S. Dancette	9:10	9:25	Role of ions in time evolution of bending of electro-responsive polymers (TEmPuRA) **Manuel Rivera** (INSA Lyon), **Hidemasa Takana** (TU) et al.
		9:25	9:40	Stress assessment from alternative incremental permeability method **Eric Wasniewsk**i (CETIM) et al.
		9:40	9:55	Atomic strain field in high entropy alloys. TEM observations and numerical results **Pierre-Antoine Geslin** (ELyTMaX) et al.
		9:55	10:10	NDT based on the magnetization mechanisms: last progress in the framework of BENTO. **Benjamin Ducharne** (INSA Lyon), **Tetsuya Uchimoto** (TU) et al.
		10:10	10:25	Carbon Fiber Reinforced Polycarbonate Strengthened by HLEBI. **Yoshitake Nishi** (Tokai University) et al.
		10:25	10:45	Coffee break
		10:45	11:00	Self-Sensing and Self-Powered Piezoelectric Structural Identification for Health Monitoring **Yushin Hara** (TU) et al.
Manufacturing Processes & Material Synthesis	Chairpersons: Prof. S. Besset and Prof. T. Uchimoto	11:00	11:15	Al-Fe arc welding: experiment and simulation (MIMECHAS) **Benjamin Leflon**, **Kiyoaki T. Suzuki** (TU) et al.
		11:15	11:30	Elaboration and mechanical behavior of porous NiTi alloys fabricated by liquid metal dealloying **Mikihisa Fukuda** (TU) et al.
		11:30	11:45	Surface engineering of ZnO nanorods **Alexandra Apostoluk** (INSA Lyon) et al.
		11:45	12:00	MOREOVER project: Design of an EIS-based sensor for non-invasive in-field corrosion monitoring **Benoit Ter-Ovanessian** (INSA Lyon), **Zhixin Dong**, **Hiroshi Abe** (TU) et al.
		12:00	14:30	Poster Session with Lunch @ Meeting Room on the 2nd Floor of IFS Building 1

Manufacturing Processes & Material Synthesis	Chairpersons: Prof. S. Besset and Prof. T. Uchimoto	14:30	14:45	Advanced High temperature Processing Platform For The Development Of Novel Materials @ MATEIS Laboratory **Florian Mercier** (INSA Lyon)
		14:45	15:00	Synchronising Microstructure Control and Machinability in L-PBF Titanium Alloys **Chi-Ho Ng** (TU) et al.
		15:00	15:15	Copper Metallization on Oxide Ceramics by Low-Pressure Cold Spray and Its Deposition Mechanism **Kazuhiro Ogawa** (TU) et al.
Computational Mechanics & Data-Driven Modeling	Chairpersons: Prof. E. Gaudry and Prof. T. Tokumasu	15:15	15:30	Robust Multi Objective optimization design approaches Acronym of the ELyT project MuORode **Thanasak Wanglomklang**, **Sébastien Besset** (Centrale Lyon) et al.
		15:30	15:45	Dynamic Monte Carlo Simulations of Turing Pattern **Hiroshi Koibuchi** (Ibaraki KOSEN) et al.
		15:45	16:00	Effect of non-equilibrium state on the C drift velocity in iron with electric field (CarboEDiffSim) **Takashi Tokumasu** (TU) et al.
		16:00	16:20	Coffee break
		16:20	16:35	Exploring Complex Intermetallics and Quasicrystal Approximants as Catalysts **Emilie Gaudry** (Univ. Lorraine) et al.
Fluid Dynamics, Thermal Science & Energy	Chairpersons: Prof. T. Adach and Prof. M. Lallart	16:35	16:50	Heat to power energy conversion using natural rubber (REFRESH) **Gael Sebald** (INSA Lyon), **Atsuki Komiya** (TU) et al.
		16:50	17:05	Thermal aggression of a metallic wall by a reacting flow: near-wall gas-phase temperature measurements with laser diagnostics **Pradip Xavier** (INSA Rouen Normandie) et al.
		17:05	17:20	Contact Electrification of High-speed Nanodroplets Impinging on Various Metal Plates under Different Generation Conditions **Jiun-Shian Lee** (TU) et al.
		17:20	17:35	Presentation of ENSAM research activities **Ivan Iordanoff** (VP for research and innovation at ENSAM) et al.
		18:30	20:00	Banquet @ PICKS

Sunday, March 8th

Fluid Dynamics, Thermal Science & Energy	Chairpersons: Prof. G. Sebald and Prof. A. Komiya	9:00	9:15	Self-powered beacon using optimized magnetic energy harvester and ultralow power design **Hanae Aoki** (TU), **Mickaël Lallart** (INSA Lyon) et al.
		9:15	9:30	DMD analysis of the length-to-diameter ratios for flow passing through a cylinder with its axis parallel to the flow direction **Hiraku Yata** and **Takahiro Adachi** (Akita University) et al.
		9:30	9:45	Towards greener Vacuum Insulation Panel, X-ray tomography measurements to understand fiber network as pressure decrease. (TP-VIP) **Genevieve Foray** (INSA Lyon) et al.
		9:45	10:00	Advanced Computational Study of Liquid Ammonia Atomization and Spray Combustion Characteristics with Phase Change **Jun Ishimoto** (TU)
Bio-Engineering & Medical Hemodynamics	Chairpersons: Prof. C. Pailler-Mattei and Prof. M. Ohta	10:00	10:15	Towards in vivo mechanical characterisation of intracranial aneurysms: a Coherent Point Drift-based approach **Lise Fontalirant** (Centrale Lyon) et al.
		10:15	10:30	Towards Real-Time Whole-Brain Arterial 3D Hemodynamic Prediction — A Physics-Constrained Deep Learning Framework for the Internal Carotid Artery **Jing Liao** (TU) et al.
		10:30	10:45	Cellulose Nanofiber-Reinforced Silk Fabrics via Silkworm Feeding: Tensile Properties and Dimensional Stability **Hiroki Kurita** (TU) et al.
		10:45	11:05	Coffee break
Tribology & Surface Engineering	Chairpersons: Prof. K. Adachi and Prof. V. Fridrici	11:05	11:20	Mechano-Chemically-activated Tribofilm Growth at Nanoscale on DLC materials (MeCaT-DLC) **Jean Michel Martin** (Centrale Lyon), **Shaoli Jiang** (TU) et al.
		11:20	11:35	Achieving 30-fold friction anisotropy in liquids using rubber with inclined-groove texture **Arata Ishizako** (TU) et al.
		11:35	11:50	Anodization of aluminum for self-formation of low friction interfaces under severe tribological conditions: AnodiTribo project **Theo Yamana** (TU, Centrale Lyon) et al.

Tribology & Surface Engineering	Chairpersons: Prof. K. Adachi and Prof. V. Fridrici	11:50	12:05	In-situ Synchrotron Quantification of Internal Strain Distribution in Rubber During Dry Sliding Against a Resin Sphere **Toshiaki Nishi** (TU)
		12:05	12:20	Visco-elastic contact : rolling versus sliding, and the effect of multi-layered material and roughness on the apparent friction coefficient **Daniel Nelias** (INSA Lyon)
		12:20	12:35	Investigation of bulk and interface mechanical properties; correlations for hard on soft contacts **Antoine Normant** (TU), Sylvain Dancette (INSA Lyon) et al.
		12:35	12:50	Closing
		12:50	14:00	Lunch
		14:00		Optional: Excursion

Poster Session: Saturday, March 7, 12:00-14:30

Please create your poster in A0 size. It will also be displayed at the anniversary ceremony on Monday, March 9.

1	SOLYDIC project: Effect of hydrogen pre-charging on the tribological behavior of lubricated 100Cr6/100Cr6 contacts **Nicolas Mary** (INSA Lyon) et al.
2	HLEBI Induced Fracture Toughness of 3D-Printed Short CFR-PLA **Hirotaka Irie** (Tokai University) et al.
3	Probabilistic Evaluation Method for Cracks on Divertor Armors in Fusion Reactors Using Direct Current Potential Drop Technique **Kazushi Honjo** (TU) et al.
4	Evaluation of Natural Rubber Crystallization Effect on Variation in Elastocaloric Coefficient **Takuma Oiri** (TU) et al.
5	Annealing the Adhesive Film Increases the Local Shear Stiffness of the Formula SAE Carbon Monocoque Without Increasing Weight. **Tsubasa Nakayasu** (Tokai University) et al.
6	A Molecular Dynamics Approach to Computing the Work of Adhesion at Various Surfaces **Takumi Tanaka** (TU) et al.
7	Transition of Momentum Transport Pathways under Shear: A Molecular Dynamics Insights **Masaharu Yoshida** (TU) et al.

8	AI-assisted symmetry-informed topology optimization of woven materials for broadband sound absorption (MuORode) **Thanasak Wanglomklang** (INSA Lyon) et al.
9	Metamodel-based Robust Shape Optimization for Aircraft Cabin Noise Reduction (MuORode) **Thanasak Wanglomklang** (INSA Lyon) et al.
10	Towards Large-Scale Realistic Cerebral Artery Generation (Engineering for Health Simulation & Modeling) **Vedhino Bima Aryaputra Ahnaf** (TU) et al.
11	An Advanced Non-Invasive EIS Method for Corrosion Layer Characterization: From Model Materials to Archaeological Artifacts (MOREOVER) **Benoît Ter-Ovanessian** (INSA Lyon) et al.
12	Strengthening and deformation mechanisms of high strength biodegradable Fe–10Mn alloy **Hiroya Ishii** (TU) et al.

Saturday, March 7th

Morning

Role of ions in time evolution of bending of electro-responsive polymers

TEmPuRA

ELyT Global

Theme (Energy)

Scientific topic (Simulation & Modeling)

					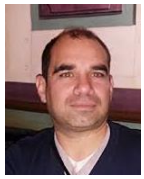
M. RIVERA [a,b,c,d]	G. COATIVY[a]	V. PERRIN[a]	L. SEVEYRAT [a]	Y.GUO[e]	D. ALBERTINI [f]

				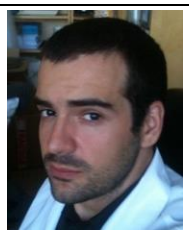		
J. COURBON[g]	G. SEBALD[d]	Y. Kaneko[b]	F. DALMAS[g]	S. LIVI[h]	J-Y. CAVAILLE [b,c,d]	H. TAKANA[b,c]

[a] *LGEF, EA 682,INSA Lyon, Univ. Lyon*	[e]*FRIS, Tohoku University, Aoba-ku, Sendai, 980-0845, Miyagi, Japan*
[b] *IFS, Tohoku University*	[f] *INL, UMR5270, VILLEURBANNE, 69622, France*
[c] *IFS Lyon Center, Tohoku Univ., INSA Lyon*	[g]*MATEIS, UMR 5510, CNRS INSA Lyon, Univ. Lyon*
[d] *ELyTMaX, IRL 3757, CNRS – INSA – ECLyon - UCBLyon - Tohoku Univ.*	[h]*IMP, UMR 5223, INSA Lyon, Univ. Lyon*

Abstract

When subjected to a constant electric field, thin elastomeric films coated with electrodes, such as polyurethane, bend progressively and non-monotonically [1,2]. This behavior is not expected in a pure dielectric elastomer, as it requires an asymmetric distribution of charge over time, which should not be observed in pure dielectric elastomers (a symmetric distribution and rapid response are expected). Our experimental and theoretical work suggests that the presence of a

small amount of ionic impurities could explain this phenomenon [2,3]. In addition, our ongoing modeling and simulation work has shown that in the case of monoatomic ions such as Na^+ and Cl^-, the slow redistribution of ions, when the electric field is deactivated, is responsible for a kind of memory effect (by applying the electric field again, bending continues from the point when the electric field is deactivated). Finally, in the case of elastomers doped with complex polyatomic ions such as ionic liquids, a remanent deformation has been observed experimentally after the electric field is turned off (see Figure) and has been attributed to the presence of a residual layer rich in anions [4], as evidenced by Energy-Dispersive X-ray (EDX). The role of cations (which were not detected by EDX due to a lack of chemical contrast with the matrix) and the mechanisms responsible for stabilizing the anionic layer are still under investigation. The presentation in this workshop aims to summarize these results on both aspects, experimental and modeling.

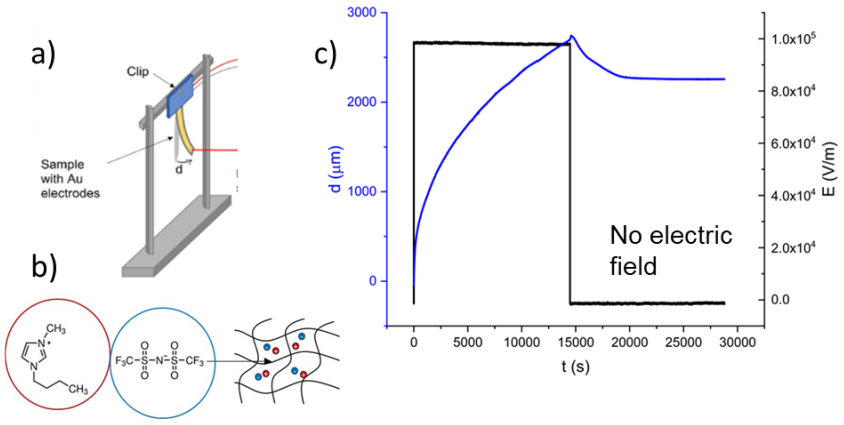

Figure. a) set-up used to study the bending under constant electric field b) schematic of ionic liquid doped elastomer c) bending obtained for epoxy-amine doped with BMIM-TFSI at a constant electric field of 0.1MV/m and after turning off the electric field.

References:

[1] M. Watanabe, T. Hirai, Bending-electrostrictive response of polyurethane films subjected to a reversed electric field, J. Appl. Polym. Sci. 92 (2004) 3644–3650. https://doi.org/10.1002/app.20300.

[2] G. Coativy, K. Yuse, G. Diguet, V. Perrin, L. Seveyrat, F. Dalmas, S. Livi, J. Courbon, H. Takana, J.Y. Cavaillé, Role of charge carriers in long-term kinetics of polyurethane electroactuation, Smart Mater. Struct. 31 (2022) 125019. https://doi.org/10.1088/1361-665X/aca12e.

[3] G. Diguet, J.-Y. Cavaillé, G. Coativy, J. Courbon, Electric space charge threshold observation in polyurethane under high electric fields, J. Appl. Phys. 135 (2024). https://doi.org/10.1063/5.0182679.

[4] G. Coativy, L. Seveyrat, V. Perrin, D. Djoumoi, D. Albertini, J. Courbon, H. Takana, J.-Y. Cavaillé, K. Ryskulova, S. Livi, F. Dalmas, Remanent deformation and local stiffening induced by electric field in low glass transition epoxy-amine polymer network doped with ionic liquid, Polymer (Guildf). 339 (2025) 129169. https://doi.org/10.1016/j.polymer.2025.129169.

stress assessment from alternative incremental permeability method

ELyT Global
Magnetic NDT for steel characterization

	**Dr. Eric WASNIEWSKI** **CETIM[1]**		Associate Pr. Benjamin DUCHARNE ELyTMaX[4,5]
	**Pr. Laurent DANIEL** **GeePs [2,3]**		**Dr. Fan ZHANG** **CETIM[1]**
	**Pr. Tetsuya UCHIMOTO** **IFS[6]**		

[1]Cetim, 52 avenue Félix Louat 60300 Senlis, France

[2]Université Paris-Saclay, CentraleSupélec, CNRS, Laboratoire de Génie Électrique et Électronique de Paris, 91192, Gif-sur-Yvette, France

[3]Sorbonne Université, CNRS, Laboratoire de Génie Électrique et Électronique de Paris, 75252, Paris, France

[4]Univ Lyon, INSA Lyon, LGEF EA682, 69621 Villeurbanne, France

[5]ELyTMaX IRL3757, Univ Lyon, INSA Lyon, Centrale Lyon, Université Claude Bernard Lyon 1, Tohoku University, Sendai 980-8577, Japan

[6]Institute of Fluid Science (IFS), Tohoku University, Sendai, Japan

Abstract

Residual stresses play a major role in determining the performance, integrity, and service life of structural steels. Residual stresses are usually analyzed by X-Ray diffraction. This technique may not be adapted for high-speed production, but the evaluation of internal stresses enables the anticipation of potential breakdown and degradation. Magnetic measurements are an alternative non-destructive technique, employed to characterize industrial components. The exploration of its ability to evaluate residual stress is a promising line of research.

1 Incremental permeability measurements

1.1 Incremental permeability

The Magnetic Incremental Permeability (MIP) corresponds to the slope of the inner asymmetric hysteresis loops (Figure 1). These loops, also called minor cycles, are obtained when the tested material is exposed to the superimposition of two magnetic contributions:

1. A low frequency (quasi-static), high amplitude magnetic excitation that provides a bias magnetization.

2. A high frequency, low amplitude magnetic excitation, allowing the measurement of the relative magnetic incremental permeability μ_{MIPr}.

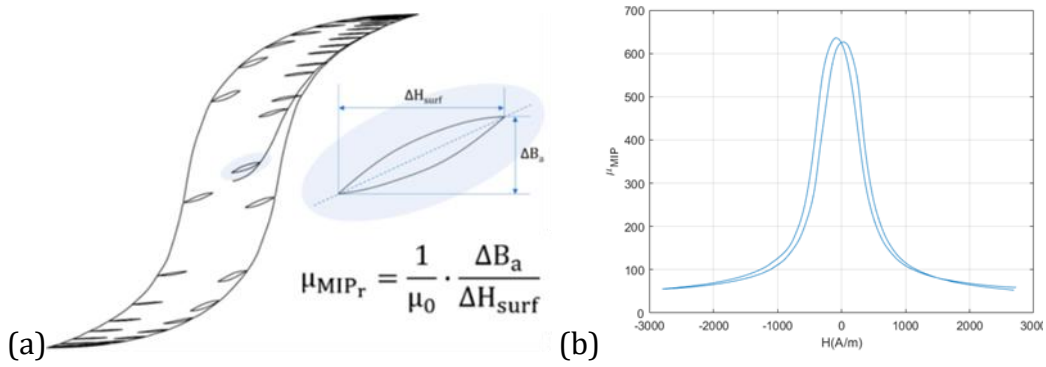

Figure 1: a) MIP illustration and definition and b) example of incremental permeability measurement.

1.2 Samples

Single crystal of Iron-Silicon Grain Oriented sheets (FeSi GO) and low carbon steel (DC04) were tested in this study. All specimens were extracted from the same batch and cut by electrical discharge machining (EDM) at different orientations from the rolling direction (0°, 30°, 45°, 54.7°, 60°, and 90° for FeSi and 0°, 45° and 90° for DC04). For each orientation, MIP measurements have been performed at various levels of applied tension stress. MIP was measured along the specimen in the direction of stress application.

2 Alternative Setup

The conventional setup for MIP measurements employs a single pancake coil positioned on the sample surface and connected to an Impedancemeter. In the proposed alternative configuration, two coils are utilized: one to introduce the high-frequency component and the other to capture the resulting signal. Moreover, adjusting the angle between the sensor and the sample orientation provides an additional degree of freedom, thereby enhancing the analytical capabilities of the measurement.

Conclusion

Measurements performed with the alternative setup demonstrate better sensitivity to stress as a function of the angle relative to the sample's length, compared to the standard configuration.

Atomic strain field in high entropy alloys. TEM observations and numerical results

ELyT Global

Materials science Metallurgy

Dr. Pierre-Antoine GESLIN

ElyTMaX, CNRS / Tohoku University Sendai, Japan,

Dr. Louis LESAGE

(i) ElyTMaX, CNRS / Tohoku University Sendai, Japan,
(ii) ESRF, Grenoble, France

Dr. Matthieu BUGNET

(i) Mateis, INSA-Lyon, Lyon, France
(ii) SuperSTEM Lab, Daresbury United Kingdom

Prof. Hidemi KATO

IMR, Tohoku University, Sendai, Japan

Abstract

High entropy alloys contain multiple components in comparable quantities forming a solid solution phase. They have attracted increasing attention in the past decades due to their exceptional mechanical properties [1,2]. In the solid solution phase, the random arrangement of atoms of different sizes leads to lattice distortions as atoms are slightly displaced away from their lattice site (see Fig. 1.a). These lattice distortions are the focus of intense research because their amplitude have been shown to correlate with mechanical, thermodynamical, electrical, and magnetic properties of the alloys.

High resolution scanning transmission electron microscopy (HRSTEM) has emerged recently as an interesting tool to measure lattice distortions at the nanometer scale in concentrated alloys [3]. Fig. 1.b shows typical strain maps obtained with this technique. The random fluctuations of strains at the nanoscale emerge from the random arrangement of solute

atoms in the crystalline lattice; yet, strain maps appear to display specific patterns: the strains components ε_{xx} and ε_{yy} show elongated stripes in the x and y directions respectively while ε_{xy} appear to be more isotropic.

To rationalize these observations, we developed an elastic model of random alloys where atoms of different species are modeled as misfitting inclusions in an homogeneous isotropic medium [4]. Despite its simplicity, this model reproduce the key features of the experimental strain maps (see Fig. 1(b)). In addition, atomistic calculations have also been used to investigate the influence of the thin foil surfaces on the results.

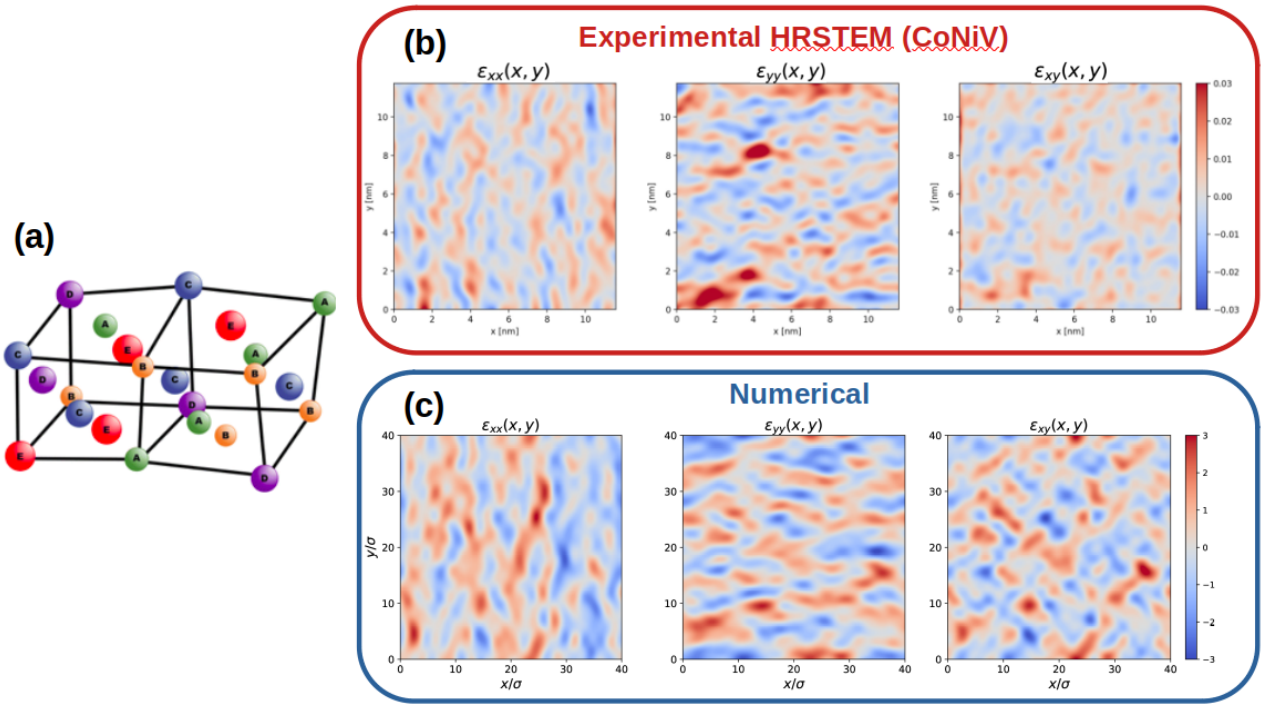

Figure 1: (a) Schematic representation of lattice distortions in high entropy alloys. (b) Strain maps measured experimentally with HRSTEM on a CoNiV thin foil . (b) Strain maps obtained numerically from the elastic model

Reference :

[1] E. P. George, D. Raabe, R. O. Ritchie, High-entropy alloys, Nature reviews materials 4 (2019) 515–534.

[2] D. B. Miracle, O. N. Senkov, A critical review of high entropy alloys and related concepts, Acta materialia 122 (2017) 448–511.

[3] Q. Ding, Y. Zhang, X. Chen, X. Fu, D. Chen, S. Chen, L. Gu, F. Wei, H. Bei, Y. Gao, et al., Tuning element distribution, structure and properties by composition in high-entropy alloys, Nature 574 (2019) 223–227.

[4] P.-A. Geslin, D. Rodney, Microelasticity model of random alloys. Part I: mean square displacements and stresses, Journal of the Mechanics and Physics of Solids 153 (2021) 104479.

NDT based on the magnetization mechanisms:

last progress in the framework of BENTO.

ELyT Global
Magnetic Rotational Permeability (MRP)

			
Tetsuya UCHIMOTO	**Benjamin DUCHARNE**	**Gael SEBALD**	**Yves Armand TENE DEFFO**

Abstract

Mechanical stresses strongly influence the magnetic behavior of non-oriented electrical steels (NOES), with direct consequences for the performance and reliability of electrical machines. Conventional magnetic nondestructive testing (NDT) techniques predominantly rely on unidirectional magnetization, which limits access to magnetization mechanisms that are particularly sensitive to stress. In contrast, rotational magnetization selectively activates additional mechanisms, such as reversible 90° domain wall motion and coherent domain rotation, whose contributions remain insufficiently exploited for stress evaluation.

In this work, a novel magneto-mechanical characterization approach, termed Magnetic Rotational Permeability (MRP), is proposed for the indirect assessment of uniaxial tensile stress in NOES sheets. The method combines a low-speed quasi-static rotational magnetic field, generated by two orthogonally arranged electromagnets, with a transmission - reception eddy current transducer (ECT) operating under locally homogeneous magnetic conditions. The rotational magnetization enables the investigation of stress-sensitive mechanisms over a wide excitation range, from low-field reversible domain wall bulging to high-field regimes governed by magneto- crystalline anisotropy and magnetoelastic energy.

Experimental investigations were conducted on NOES specimens subjected to controlled uniaxial tensile stress up to 200 MPa. The real and imaginary components of the ECT receiver voltage were analyzed as functions of the rotational field amplitude, excitation frequency, and applied stress. MRP butterfly curves and polar representations revealed strong stress sensitivity, particularly in the imaginary component of the ECT signal. Several magnetic indicators derived

from the MRP response exhibited high linear correlation with tensile stress, with Pearson coefficients exceeding 0.95 under optimized excitation conditions.

The results demonstrate that MRP provides reliable and physically interpretable magnetic indicators for stress evaluation, while remaining compatible with NDT constraints. By leveraging rotational magnetization mechanisms, this approach opens new perspectives for multidimensional magnetic characterization and advanced stress monitoring in electrical steels.

Carbon Fiber Reinforced Polycarbonate Strengthened by HLEBI.

ELyT Global

*Effects of HLEBI to Polymers & its Composites
**HLEBI Induced Adhesive force of CF/Polymers

Yoshitake Nishi[1,2,3,4+], Helmut Takahiro Uchida[1], Kousuke Sagawa[1], Masae Kanda[1*], Eiichi Miura[1+], Michael C. Faudree[1#], Hideki Kimura[1],

1Tokai Univ., 〒259-1292, 4-1-1, Kitakaname, Hiratsuka, +KISTEC, *Chubu Univ., #Tokyo City Univ. **Japan**.

Michelle Salvia[2], Kaori Yuse[3], Jean-Yves Cavaille[3], Alain Vautron[4], Daniel Gyomar[3], Pierre-Francois Gobin[3],

2EC-Lyon,Ecully Cedex 69134, **France**.

3INSA Lyon, *Bât. B. Pascal, 5° étage, 7, Avenue Jean Capelle, 69621 Villeurbanne cedex,* **France.**

4ENSM.St. Saint-E´tienne Cedex 2 42023, **France**

Abstract:

Since **1998,** our target of the projects, started by **Gobin (INSA Lyon) & Tani (Tohoku University)** late Profs. Emeritus, have been the rising the **international research collabirations for constructed and smart materials.** Excellent results were getting **PhD (INSA Lyon) of M. Kanda, Master of Engineering** (**Tokai** University), as well as following **papers** collaborated with **three Research Alliances. Our Future contribution to J-F Collaboration (A,B & C)** will be progressed in the following three fields. By the way, recent topics related to strengthening methods of carbon fiber reinforced polycarbonate (Ref. A-①,②,④&⑪) will be mainly introduced. One of the paramount tasks for achieving a sustainable environment is elimination of non-recyclable plastics. Although thermoplastics are recyclable, they are weaker than thermoset epoxy polymer. Thus, applying homogeneous low voltage electron beam irradiation (HLEBI) to carbon fiber reinforced polycarbonate (CFRPC) have been proposed to increase strength. Experimental results showed an *intermediate* process of applying 129 kGy dose of 170 kV-HLEBI directly to each CF ply before hot press improved median impact value ~19% over those of untreated. Likewise, improvement of median 3-point bending strength by *intermediate* process of 215 kGy was ~18%. On the other hand, a *finishing process* of applying 258 kGy HLEBI dose at 170 kV cathode potential (V_c) to CFRPC sample surfaces just after hot-press, that can potentially be done before shipping, strengthens median impact value significantly, about 22% larger than that of untreated. Furthermore, an 86 to 172 kGy dose range at 250 kV apparently improved mean impact value, which was 25-30% higher than CFRPC specimens untreated. Although the improvement in impact value from the *finishing process* was slightly higher than that from the *intermediate* process, the *intermediate* process can be tailored for samples of any thickness. To explain the strengthening of the CFRPC by optimal dose of HLEBI, many factors need to be considered of not only fractography discussion of fracture mechanism transition from cracks propagating, but also nanoscale discussion with X-Ray photoelectron spectroscopy (XPS) analysis of the CF/PC interface.

Research Activities of three J/F-Research Alliances for a Last Quarter Century

Based on the collaboration-A with **ECL (M. Salvia), 16** papers of the **CFRPs** (fiber reinforced polymer) have been **firstly** investigated. They are A-①: **Additional Strength of CFRPC Induced by HLEBI**, K.Sagawa, H. Kimura, H.T.Uchida,F.S.,N.T.,S.Kaneko,M.Salvia,M.C.Faudree,Y.Nishi, (Chap. Springer Book "Recent Developments in Advanced Bio- and Nano-Materials" ed. by P.M.,C.G.,P.B.,A.K.,S. Kaneko) in press. **A-② : Increasing Cathode Potential of HLEBI to Increase Impact Strength of CFRPC & Characterization by XPS C_{1s} and O_{1s} Peaks,** F.Sato, K. Sagawa, H.-T. Uchida, H. Irie, M.C.Faudree, M. Salvia, A.Tonegawa, S.Kaneko, H.Kimura, Y.Nishi, Materials, in press. A-③ : **Impact Value Improvement of PC by Addition of Layered CF Reinforcement and Effect of EB Treatment,** Y. Nishi, N. Tsuyuki, M. C.

Faudree, H. T. Uchida, K. Sagawa, Y. Matsumura, M. Salvia, H. Kimura, Polymers, 17(8) 1034 (2025), A-④:Novel Treatment for 3D-SCFRPA66 of HLEBI on Tensile Properties, E Miura, H-T. Uchida, T. Okazaki, K. Sagawa, M. C. Faudree, M. Salvia, H. Kimura, Y. Nishi, Polymers, 16(23) 3408 (2024), A-⑤: **Increasing Bending Strength of PC Reinforced by CF Irradiated by EB** :Y. Nishi, N. Tsuyuki, H. T. Uchida, M. C. Faudree, K. Sagawa, M. Kanda, Y. Matsumura, M. Salvia, H. Kimura, Polymers, 15(22) 4350 (2023), A-⑥: A Novel Nickel-Plated CF Insert in Al Joints with Thermoplastic ABS Polymer or Stainless Steel, Y. Nishi, K. Sagawa, M. C. Faudree, H. T. Uchida, M. Kanda, S. Kaneko, M. Salvia, Y. Matsumura, H. Kimura, Materials 16(17)5777 (2023), A-⑦: Improvements of Strength of Layered PP Reinforced by CF by its Sizing Film and EB under Protective N_2 Gas Atmosphere: Y. Nishi, S. Kitagawa, M. C. Faudree, H. T. Uchida, M. Kanda, S. Takase, S. Kaneko, T. Endo, A. Tonegawa, M. Salvia & H. Kimura: Suzuki Carbon Book (Springer Nature Singapore Pte Ltd.2021, ISBN978-981-15-7609-6 & -7610-2 (eBook) https://doi.org/10.1007_978-981-15-7610-2, Chapter 12, pp.279-302, A-⑧: Advances in Ti-Polymer Hybrid Joint by CF-Plug Insert: Current Status and Review, M. C. Faudree, H. T. Uchida, H. Kimura, S. Kaneko, M. Salvia, Y. Nishi, Materials <Special Issue Organic Matrix Composites and Multifunctional Materials.15-3220-PP1-19.> 15 (9) 3220 (2022), A-⑨: A Novel Joint of 18-8 Stainless Steel and Al by Partial Welding Process to Ni-Plated CF Junction: M. Tomozawa, M. C. Faudree, D. Kitahara, S. Takase, Y. Matsumura, I. Jimbo, M. Salvia & Y. Nishi, Maters. Trans. 61 (12) 2292 (2020), A-⑩: A New Process of Thermoplastic PP Reinforced by Interlayered Activated CF treated by EBI under N_2 gas atmosphere with O_2 prior to Assembly and Hot-press, S. Kitagawa, H. Kimura, H. T. Uchida, M. C. Faudree, A. Tonegawa, S. Kaneko, M. Salvia, Y. Nishi; Meters.Trans. 60(4) 587(2019), A-⑪: Tensile strength of PP reinforced by CF covered with and without sizing epoxy film, S. Kitagawa, H. Kimura, S. T., N. T., D. K., A. T., M. C. Faudree, H. T. Uchida, A. Tonegawa, M. Kanda, N. Inoue, S. Kaneko, T. Endo, M. Salvia, Y. Nishi; Trans. Materials Research Society of Japan, Jun 125 (2018), A-⑫**: Enhanced tensile strength of Ti/PC joint connected by EB activated cross-weave CF cloth insert,** H.H., M.C.Faudree, Y.E., S.T., H.Kimura, A.Tonegawa, Y.Matsumura, I.Jimbo, M.Salvia, Y.Nishi, Maters. Trans. 58(11) 1606 (2017), A-⑬: Improvement of bending modulus and impact value of injection-molded short CF reinforced PEEK with HLEBI, Y. Nishi, R. Ourahmoune, M. Kanda, J.H. Quan, M.C. Faudree and M. Salvia; *Mater. Trans.*, **55** (8) 1304 (2014), A-⑭:Effects of EBI on elasticity of CFRTP (CF/PEEK), H. TAKEI, M. Salvia, A. Vautrin, A.Tonegawa, Y.Nishi; Mater. Trans. **52** (4) 734 (2011), A-⑮ : Effects of EBI on impact value of Novolak-type phenol CFRTP, Y. Nishi, H. Takei, K. Iwata, M. Savia, A. Vautrin, Mater.Trans.51(12) 2259 (2010), and A-⑯**:** Effects of EBI on impact value of CFRTPEEK, Y. Nishi, H. Takei, K. Iwata, M.Salvia, A. Vautrin; Mater.Trans. **50** (12) 2826 (2009).

Based on the collaboration-B with **LGEF, INSA de Lyon (D. Guyomar & K. Yuse), 12** papers of the **Sensor and Actuators** have been **secondary** investigated and constructed with B-①Effect of 100 keV Class EBI on Impact Fatigue Behavior of PZT ceramics : N.T.**,** A.T.**,** S.T.**,** D.K.**,** M. Kanda**,** N. Inoue**,** K.Yuse, D.Guyomar, A.T., Y.M. & Y.Nishi; Maters. Trans.; 59(3)450(2018), B-②An Improved H_2-gas pressure operated $LaNi_5$ powder-dispersed PU/Ti 2-layer actuator with reversible giant and rapid expansion by hydrogenation : Y.Nishi, J.O., M.C.Faudree, M.Kanda, K.Yuse, D.Guyomar, H-H.Uchida; Maters. Trans., 59(1)129 (2018), B-③Improvement of Electric Field Induced Compressive Electrostriction of PU Composites Film Homogeneously Dispersed with Carbon Nanoparticles, M. Kanda, K. Yuse, B. Guiffard, L. Lebrun, Y. Nishi, D. Guyomar: Maters. Trans., 56(12) 2029 (2015), B-④Actuation abilities of multiphasic electroactive polymeric systems, M.Lallart, J.-F.Capsal, A.K. Mossi Idrissa, J.Galineau, M.Kanda, D.Guyomar; J. Applied Physics,112 (2012) 094108), B-⑤ Solidification Thickness Dependent Electrostriction of PU Films (M.Kanda, K.Yuse, B.Guiffard, L.Lebrun, Y.Nishi, D.Guyomar: Maters. Trans.,53, 1806 (2012), B-⑥ Modeling of thickness effect and polarization saturation in electrostrictive polymers, M.Lallart, J.-F.Capsal, M.Kanda, J.Galineau, D.Guyomar, K.Yuse, B.Guiffard: Sensors and Actuators B: Chemical, 171-172, 739 (2012), B-⑦The compressive electrical field electrostrictive coefficient M_{33} of electroactive polymer composites and its saturation versus electrical field, polymer thickness, frequency and fillers, D.Guyomar, P.-J.Cottinet, L.Lebrun, C.Putson, K.Yuse, M.Kanda, Y.Nishi: Polym. Adv. Technol, (2011) DOI 10.1002/pat.1993), B-⑧Thickness effect on electrostrictive PU strain performances: A three-layer model, D.Guyomar, K.Yuse, M.Kanda , Sensors and Actuators A,168, 307 (2011), B-⑨ Development of large-strain and low-powered electro-active polymers (EAPs) using conductive fillers, K.Yuse, D.Guyomar, M. Kanda, L.Seveyrat, B.Guiffard: Sensors and Actuators A,165,147 (2011), B-⑩ Focus on the electrical field-induced strain of electroactive polymers and the observed saturation, D.Guyomar, K.Yuse, P.-J. Cottinet, M.Kanda, L.Lebrun, J. Applied Physics,108, 114910 (2010), B-⑪ Reversible Bending Motion of Unimorph Composites Driven by Combining $LaNi_5$ Alloy Powders Dispersed PU and Thin Supporting Cu Sheet under Partial Hydrogen Gas Pressure, J.O.,M.Kanda,K.Yuse,H-H.Uchida, D.Guyomar, Y.Nishi, Maters. Trans.,51, 994 (2010), and B-⑫ Giant Bending Strain of Reversible Motion of Uni-Morph Soft Mover Composites Driven by Hydrogen Storage Alloy Powders Dispersed in PU Sheet, Y.Nishi, S.O., M.Kanda, A.S.,R.S.,Y.E.,D.K., H.H.Uchida., K.Yuse, D.Guyomar: Maters. Trans.,50, 2460 (2009).

Based on the collaboration-C with **MATEIS, INSA de Lyon (J-Y Cavaille), 6** papers of the **adhesion and strengthening of polymers induced by EBI** process have been **thirdly** investigated and constructed with C-①Adhesion of PE/PET laminated sheets by HLEBI prior to assembly and hot-press above melting point, S.T., H. T.Uchida,A.Y.,M.Kanda,O.Lame, J.-Y.Cavaille,Y.M.,Y.Nishi: Maters. Trans., 58(7)1055 (2017), C-② Effects of HLEBI on adhesive force of peeling resistance of laminated sheet with PE and austenitic 18-8 stainless steels, C.K., M.Kanda, O.Lame, J-Y.Cavaille, Y.Nishi: *Maters. Trans.*, 57(3) 373 (2016), C-③ Effects of HLEBI on brazilian bending strength of liquid quenched ten mega molecular weight-polyethylene (TMMW-PE), Y.Nishi, M.Kanda, K.S., S.I., M.U., S.I., M.C.Faudree, O.Lame, J-Y.Cavaille, 2016,Sept.26th-Zaoh-ELyT WS abstract. C-④Evaluation of the tensile strength of EB irradiated powdered ultra high molecular weight-polyethylene (UHMWPE) prior to sintering, M.Kanda, T.Deplancke, O.Lame, Y.Nishi and J-Y.Cavaille, *Maters Trans.*, 56 (9) 1505 (2015), C-⑤High electric conductive PMMA composites without impact value decay by dispersion of Cu powder, Y.Nishi, Y.E., N.K., M.Kanda, K.Iwata, K.Yuse, B.Guiffard, L.Lebrun, D.Guyomar, Maters. Trans., 51, 1437 (2010), C-⑥: Impact value of high electric conductive ABS composites with Cu powder dispersion prepared by solution-cast method, Y.Nishi, N.K., M.Kanda, L.Lebrun, D.Guyomar: Maters.Trans.,51,165(2010).

Self-Sensing and Self-Powered Piezoelectric Structural Identification for Health Monitoring

ELyT Global
Theme (Energy)
Scientific topic (Materials & Structure design)

	**Dr. Yushin HARA**		**Prof. Kanjuro MAKIHARA**

Abstract

Data-driven structural health monitoring enables the early detection of structural damage and facilitates detailed maintenance inspections and repairs. The method of extracting modal frequencies and modal shapes of target structures from data is termed operational modal analysis. Changes in mode information can detect whether structural alterations have occurred. Implementation of structural health monitoring needs input and output of the structure, which are excitation force and structural vibration. Three devices, an exciter, a vibration sensor, and an energy source to driven devices, are required. Preparing these devices individually and installing them on target structures leads to technical costs, creating barriers to the societal implementation of structural health monitoring. Consequently, the development of alternatives to these devices, or lower-cost devices, is desirable. Smart materials, particularly piezoelectric elements, possess the capability to convert electrical and mechanical energy into one another and have been utilized as actuators, vibration sensors, and vibration energy harvesters. Furthermore, research is underway into their operation as multifunctional smart materials, where a single piezoelectric transducer performs multiple functions.

The authors note that the three devices required for structural health monitoring can be replaced by piezoelectric elements. By assigning three functions to a single piezoelectric transducer, we propose a method to achieve structural health monitoring with the minimum number of devices. The voltage generated by the piezoelectric transducer, which performs three functions, exhibits a complex voltage waveform influenced by these three functions. Consequently, a challenge arose where the input and output data required for structural health monitoring could not be acquired from voltage information. Therefore, this research proposes a novel signal processing method to appropriately acquire the input and output data. Using input data obtained through signal processing, structural health monitoring was performed on a 60 kg structure, confirming that abnormalities were detected appropriately.

Al-Fe arc welding: experiment and simulation

ELyT Global
Theme: Transportation
Scientific topic: Materials & Structure design

	**Benjamin Leflon**		**Kiyoaki T. Suzuki**
	**Sylvain Dancette**		**Yutaka S. Sato**

Abstract

To reduce vehicle weight and CO_2 emissions, multi-material automotive structures which combine aluminum alloys with steel are in high demand. However, Al-Fe welding remains challenging because a brittle intermetallic compound (IMC) forms at the weld interface and degrades weld strength. The IMC at Al/Fe interfaces typically consists of a thick Fe_2Al_5 and a thin Fe_4Al_{13} layers. The dominant Fe_2Al_5 often serves as a preferential crack path under loading due to its low fracture toughness.

We have studied the effects of alloying elements on IMC microstructure and weld strength. In the first part of this presentation, we report the effect of Ni addition, which doubled the weld strength by changing the IMC morphology.

Alloying elements set aside, understanding the reaction kinetics of pure solid Fe and pure liquid Al is key to reliably predict IMC formation during Al-Fe welding. Although it has been studied a lot, uncertain areas remain regarding the actual phase formation sequence, the role of dissolution, and the correctness of the usually assumed volume diffusion regime. To clarify these points, we observed the Al-Fe reaction in situ by means of X-ray diffraction and tomography powered by synchrotron radiation. Tomography observations of pure aluminum powders melted on a pure Fe rod enabled to follow the formation of the typical tongue like

IMC and to quantify its thickness and interface positions over time. The sample annealed at 700 °C followed the expected volume diffusion regime perfectly, while deviations from it occured at 770 °C and 830 °C after a few minutes. In particular, thickness even ended up decreasing for the latter, showing the competing effect of IMC dissolution by the liquid Al bath at higher temperatures. Observing interface position revealed a counterintuitive net movement of the IMC towards liquid Al, while it is expected to grow towards solid Fe, which was explained from the difference in molar volumes between Fe and the IMC. Finally, X-ray diffraction on various types of samples, including powder mixtures, suggest that the main IMC phase Fe_2Al_5 and the minor one Fe_4Al_{13} always appear simultaneously right after Al melting, whereas FeAl, then $FeAl_2$, may only appear in later stages. Overall, this study supports that when it comes to modeling IMC growth for a quick transient process such as Fe-Al arc welding, only Fe_2Al_5 needs to be taken into account, and dissolution may be neglected.

Elaboration and mechanical behavior of porous NiTi alloys fabricated by liquid metal dealloying

ELyT Global

Materials science

Liquid metal dealloying, NiTi shape memory alloy

	**Mikihisa FUKUDA** **Graduate school of Engineering, Tohoku University,** **Sendai, Japan**		**Dr. Sylvain DANCETTE** **Mateis, INSA-Lyon / CNRS,** **Lyon, France**
	**Dr. Pierre-Antoine GESLIN,** **ElyTMaX, CNRS / Tohoku University,** **Sendai, Japan**		**Prof. Hidemi KATO** **IMR, Tohoku University,** **Sendai, Japan**

Abstract

Background

Nickel-Titanium (NiTi) alloys have very unusual mechanical properties for metallic materials: they display “superelasticity” (large elastic reversible deformation) and “shape memory effect” by which a plastically deformed sample recovers its original shape after heating. Both behaviours are permitted by a phase transformation between two distinct atomic arrangements (the austenite and martensite phases) [1]. Because of these properties, NiTi alloys are used in various applications: the shape memory effect is harnessed in biomedical applications such as stents and temperature-controlled actuators [2]. In addition, the phase transformation triggers an elasto-caloric effect (i.e. a coupling between mechanical stress and temperature), such that these materials are considered for solid-state refrigeration and heating applications [3]. At the moment, these applications mostly rely on bulk NiTi alloys. However, introducing a small scale porosity in NiTi alloy would allow to modify or even improve some properties: it would lower the material weight and elastic stiffness, improve shock absorption properties, which would be

desirable for biomedical applications. Also, introducing an open porosity would increase the exchange surface with fluids, which is interesting for actuators and elasto-caloric applications. In addition to these potential applications, understanding the interplay between shape memory effect and a porous microstructure is a fundamental problem that remains largely unexplored. In this research, liquid metal dealloying (LMD) [4] is used to fabricate porous NiTi alloys with open porosities. LMD relies on the mixing enthalpy between elements to promote the selective dissolution of an element of an alloy into a liquid metal bath. Upon dissolution of this sacrificial element, the remaining element self-assembles to form connected ligaments (see Fig. 1.a). By this process, an open porosity can be introduced in the materials (see Fig. 1.b).

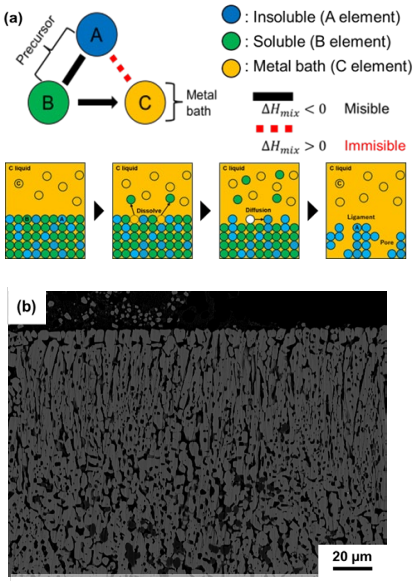

Fig. 1: (a) Concept of LMD
(b) Bicontinuous structure obtained by LMD

Experimental procedures

In this research, Ni_3Ti alloys were selected as precursor alloys and Mg as metallic bath based on mixing enthalpy (see Fig. 2). NiTi-Mg composites were prepared by immersing the precursor alloys into Mg bath at 850 °C for 30 min, and porous NiTi alloys were obtained by removing Mg component with nitric acid. The samples were characterized by X-ray diffraction (XRD) for crystal structure analysis, and their microstructure and compositions were examined using scanning electron microscope (SEM) and energy dispersive x-ray spectroscopy (EDS). In addition, the solid-state phase transformation temperatures were investigated using differential scanning calorimetry (DSC).

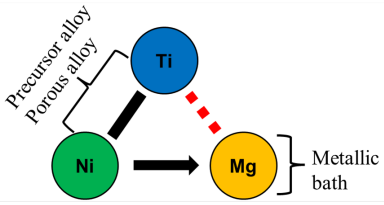

Fig. 2: Reaction design of LMD for fabricating porous NiTi alloy

Results

Using LMD technique, porous NiTi alloys were successfully fabricated, and it was confirmed that crystal structure corresponds to B2 ordered austenite phase, which is high-temperature phase of NiTi alloys (see Fig. 3). According to the compositional analysis by EDS, the porous NiTi alloys contained not only Ni and Ti but also Mg originating from the metallic bath. Also, DSC measurements showed that there were no peaks in the temperature range from -60 to 300 °C, indicating that NiTi alloys obtained by LMD did not undergo phase transformation in the temperature range.

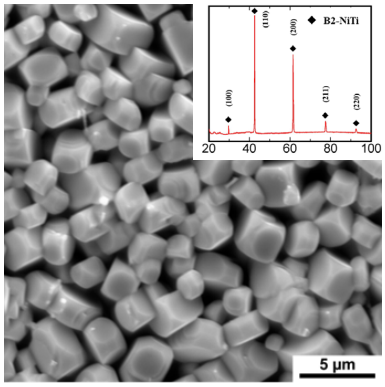

Fig. 3: Porous NiTi alloys fabricated by LMD

References

[1] D. Mantovani, *JOM*, 52(2000), 36-44.
[2] J. M. Jani et al., *Mater. Des.*, 56(2014), 1078-1113.
[3] J. Cui et al., *Appl. Phys. Lett.*, 101(2012), 073904.
[4] T. Wada et al., *Mater. Lett.*, 65-7 (2011), 1076-1078

Surface engineering of ZnO nanorods

ELyT Global

Theme (to precise)
Scientific topic (to precise)

Dr Alexandra Apostoluk

Lyon Institute of Nanotechnologies, INL, INSA Lyon, France

T. Dedova[1], B. Masenelli[2], D. Priano[3], S. Danièle[3], M. Sypniewska[4], M. Kriisa[1], A. Katerski[1], I. Oja Acik[1]

[1]Laboratory for Thin Film Energy Materials, Tallinn University of Technology, Tallinn, Estonia

[2]Lyon Institute of Nanotechnologies, INL, INSA Lyon, France

[3]Laboratory of Catalysis, Polymerization, Processes and Materials, CPE, Lyon, France

[4]Bydgoszcz University of Science and Technology, Bydgoszcz, Poland

Abstract

Zinc oxide (ZnO) nanostructures have garnered considerable interest due to their wide range of applications, particularly in solar energy conversion and photocatalysis. Nanostructuring significantly enhances the photocatalytic performance of ZnO by increasing its specific surface area, which promotes their adsorption of pollutant molecules. Moreover, the efficient photoinduced charge separation and transfer processes in ZnO enable the degradation of organic contaminants under UV or visible light, making it a promising material for wastewater treatment applications [1].

Precise control over crystallite size and morphology through controlled synthesis methods allows the tuning of ZnO's electronic band structure to meet specific photocatalytic requirements. In addition, surface decoration and modification of ZnO nanorods with appropriately selected functional groups further enhances their photocatalytic efficiency. Defect engineering also emerges as a powerful approach to improve photocatalytic activity; the intentional introduction of defects within the crystal lattice and electronic structure favorably

influences light absorption, charge carrier separation and mobility, as well as surface reaction kinetics.
Owing to defect-related wide-band emission, ZnO nanostructures are also attractive candidates for down-shifting applications in solar cells, where they can effectively convert high-energy photons into wavelengths better matched to the spectral response of photovoltaic devices [2]. We present recent studies on ZnO nanorods with engineered surfaces to obtain hydrophilic or hydrophobic surfaces and their characterization by spectroscopic techniques.

References:
[1] P. Gaffuri, T. Dedova, E. Appert, M. Danilson, A. Baillard, O. Chaix-Pluchery, . Güell, I. Oja-Acik, V. Consonni, Enhanced photocatalytic activity of chemically deposited ZnO nanowires using doping and annealing strategies for water remediation, Applied Surface Science 582, 2022, 152323, https://doi.org/10.1016/j.apsusc.2021.152323
[2] A. Apostoluk, D. Priano, M. Sibinski, K. Znajdek, S. Danièle, B. Masenelli, Zinc Oxide Nanoparticles for White Light-Emitting Diodes and Solar Cells. *Mastering Optoelectronics - Fundamentals, Applications, and Innovations [Working Title]*, IntechOpen, 2025, 10.5772/intechopen.1011840

MOREOVER project: Design of an EIS-based sensor for non-invasive in-field corrosion monitoring

ELyT Global
Energy
Surfaces and interfaces

 Z. Dong[1,2,3]	 H. Abe[1]	 B. Ter-Ovanessian[3]	N. Mary[2] Y. Watanabe[1,2] B. Normand[3]

Affiliation

[1] *Graduate School of Engineering, Tohoku University, 6-6-01-2 Aoba, Aramaki, Aoba-Ku, Sendai, Japan*
[2] *ELyTMaX UMI 3757, CNRS–Université de Lyon–Tohoku University, International Joint Unit, Sendai, Japan*
[3] *INSA-Lyon, UCBL, UMR CNRS 5510 MATEIS,69621 Villeurbanne Cedex, France*

Abstract

1. Background

Nuclear power constitutes a significant component of both the French and Japanese energy source combinations. Its ongoing operation and expansion are essential for realizing decarbonized energy goals. Nevertheless, effective management of nuclear waste remains a crucial factor influencing public acceptance and perception. The French Nuclear Safety Authority (ASNR) classifies nuclear waste into two categories based on its radioactivity levels and lifespan: "short-lived" and "long-lived". "Short-lived" waste originates from activities such as the operation, maintenance, and decommissioning of nuclear power plants, including items like filters, used components, tools, and debris. On the other hand, "long-lived" waste primarily results from the processing of spent nuclear fuel. Geological disposal is internationally recognized as the benchmark solution for managing the most hazardous, long-lived radioactive waste.

The objective of a geological repository is to preserve both humanity and the environment from the effects of radioactive waste by containing radioactivity for up to several hundred thousand years. Most repository systems rely on multiple natural and/or artificial barriers to prevent the migration of radionuclides into the biosphere. Regardless of the chosen approach, an extended corrosion period can occur on the overpack material (such as copper or non-alloyed steel) under specific environmental conditions. However, limited knowledge exists regarding the long-term

behavior of these materials when exposed to such environments that may change over extended periods.
Since corrosion tests at the lab typically occur over short durations relative to the repository's timescale, mechanistically based modeling of corrosion product composition, formation mechanisms, and growth rates is necessary to forecast long-term behavior accurately. To propose consistent models, initial data acquisition is crucial. In this regard, archaeological artifacts serve as valuable resources, providing a database for validation and detailed investigation to validate the model. In this study, in collaboration between INSA Lyon, Tohoku university and the National Research Institute for Cultural Properties in Nara, one approach involves conducting descriptive and quantitative analyses on samples of copper or iron alloys, referred to as archaeological analogs, which have experienced corrosion during burial for approximately 1,000 years. Nevertheless, legal regulations governing the protection of cultural heritage allow for chemical and physical characterization of excavated cultural objects using non-destructive techniques that preserve their value. This work developed and validated an easy-to-set-up and non-invasive method for rapid, damage-free EIS measurements. The method employs a sensor consisting of two additively manufactured electrochemical cells filled with agar-based solid electrolytes. The employed electrolyte is simple to prepare, and the sensor accommodates different sample geometries. Impedance measurements are performed simply by placing the cells on the sample surface, without direct metal contact [1].

2. Achieved results

The potentiality of the sensor was assessed, from model systems using bare and coated copper wafers, to artificially aged steam-oxidized carbon steel coupons, atmospheric-corroded steel plates, and finally, 8th-century Japanese iron archaeological artifacts. The spectra measured on bare copper revealed a significant contribution from the sensor impedance at low frequencies; a corresponding data-processing procedure was developed to subtract this effect. After correction, non-invasive spectra closely matched those obtained by conventional EIS. Measurements on alumina-coated copper showed spectra of a fine coating, with its thickness determined from EIS results consistent with the wafer specifications. Observations on steam-oxidized steels showed decreased impedance with oxidation time and thickness increasing, validating the development of a porous and conductive corrosion layer commonly seen in this condition. For atmospheric-corroded steel samples, the method successfully distinguished the difference in layer morphology from samples of similar composition and comparable layer thickness. Measurements on archaeological artifacts indicated a low-impedance system. The spectra exhibited diffusion-controlled features, suggesting a highly porous corrosion layer.
Finally, this preliminary work has established the measurement methodology for the non-invasive EIS sensor and demonstrated its capability to provide reliable impedance spectra across a range of corrosion systems. Although difficulties were encountered in certain spectra interpretation, comparative validation with conventional EIS confirmed that these difficulties originate from the complexity of the EIS technique itself, and not from limitations of the non-invasive approach.
The method is therefore presented as a convenient, versatile, and promising tool to advance the application of EIS in non-invasive characterization and in situ corrosion studies.

[1] Dong Z, Ter-Ovanessian B, Abe H, Mary N, Watanabe Y, Normand B. *Corrosion Science 2025;254:113029. https://doi.org/10.1016/j.corsci.2025.113029.*

Saturday, March 7th

Afternoon

ELyT Global

Advanced High temperature Processing Platform For The Development Of Novel Materials @ MATEIS Laboratory

	**Florian Mercier** **MATEIS**		

Abstract

The laboratory MATEIS at INSA-LYON has expertise in multi technics to develop new materials.

Since more than 15 years, we apply this expertise in a scientific platform for high temperature processing of materials.

MATEIS have testing machines that can simulate a wide variety of thermal/mechanical metallurgical situations. Starting with the basic treatment of metals to obtain specific structure and proceeding through the testing of specimens taken from finished products, we can simulate and provide test data on almost any thermal/mechanical exposure the material sees during its life.

After a short presentation of the equipment available inside the platform i.e. the Spark Plasma Sintering (SPS), the Hot press (HP), the Gaz Plasma Sintering (GPS) and the Gleeble thermomechanical simulator, I will present some results obtained at MATEIS in collaboration with Tohoku University.

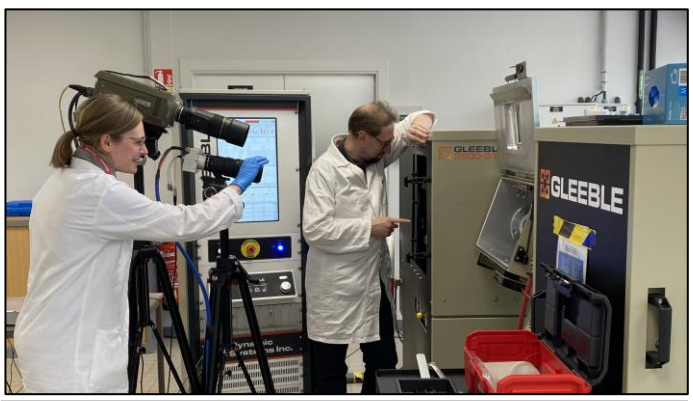

Maëlle Moor and Florian Mercier @2025

Synchronising Microstructure Control and Machinability in L-PBF Titanium Alloys

ELyT Global
Theme (Engineering for Health)
Scientific topic (Materials & Structure Design)

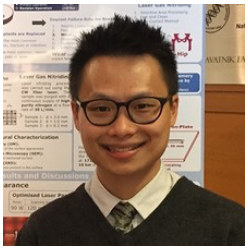	**Dr. Chi-Ho Ng** **Institute for Materials Research, Tohoku University, Sendai, Japan**		**Prof. Kenta Yamanaka** **Institute for Materials Research, Tohoku University, Sendai, Japan**
	**Prof. Michael Bermingham** **Centre for Advanced Materials Processing and Manufacturing, School of Mechanical and Mining Engineering, The University of Queensland**		**Prof. Damien Fabregue** **Université de Lyon, INSA Lyon**

Abstract

While modified titanium alloys produced by Powder Bed Fusion (PBF) exhibit excellent mechanical properties, their post-production machining remains a key challenge for large-scale industry. This study tackles this issue by using Beta-isomorphous elements as strategic additives to improve grain structures while boosting strength and ductility. Importantly, these modifications significantly reduce machining forces and energy consumption, addressing common challenges in finishing near-net-shape parts produced by additive manufacturing. By offering an easy way to balance metallurgical control with better machinability, this work provides a crucial "novel solution" that makes high-performance and manufacturability achievable together.

Copper Metallization on Oxide Ceramics by Low-Pressure Cold Spray and Its Deposition Mechanism

	**Prof. Kazuhiro OGAWA** **Tohoku University**		**Dr. Minjae YU,** **Dr. Hiroki SAITO,** **Assoc. Prof. Yuji ICHIKAWA** **Tohoku University**

Abstract

In the academic year 2024, we demonstrated the feasibility of copper metallization on oxide ceramic substrates using low-pressure cold spray (LPCS) technology. By employing Cu-Al composite powders, particularly the Cu-70 composition (70 vol% Cu, 30 vol% Al), we achieved coatings with favorable thickness, copper content, and low porosity. This initial study also highlighted the importance of oxide ceramics—especially zirconia—for achieving higher deposition efficiency, and suggested that oxygen mobility from the ceramic substrate may play a critical role in the adhesion mechanism.

In the academic year 2025, our research progressed significantly from feasibility to optimization and mechanistic understanding. We systematically investigated the influence of LPCS operational parameters, including gas pressure and stand-off distance, on coating performance. The optimized condition of 0.6 MPa gas pressure and 10 mm spray distance enabled the formation of dense copper-rich coatings with thicknesses up to 240 μm and copper content reaching 70%. Comparative studies between alumina and zirconia substrates revealed that zirconia consistently yielded thicker coatings, likely due to its higher surface temperature and oxygen diffusivity.

To further enhance deposition, we introduced surface pre-treatment techniques such as laser texturing and heat-assisted laser treatment. These methods increased surface roughness and oxygen content, respectively, both of which contributed to improved coating adhesion and thickness. The application of bond coatings (pure Al and Cu-70) enabled the successful deposition of pure copper layers, overcoming the limitations of direct copper spraying.

Mechanistic insights were obtained through micro-tensile testing and transmission electron microscopy (TEM) with energy-dispersive spectroscopy (EDS). These analyses revealed that, unlike metal substrates where adhesion is localized at particle edges, ceramic substrates exhibit uniform tensile strength across the particle interface. The breakage of native oxide films and subsequent oxygen diffusion from the ceramic substrate to the metal particles were identified as key factors enabling strong metallurgical bonding. Furthermore, aluminum's higher plasticity and adhesion strength were shown to facilitate copper deposition in composite powders.

Together, these findings represent a substantial advancement from the initial demonstration of LPCS-based ceramic metallization. The study of the academic year 2025 not only optimized the process for practical application but also provided a detailed understanding of the interfacial phenomena governing metal-ceramic bonding. These insights contribute to the development of reliable, low-temperature metallization techniques for next-generation power electronic modules.

Robust Multi Objective optimization design approaches Acronym of the ELyT project MuORode

ELyT Global

Project ELyT lab: R7 – Robust Multi Objective optimization design approaches

	**Koji SHIMOYAMA[1]**		**Frédéric GILLOT[2]**
	**Hiroshi, SUITO[3]**		**Sébastien BESSET[2]**
	**Sonia MAHMOUDI[3,4]**		**Thanasak, WANGLOMKLANG[2]**

[1] *Department of Mechanical Engineering, Kyushu University, Japan*

[2] *Ecole Centrale de Lyon, LTDS DySCo Team, Lyon, France*

[3] *Advanced Institute for Materials Research, Mathematical Science Group, Tohoku University, Japan*

[4] *RIKEN, Center for Interdisciplinary Theoretical and Mathematical Sciences (iTHEMS), 2-1, Hirosawa, Wako, Saitama 351-0198, Japan*

Abstract

Long-term international collaborations within the ELyT framework have enabled the development of advanced methodologies for robust multi-objective optimization of complex mechanical and vibro-acoustic systems. These systems are typically characterized by highly complex behaviors, strong sensitivity to uncertainties, and prohibitively expensive numerical evaluations.

Within the collaboration with Prof. Shimoyama (Kyushu University), this research has focused on robust shape optimization for aircraft cabin noise reduction. The complex nature of spatial sound distribution inside aircraft cabins requires efficient optimization strategies. This challenge is addressed by defining expensive numerical evaluations through Kriging and Co-Kriging metamodels to manage multi-fidelity

data. The multi-objective formulation leads to Pareto-optimal solutions minimizing both the mean value and the standard deviation of the Sound Pressure Level (SPL) under operational uncertainties.

More recently, in response to the growing demand for advanced sound-absorbing materials in aerospace and transportation applications, a collaboration with Prof. Mahmoudi (Tohoku University) has been initiated on the AI-driven design of woven materials for enhanced sound absorption. This approach relies on a semi-supervised convolutional autoencoder (Semi-ConvAE) architecture to extract low-dimensional representations from micro-structural unit cells. A Gaussian Process Regression (GPR) model is subsequently employed to predict absorption coefficients from the latent space, enabling efficient optimization of complex material geometries.

Current research activities are extending these methodologies toward more realistic aircraft noise prediction by incorporating turbulent boundary layer (TBL) excitation and spatially distributed noise source models, which represent the dominant noise generation mechanisms during cruise conditions. Ongoing developments on shape optimization and sound-absorbing liner material design aim at mitigating vibro-acoustic coupling effects while ensuring robustness against operational and material uncertainties.

1. Achieved results

The proposed robust optimization framework has been successfully applied to various vibro-acoustic design problems. Recent developments by Thanasak Wanglomklang have focused on the integration of neural-network-based two-stage robust shape optimization and hybrid energy-based modeling methods for mid-to-high frequency acoustics. The corresponding results have been presented and published in international peer-reviewed journals.

Currently, Thanasak Wanglomklang is continuing his research as a JSPS Short-Term Postdoctoral Fellow (April 2026 – March 2027), with a focus on deep learning methodologies for inverse design and robust optimization problems in acoustics.

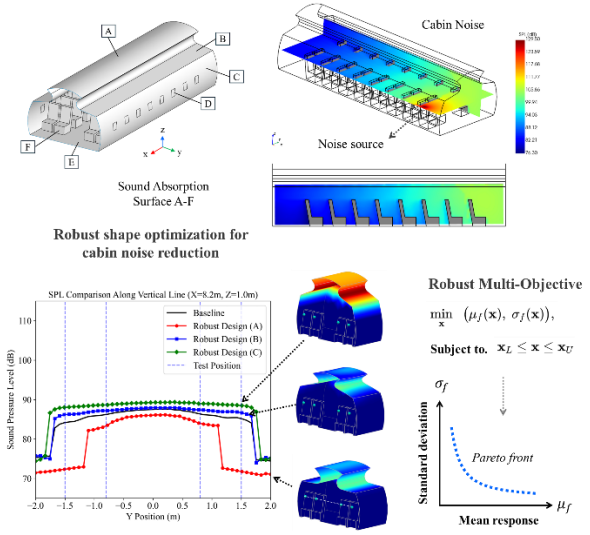

Figure 1: Robust shape optimization for cabin noise reduction

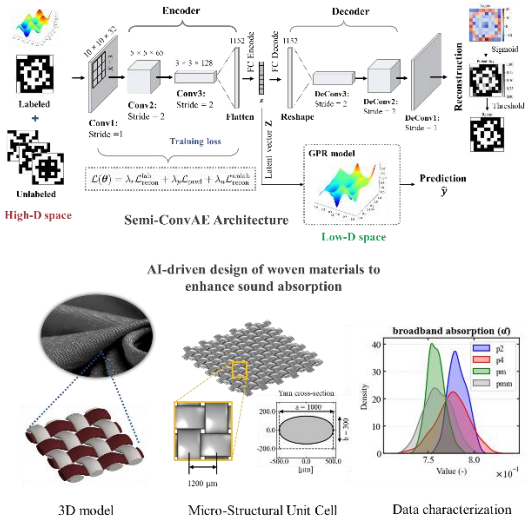

Figure 2: AI-driven design of woven materials to enhance sound absorption

References :

[1] Wanglomklang, T., Shimoyama, K., Gillot, F., & Besset, S. (2025). Neural-network-based two stage robust shape optimization for acoustic noise reduction in an aircraft cabin. Engineering Optimization, 1–19.

[2] Wanglomklang, T., Gillot, F., Besset, S., and Mahmoudi, S. (2025). Vibro-Acoustic Modelisation of Periodic Woven Structures Dedicated to Multi-Objective Shape Optimization. ICFD 2025, Sendai, Japan, November 10-13, 2025.

Dynamic Monte Carlo Simulations of Turing Pattern

F. Kato, H. Koibuchi, M. Nakayama, S. Tasaki and T. Uchimoto

Abstract

We present the dynamic Monte Carlo (DMC) data calculated on two-dimensional triangular and square lattices undergoing periodic sine and square wave deformations. No lattice fluctuation is considered, meaning no movement of pigment cells is assumed for biological patterns. The DMC data exhibit hysteresis behavior in the order parameters of the internal degree of freedom (IDOF) variable, denoted by $\vec{\tau}$, which corresponds to Turing pattern direction. Hysteresis behavior is also observed in some other physical quantities.

1. Introduction

The dynamic Monte Carlo (DMC) technique was developed to study the experimentally observed hysteresis behaviors in the magnetization of ferromagnetic materials [1,2]. In DMC simulations of ferromagnetic models, such as the Ising model, the external magnetic field is periodically varied. Consequently, the DMC simulations can account for hysteresis delays in the magnetization of ferromagnetic materials.

In the FG modeling of Turing patterns (TPs) composed of activator u and inhibitor v, the internal degree of freedom (IDOF) has been shown to significantly influence the relaxation process, during which an increase in entropy is expected [3]. However, the hysteresis behavior of physical quantities under periodic external stimuli remains unclear in the TP system, despite the observation of a maximal entropy state numerically [3]. In this presentation, we demonstrate that TPs respond to the periodic lattice deformation and exhibit hysteresis behavior depending on the lattice structure, which represents the interaction network for pigment cells.

2. Lattices and Periodic deformations

In this presentation, we use 2D triangular and square lattices (Figs. 1(a),(b)). The lattice deformation is defined as

$$L_x = (1 \pm r)L_x^0, \quad L_y = (1 \pm r)L_y^0, \tag{1}$$

where L_x, L_y denote the side lengths and L_x^0, L_y^0 are their original undeformed ones.

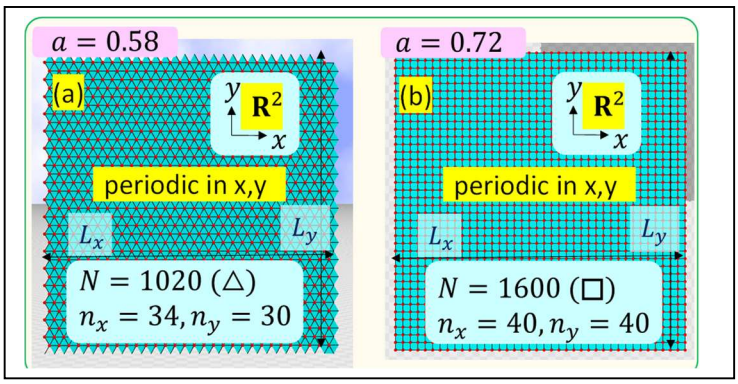

Fig.1 (a) Triangular and (b) square lattices used in the DMC simulations. Lattice vertices (small dots) correspond to pigment cells in biological patterns. The lattice shape is deformed by the deformation ratio r in Eq. (1). The square lattice is symmetric under a $\frac{\pi}{2}$ rotation, whereas the triangular lattice is not.

The deformation ratio r is varied in two different ways; square and sine deformations, such that

$r = 0.2$ (square wave), $r = 0.2\sin(2\pi\tilde{t})$ (sine wave), (2)

where $\tilde{t}$ in $\sin(2\pi\tilde{t})$ corresponds to the MC iteration.

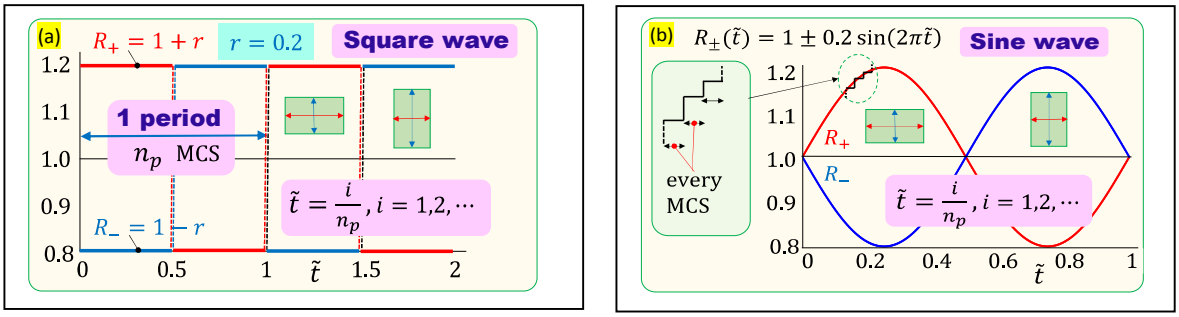

Fig.2 (a) The square wave by the deformation parameters $R_\pm = 1 \pm 0.2$ and (b) the sine wave by $R_\pm(\tilde{t}) = 1 \pm 0.2\sin(2\pi\tilde{t})$. This $R_\pm(\tilde{t})$is periodically changed as a function of $\tilde{t} = \frac{i}{n_p}$, where$i$ denotes i-th MC sweep (MCS) for the update of $\vec{\tau}$, and n_p denotes the total number of MCS for one period. The value of $R_\pm(\tilde{t})$ in the sine wave is updated every MCS.

3. Results

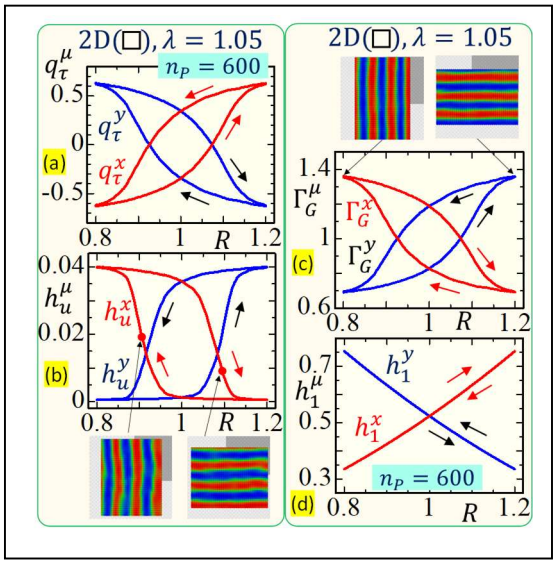

Fig.3 (a) Order parameters $q_\tau^\mu, (\mu = x, y)$ vs. R, (b) diffusion energies $h_u^\mu, (\mu = x, y)$ vs. R, (c) effective tension coefficient $\Gamma_G^\mu, (\mu = x, y)$ vs. R, and (d) Gaussian bond potential $h_1^\mu, (\mu = x, y)$ vs. R of the 2D square model. The hysteresis delays are symmetric under the deformation.

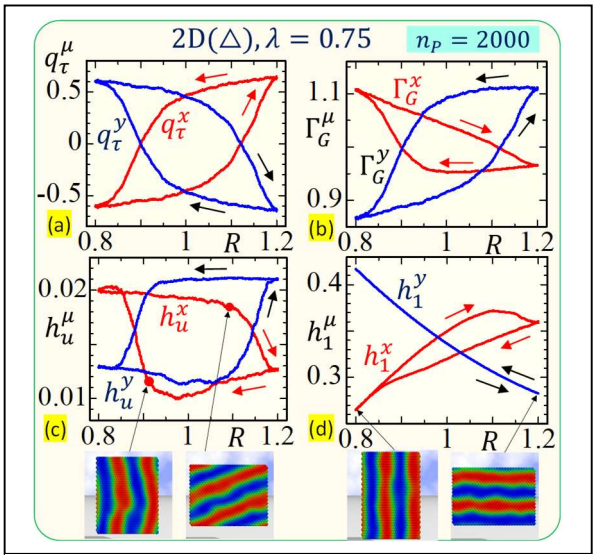

Fig.4 The DMC data obtained on the 2D triangular lattice. The anisotropy in the triangular interaction network is reflected in the direction-dependent or nonsymmetric hysteresis delays.

$$q_\tau^\mu = 2\left(\frac{1}{N}\sum_i(\vec{\tau}_i \cdot \vec{e}^\mu)^2 - \frac{1}{2}\right), (\mu = x, y)$$

$$\vec{e}^x = (1,0), \vec{e}^y = (0,1).$$

4. References

[1] M. Rao, et. al., Phys. Rev. B, 42, 856-884 (1990), https://doi.org/10.1103/PhysRevB.42.856.

[2] W.S. Lo et. al., Phys. Rev. A, 42,7471-7474(1990), https://doi.org/10.1103/PhysRevA.42.7471.

[3] F. Kato, et.al., Soft Matter, 21, 2317-2338 (2025), https://doi.org/10.1039/D4SM01309C.

Effect of non-equilibrium state on the C drift velocity in iron with electric field

ELyT Global

Theme :Energy

Scientific topic : Simulation and modeling

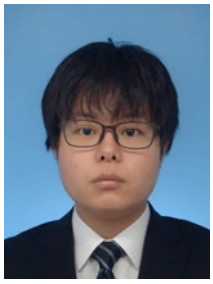	**Mr. R. Onozuka** **（Institute of Fluid Science, Tohoku University, Japan），（Graduate School of Engineers, Tohoku University, Japan），(MATEIS, INSA-Lyon, France)**		**Dr. C. Adessi** **（Institut Lumière Matière, University Claude Bernard Lyon 1,France）**
	**Prof. J. Kioseoglou** **（COSSPHY, Theoretical and Computational Solid State Physics, Aristotle University of Thessaloniki, Greece）**		**Prof. P. Chantrenne** **(MATEIS, INSA-Lyon, France)**
	**Prof. T. Tokumasu** **（Institute of Fluid Science, Tohoku University, Japan）**		

Abstract

In the field of thermal treatment for metals, the use of Joule heating produced by renewable energy or nuclear power has attracted attention because of its advantages (e.g. the absence of greenhouse gas emissions, high energy efficiency, and short processing time). Previous studies have shown that carbon migration in iron under an electric field indicates unique behavior and this behavior may influence the kinetics of phase transformation in Fe–C alloys [1,2]. However,

the mechanism underlying this unique carbon migration has not yet been fully understood. In our project, we have tried to clarify this mechanism using simulation, modeling, and experimental approaches. We analyzed both body-centered cubic (BCC) and face-centered cubic (FCC) structures for iron crystal. These results suggest that the migration mechanism can be attributed to non-equilibrium effects induced by the electric field and higher-order derivative terms in Fick's law. The details of our study are presented below.

・Simulation and modeling part

We developed an analytical model based on the 3D Maxwell–Boltzmann distribution to reproduce the drift velocity of carbon in Fe–C alloys under the electric field [3]. This model requires the energy barrier for migration, vibration frequency of carbon as parameters input. The energy barrier was evaluated from an Arrhenius plot of the diffusion coefficient obtained from equilibrium MD simulations. The analytical model is highly sensitive to the energy barrier. Therefore, it is necessary to calculate the diffusion coefficient of carbon with high statistical accuracy in order to determine the energy barrier reliably. For this purpose, we performed 200 identical simulations with different initial velocities to improve the statistical accuracy of the calculated diffusion coefficient. On the other hand, we performed the same simulation 100 times to obtain the drift velocity. Figure 1 shows the results for the FCC structure: the analytical model without non-equilibrium effects (red line), the drift velocity obtained from the slope of carbon displacement in molecular dynamics (MD) simulations (blue symbols), and the Nernst–Einstein relation (green line). At low electric field strength, the analytical model shows good agreement with the Nernst–Einstein relation, whereas a large discrepancy appears at high electric field strength. We have considered that this discrepancy is attributed to non-equilibrium effects because a relaxation period is observed at high electric fields, as shown in Fig. 2. In other words, the local temperature of carbon becomes higher than that of the surrounding iron lattice. This temperature difference leads to a transfer of kinetic energy from carbon to iron crystal, as a result, carbon requires more energy than the migration energy barrier in the absence of an electric field. When this energy transfer is taken into account by assuming an additional term of $\frac{eZ^*Ea_0}{4}$, the analytical mode is modified as shown by purple line in figure 1. In the analytical model including non-equilibrium effects, good agreement with the MD results is obtained at high electric field strength. However, a discrepancy between this model and the Nernst–Einstein relation appears at low electric field strength. This is reasonable because non-equilibrium effects can be neglected in the low-field regime.

・Experimental part

Several experiments have been performed to analyze the carbon migration in Fe-C alloys under electric field. The experimental setup is shown in Figure 3.

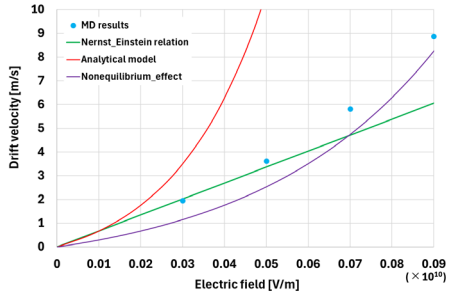

Fig. 1 Analytical model

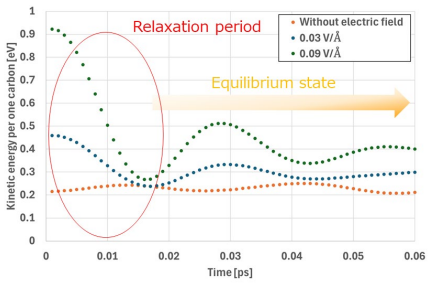

Fig 2 Relaxation period

Fig. 3 Experimental setup

References

[1] P. Chantrenne, M. Monzey, D. Fabrègue, G. Pierre, P. Michel, M. Florian, Metall Mater Trans B 54, (2023), 2454–2466.

[2] R. Onozuka, P. Chantrenne, T. Tokumasu, *Proc. 22th ICFD*, (2025), 1759-1761.

[3] R. Onozuka, C. Adessi, J. Kioseoglou, P.Chantrenne, T. Tokumasu, ABSTRACTS BOOK ELyT workshop 2025, (2025), 54-55.

Exploring Complex Intermetallics and Quasicrystal Approximants as Catalysts

ELyT Global
Computational Mechanics & Data-Driven Modeling

Prof. Emilie Gaudry

Université de Lorraine, CNRS UMR7198, IJL Campus Artem, Nancy, France

Abstract

Intermetallic compounds are attracting increasing attention in heterogeneous catalysis. Unlike conventional multimetallic systems, they exhibit well-defined electronic structures and catalytic behaviors that allow them to be regarded as “pseudoelements.” Their unique surface morphologies and electronic properties can also enable novel reaction pathways, offering enhanced selectivity and reactivity compared to traditional catalysts.

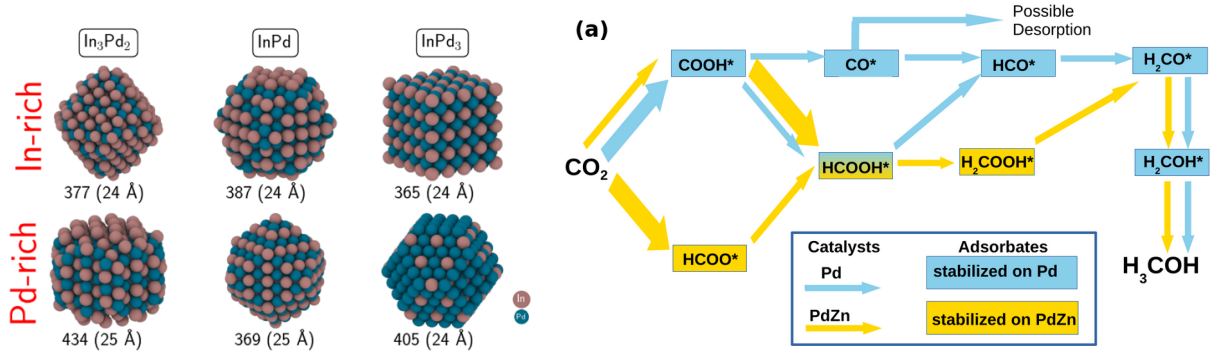

Fig. 1. (a) Morphologies of In_3Pd_2, InPd and $InPd_3$ nanoparticles based on the Wulff construction.[1] **(b)** Scheme illustrating the control of the reaction path for the CO_2 reduction to methanol.[2]

Several case studies will be presented to highlight the distinctive behavior of intermetallic compounds compared with that of pure metals. At the nanoscale, the controlled synthesis of intermetallic nanoparticles remains challenging. Based on the In-Pd binary as a typical system, we show that ordered nanoparticles likely present crystalline forms, the Wulff polyhedron being the most stable morphology in the range of 300-1200 atoms. A noticeable tendency towards amorphisation is observed when disorder is introduced in nanoparticles built from In_3Pd_2 and InPd.[1] From the perspective of catalytic reactivity, focusing on CO_2 hydrogenation to methanol, chosen for its significant environmental and energy importance,

we show that in comparison to Pd, the strong electron-donor character of PdZn weakens the adsorption of carbon-bound species and strengthens the binding of oxygen-bound species. As a consequence, the first step of CO_2 hydrogenation more likely leads to the formate intermediate on PdZn, while the carboxyl intermediate is preferentially formed on Pd (Fig. 1a).[2]

Modeling complex intermetallic catalyst requires advanced methodologies due to their intricate atomic and electronic structures. As a result, recent developments in machine learning have become increasingly essential, offering powerful tools to accelerate quantum chemistry calculations.[3]

In summary, while intermetallics offer exciting prospects in catalysis, their future development requires advanced tools and continued research. Among the available materials, only a few have been explored so far, and much remains to be done.

References: [1] Alexis Front, Clovis Lapointe and Emilie Gaudry, Intermetallics with sp–d orbital hybridisation: morphologies, stabilities and work functions of In-Pd particles at the nanoscale, Nanoscale Horiz., 2024, 9, 1341; [2] F. Brix, V. Desbuis, L. Piccolo, É. Gaudry**,** Tuning Adsorption Energies and Reaction Pathways by Alloying: PdZn versus Pd for CO_2 Hydrogenation to Methanol, *J. Phys. Chem. Lett.* 2020, 11, 18, 7672-7678; [3] Nathan Boulangeot, Florian Brix, Frédéric Sur, and Émilie Gaudry, *J. Chem. Theory Comput* **2024** *20*, 7287-7299

Heat to power energy conversion using natural rubber

ELyT Global
Theme: Energy
Scientific topic: Materials & Structure Design

		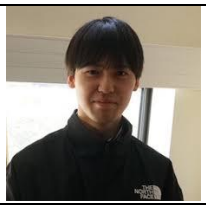		
Gaël SEBALD[a]	Giulia LOMBARDI[a]	Takuma OIRI[b]	Gildas COATIVY[c]	Atsuki KOMIYA[a,b]

[a] *ELyTMaX IRL 3757, CNRS, Univ. Lyon, INSA Lyon, Centrale Lyon, Université Claude Bernard Lyon 1, Tohoku University, Sendai, Japan*
[b] *Institute of Fluid Science, Tohoku University, Sendai, Japan*
[c] *INSA Lyon, LGEF, UR682, Villeurbanne, France*

Abstract

Low-grade heat refers to heat at low temperature, typically below 100°C. It is an abundant energy resource resulting from industrial processes, such as cooling circuits, or surface geothermal systems. It is however difficult to convert it into usable electricity because of the limited Carnot efficiency, but also because of the absence of effective solutions at low scales. Conversion efficiency of thermoelectric modules being low, alternatives techniques need to be developed.

In this presentation, the thermomechanical properties of natural rubber will be presented, followed by an experimental proof of concept of heat to power energy converter. Natural rubber tubes were first pre-elongated to a value ranging between 3 and 6, and then subjected to time variations of temperature, ranging from 15°C to 60°C. The mechanical stress after the pre-elongation varies between 500kPa to 2000 kPa. The temperature cycles showed that the mechanical stress exhibited a strong temperature dependence, with typical values of 9~12 kPa/K. For a 10 K temperature variation, the relative mechanical stress variations may reach up to >20% of the average stress.

An example of characterization is given in Figure 1, showing stress variations of ~200 kPa for temperature variations of 20 K.

A device was then developed using a dual assembly of parallel natural rubber tubes (called REG, for regenerator), as shown schematically in Figure 2. The two rubber systems are mechanically attached to a middle point about to move vertically. The outer ends of the rubber systems were anchored through force sensors, and so that the average elongation of each rubber system is at a value of 5. The motion of the translation table allows modifying the elongation of each rubber system.

To effectively convert heat into mechanical energy, we considered thermodynamic cycles (Otto cycles), consisting of two adiabatic stretching steps, and two iso-elongation heating/cooling steps. To simplify the understanding of the thermodynamic cycles, we describe here Stirling cycles, that are very close in terms of converted energy in our configuration, depicted in Figure 3. Both rubber systems exhibit identical thermodynamic cycles, but in opposite phase. The cycles are repeated several times, and the

energy conversion was quantified. The resulting output energy density is displayed in Figure 4. It was observed also that the converted energy tends to saturate at high temperatures, suggesting that the temperature window of the thermomechanical coupling of natural rubber was reached. Furthermore, operating conditions should be carefully chosen to avoid the effect of the mechanical losses.

The experimental device consisting of 20g of natural rubber exhibited an output mechanical energy of 3.2 J (or 150 mJ/cm^3) with 35 K imposed temperature variations, and elongation varying between 4.5 and 5.5 using Stirling cycles. Considering the cycle period of 34 s, this corresponded to an output mechanical power of 120 mW.

The proposed device is further scalable by increasing the number of parallelized natural tubes, which may constitute a plausible large scale energy production from low temperature heat sources. More details may be found in [1].

[1] Sebald, G., Lombardi, G., Coativy, G., Komiya, A., (2025) "Converting low-grade heat into mechanical energy using a natural rubber elastocaloric device", *Joule*, **9(7)**, 102012. (doi: 10.1016/j.joule.2025.102012)

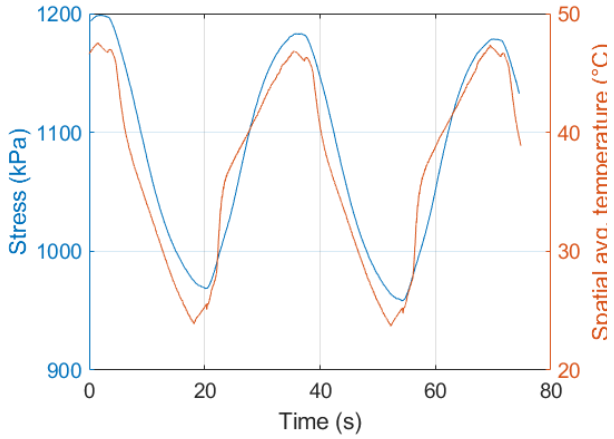

Figure 1: Stress and temperature vs time of natural rubber with a pre-elongation of 6.

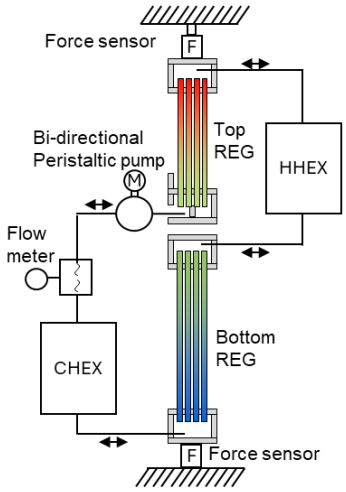

Figure 2: Experimental proof of concept of heat to power energy conversion using natural rubber

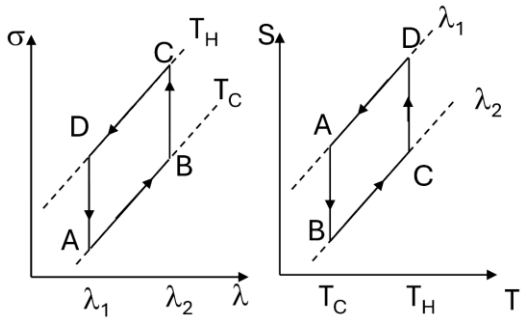

Figure 3: Thermodynamic cycles for heat to power energy conversion in natural rubber

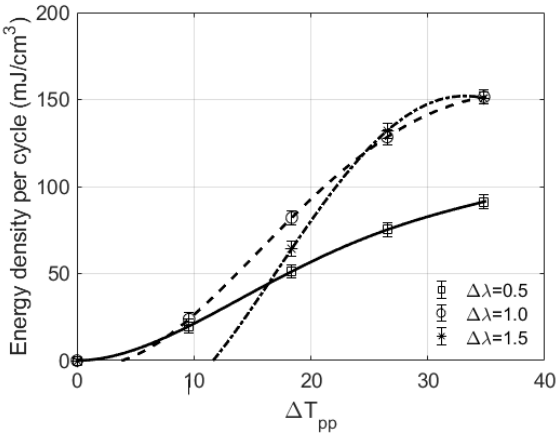

Figure 4: Output energy density for various tested temperature variations and elongation amplitudes

Thermal aggression of a metallic wall by a reacting flow: near-wall gas-phase temperature measurements with laser diagnostics

ELyT Global

Energy - Materials

Combustion with laser-based diagnostics

	**Pradip XAVIER** **Associate Professor** **INSA Rouen Normandie** **Energy Engineering Dpt.** **CNRS CORIA** **Reactive Flows Dpt.**		**Artémis BLONDEL** **PhD student** **INSA Rouen Normandie** **Energy Engineering Dpt.** **CNRS CORIA** **Reactive Flows Dpt.**
	**Alexis VANDEL** **Research engineer** **INSA Rouen Normandie** **Energy Engineering Dpt.** **CNRS CORIA** **Reactive Flows Dpt.**		**Saïd IDLAHCEN** **Research engineer** **INSA Rouen Normandie** **Energy Engineering Dpt.** **CNRS CORIA** **Reactive Flows Dpt.**
	**Frédéric GRISCH** **Professor** **INSA Rouen Normandie** **Energy Engineering Dpt.** **CNRS CORIA** **Reactive Flows Dpt.**		

Abstract

Flame-Wall Interaction (FWI) describes various multi-physical and multi-scale phenomena resulting from the intricate interaction between a solid wall and a reactive flow [1]. With the introduction of new manufacturing processes (e.g. additive manufacturing) and innovative architectures, energy systems must be further optimized in order to reduce pollutants emissions at the wall and enhance the material durability with an improved cooling or heat treatment. To do so, the temperature in the near-wall

region has to be known precisely since significant instantaneous heat losses occurring during FWI are controlled by this key physical scalar.

This study aims to measure the near-wall temperature in the gas-phase using Two-Line Atomic Fluorescence (TLAF) of indium for the first time, to the authors' best knowledge. Temperature is obtained using TLAF via the Boltzmann distribution from the measurement of a ratio of fluorescence, generated by the sequential excitation of two low-lying states of an atom [2].

The platform AURYGA (Atomic fluorescence platform for thermometry in gases) has been developed at CORIA laboratory to allow the seeding of a flame using trimethylindium (TMI) [3]. External-Cavity Diode Lasers (ECDLs) have been chosen as to be able to scan the fine absorption profile of the indium atom, hence enabling to select a calibration-free detection scheme with only one detector [4]. Using this approach, gas-phase temperature is measured inside a conical laminar premixed CH4/air Bunsen flame interacting with a water-cooled plate (304L stainless steel) placed above it (head-on quenching configuration). Results provide the best input parameters (laser energy, seeding concentration, etc.) to perform TLAF in the near-wall region and various post-processing approaches are implemented to retrieve gas-phase temperature.

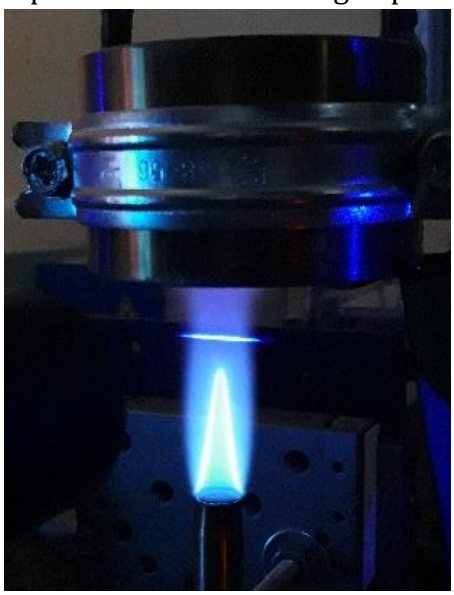

Figure 1: TLAF in a CH4/air flame at Φ= 1.25 interacting with a water-cooled stainless-steel plate

References:

[1] A. Dreizler and B. Böhm. Advanced laser diagnostics for an improved understanding of premixed flame-wall interactions. *Proceedings of the Combustion Institute*, 35:37-64, 2015

[2] C.T.J. Alkemade. A theoretical discussion on some aspects of atomic fluorescence spectroscopy in flames. *Atomic Absorption Spectroscopy*, pages 73-98,1 1970.

[3] R. Whiddon, B. Zhou, J. Borggren, M. Alden, and Z.S. Li. Vapor phase tri-methyl-indium seeding system suitable for high temperature spectroscopy and thermometry. *The Review of scientific instruments,* 86:093107, 9 2015

[4] J. Hult, I.S. Burns, and C.F. Kaminski. Measurements of the indium hyperfine structure in an atmospheric-pressure flame by use of diode-laser-induced fluorescence. *Optics Letters, 29, 2004*

Contact Electrification of High-speed Nanodroplets Impinging on Various Metal Plates under Different Generation Conditions

ELyT Global
Electrostatic
Contact electrification and liquid-solid interface

	**Mr. Jiun-Shian Lee** **Department of Mechanical System Engineering & Institute of Fluid Science, Tohoku University, Japan**		**Dr. Siwei Liu** **Institute of Fluid Science, Tohoku University, Japan**
	**Prof. Yun-Chien Cheng** **Department of Mechanical Engineering, National Yang Ming Chiao Tung University, Taiwan**		**Prof. Toshiyuki Sugimoto** **Graduate School of Engineering, Yamagata University, Japan**
	Mr. Tomoki Nakajima **Institute of Fluid Science, Tohoku University, Japan**		**Prof. Takehiko Sato** **Institute of Fluid Science, Tohoku University, Japan**

Abstract

Charging phenomena of water droplets have been observed and reported for many years. Recently, water droplets have been applied to triboelectric nanogenerators (TENGs). The kinetic energy of a water drop is harvested to produce electricity [1].
In our laboratory, a condensation-based high-speed nanodroplet generator has been built. The charging phenomenon is also observed due to the nanodroplets sprayed on the metal plate. We have tested different materials—lead (Pb), aluminum (Al), iron (Fe), copper (Cu), and tin (Sn)

[2]. The magnitude and polarity of the electric current vary with material, in the order: Pb (18.9 nA), Al (8.0 nA), Fe (-3.2 nA), Cu (-10.6 nA), and Sn (-13.3 nA). Additionally, we investigated the system parameters affecting nanodroplet generation and charging, including vessel pressure, water heater power, and nozzle temperature. This study explores the primary mechanisms of charging phenomena and design factors for future research.

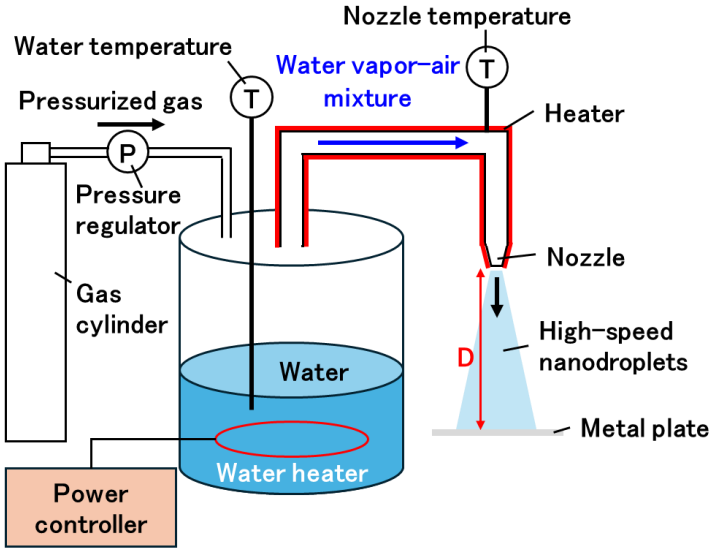

Fig. 1. Schematic of the high-speed nanodroplet generator

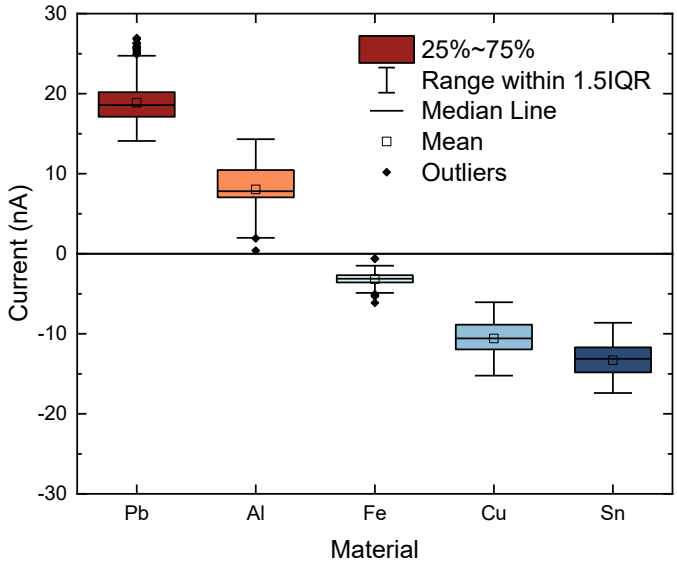

Fig. 2. The electric current of high-speed nanodroplets sprayed on the various metal plates at D = 5 mm

This study was supported by JSPS KAKENHI, Grant Numbers 23KK0265, 25H00405, and 25K17536, the Collaboration Research Project of the Institute of Fluid Science, Tohoku University, and JST SPRING, Grant Number JPMJSP2114.

Reference :

[1] Y. Jin, C. Wu, P. Sun, M. Wang, M. Cui, C. Zhang, and Z. Wang, *Droplet*, vol. 1, pp. 92-109, 2022.

[2] J.-S. Lee, T. Sato, Y.-C. Cheng, T. Sugimoto, T. Nakajima, and S. Liu, *Appl. Phys. Lett.*, vol.127, 091601, 2025.

Sunday,
March 8th

Morning

Self-powered beacon using optimized magnetic energy harvester and ultralow power design

ELyT Global
Theme: Energy
Scientific topic: Materials & Structure design

	**Hanae AOKI** **Graduate School of Engineering, Tohoku University**		**Mickaël LALLART** **LGEF, INSA Lyon**		**Gaël SEBALD** **ELyTMaX IRL 3757, CNRS, Univ. Lyon, INSA Lyon, Centrale Lyon, Université Claude Bernard Lyon 1, Tohoku University**

Abstract

The spreading of wireless autonomous networks has enabled new paradigms in data acquisition and processing, allowing new applications (transportation monitoring, structural health monitoring…). Yet, they raised the challenge of reliable and long-term power supply, which cannot be achieved by primary batteries especially in inaccessible and/or moderately harsh environments ([1]). To address this shortcoming, the concept of "Energy Harvesting", capturing energy from the direct environment of the device and converting it into electricity, has emerged as an appealing solution ([2]). Among numerous sources, mechanical energy is attractive due to its good energy density and wide availability. Yet, associated energy is still quite low, and efficient design of the global device, from the material to the application, is mandatory.

The work reported here is twofold with respect to the previously exposed challenges. First, it aims at exposing an efficient energy harvester based on optimized electromagnetic coupling. Thanks to the optimization of the magnetic flux variation during vibrations, the proposed structure permits achieving significant power output. Second, as an applicative demonstration, it is shown how an ultralow-power sensor can be designed to shape, along with the harvesting structure, a global self-powered node. The ultralow-power achievement is realized thanks to a global optimization of the power management, along with low-level programming.

Magnetic energy harvester design and characterization

To optimize an efficient energy harvester, we propose a bi-stable high-output configuration by optimizing the arrangement of two permanent magnets with a back yoke. Fig. 1(a) depicts the prototype of magnetic energy harvester (EH) based on beam vibration and electromagnetic induction. The EH consists of the soft magnetic core plate (electrical steel) inserted in 3000 turn-coil (360 ohms), which is attached to a free end of the non-magnetic cantilever beam. A pair of permanent magnets were fixed with back yoke to concentrate the magnetic flux in vicinity of coil which enables bi-stable operation without suppressing the beam vibration. The vibration test was performed under its beam resonance frequency at 13 Hz with accelerations

of 1G. Experimentally measured coil voltage was fed into an electronic simulation software (LTSpice) to investigate the harvesting abilities using a LTC3588 harvesting interface (Fig. 1(b)). Hence, from the first oscillation, it can be seen that the system is fully charged and operative after 3,5 periods (125 ms). Considering that both intermediate and output capacitors yields a value of 100µF, this corresponds to a total energy of 1.9mJ, and an average power of 15mW.

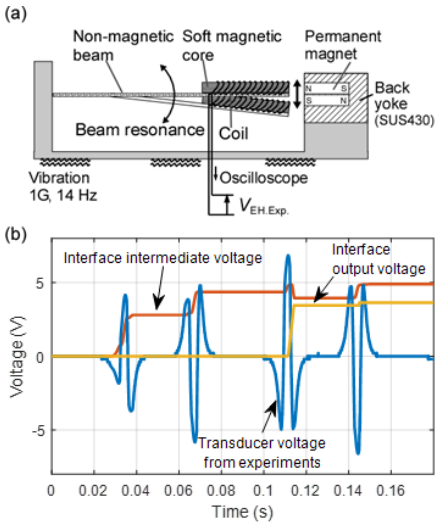

Figure 1. (a) Schematic illustration of a magnetic EH and (b) waveforms of the measured coil voltage and voltages of electronic interface.

Sensor design

In the framework of designing an efficient, globally optimized self-powered sensors, the energy usage is also of primary importance, in addition to the optimization of the harvested energy.

The sensor design has been done with deep constraints in terms of used energy. In terms of topology, a three-stage power scheme has been adopted (Fig. 2), with an harvesting stage featuring the previously exposed LTC3588 converter, a power management (PIC12LF1552) and a sensing a communication module (NRF52840 MCU and CJMCU-2080 sensor). Apart from the hardware point of view, BLE stack and sensor I2C communication were coded at a very low level by directly manipulating registries for drastic energy saving.

In order to evaluate energy required for a sensing and BLE communication cycle, the device was connected to a 470µF capacitor pre-charged at 3.6V. Results shown in Fig. 3 demonstrate a drop in the capacitor voltage from 3.64V to 3.42V, yielding an associated energy of 360µJ. In comparison, a reference STM330 module (EnOcean) shows a consumption of 585 µJ per cycle, which is almost twice than the proposed sensor.

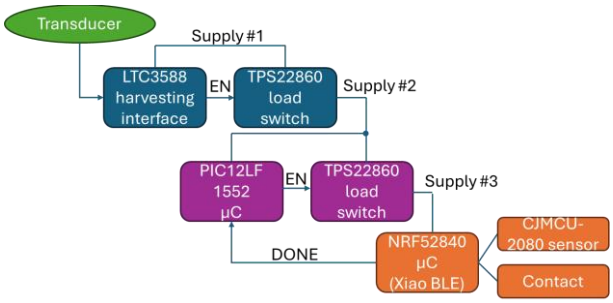

Figure 2. System synoptic.

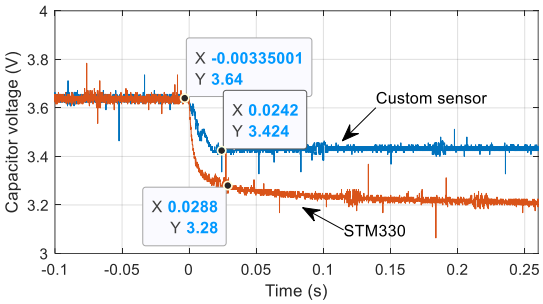

Figure 3. Consumption test waveforms and comparison with EnOcean STM 330.

Conclusion

This study demonstrated the global conception of a full sensor node able to collect its electrical energy from ambient vibrations. By a global view taking into account the energy balance of the systems (i.e. available energy vs. required one), an optimized harvester able to output 15 mW is presented, and a specific sensing node able to perform measurement and BLE communication with a few hundreds of microjoules is designed. Hence, through a comprehensive understanding of the involved energy from the source to the application, this allows envisioning new opportunities for the development of self-powered devices.

References

[1] J. VanZwol, Power Electronics Technology, July 2006, 40–45, 2006.

[2] F. K. Shaikh and S. Zeadally, Renew. Sust. Energy Rev., 55, 1041-1054, 2016.

DMD analysis of the length-to-diameter ratios for flow passing through a cylinder with its axis parallel to the flow direction

ELyT Global

Fluid flow, transportation, heat transfer
Turbulent simulation, Mode decomposition, Stability

	**Hiraku YATA** **PhD. Student** Akita University		**Prof. Takahiro ADACHI** Akita University
	**Prof. Atsuki KOMIYA** **Tohoku University**		**Prof. Valéry BOTTON** **Lyon INSA**

Abstract

The flow past a three-dimensional circular cylinder whose axis is aligned with the freestream direction is investigated by large-eddy simulation (LES), with particular attention paid to the dependence of the drag coefficient on the length-to-diameter ratio (*l/d*) of cylinder as shown in Fig.1. It is well known that the aerodynamic drag of bluff bodies is strongly influenced by the wake structure, and previous experimental studies have reported that the drag coefficient varies with the *l/d* ratio of the cylinder. However, a clear relationship between the drag coefficient and the underlying flow mode has not been fully established, mainly due to experimental difficulties such as support interference effects.

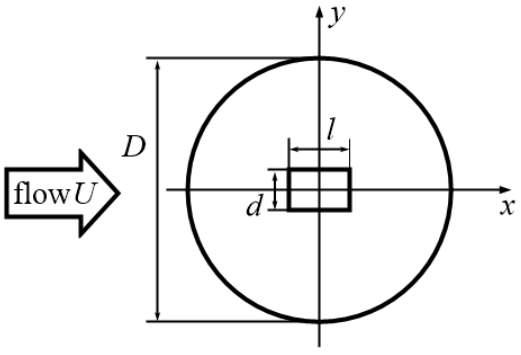

Fig. 1 Physical model and Co-ordinates.

In the present study, numerical simulations are performed in order to systematically examine the effect of the *l/d* ratio on the drag characteristics and the corresponding flow dynamics. The flow is assumed to be turbulent, and LES is adopted with the WALE subgrid-scale model. The governing equations are solved using OpenFOAM. A cylindrical body with diameter *d*=100 mm is placed in a spherical computational domain of *D*=7*d* (700mm), and a uniform inflow with velocity *U* =

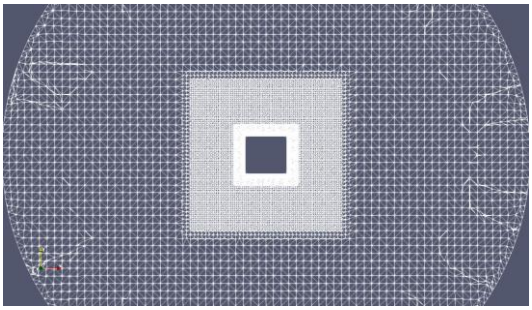

Fig. 2 Mesh distribution

7 m/s and a kinematic viscosity of ν =1.501 Pa·s is imposed parallel to the cylinder axis. The Reynolds number, defined as $Re = Ud/\nu$, is fixed at $Re = 4.6 \times 10^4$. The l/d ratio defined as a ratio of length to diameter is varied in the range of l/d=0.4–2.2.

The computational mesh is generated using cfMesh based on an octree refinement strategy shown in Fig.2. The finest grid resolution is set to 2.5 mm in the vicinity of the cylinder, while the mesh is gradually coarsened toward the outer region. Four refinement levels are employed so that the cell size at the outer boundary becomes 16(= 2^4) times larger than the minimum resolution. This mesh configuration enables an adequate resolution of the near-body flow and wake structures while maintaining reasonable computational cost.

As a representative result, we show the temporal evolution of the drag and lift coefficients in Fig. 3. The drag coefficient primarily originates from the pressure acting on the upstream end face of the cylinder, whereas the lift coefficient fluctuates around zero because the lift direction is orthogonal to the main flow. A comparison of the time series for different aspect ratios indicates that the characteristic oscillation frequency of the drag coefficient changes with l/d. In particular, consistent with previous experimental observations[1], the dominant frequency for l/d = 2.0 is approximately twice that for l/d = 1.0. This behavior suggests that the dominant flow mode differs depending on the aspect ratio, and that a transition in the wake structure may occur between these two cases.

The distribution of the time-averaged drag coefficient as a function of the aspect ratio is depicted in Fig.4 and also exhibits a qualitative change around $l/d \approx 1.5$. Although the detailed mechanism remains unclear, this tendency implies the possible existence of a transition region in which the dominant wake dynamics are altered. To further investigate this issue, Fourier spectral analysis of the drag coefficient time series is carried out to identify the dominant frequencies and characteristic periods. Based on these results, dynamic mode decomposition (DMD) is applied to the flow field data obtained from the LES. Since DMD enables the extraction of coherent spatio-temporal structures directly from numerical data, it is expected to provide insight into the dominant flow modes governing the drag behavior.

The objective of this study is to clarify the relationship between the transition of dominant flow modes and the corresponding change in the drag coefficient for freestream-aligned circular cylinders.

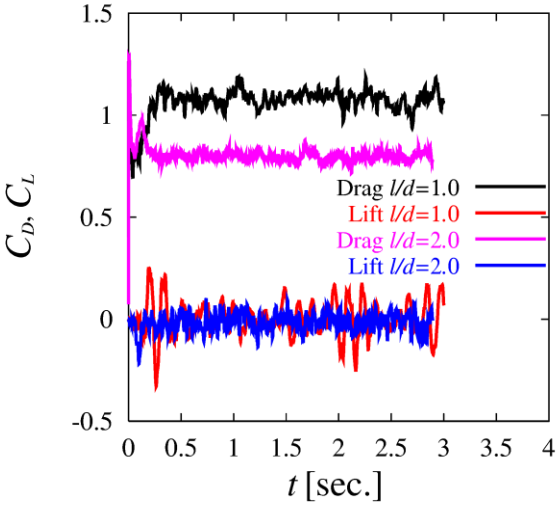

Fig. 3 Time evolution of drag and lift coefficients.

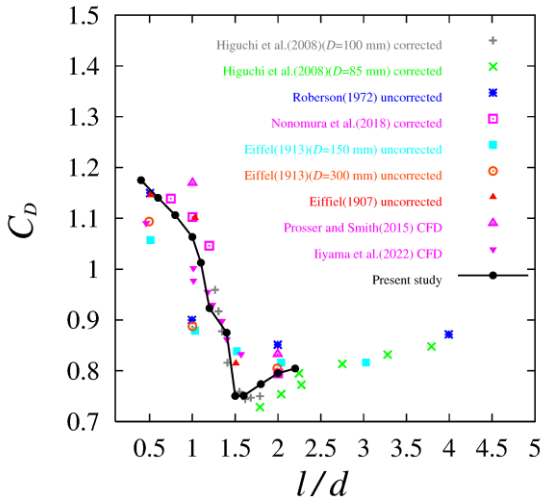

Fig.4 Drag coefficient vs. aspect ratio .

[1] T. Nonomura et. al, Effect of fineness ratios of 0.75–2.0 on aerodynamic drag of freestream-aligned circular cylinders measured using a magnetic suspension and balance system, Experiments in Fluids (2018) 59:77.

Towards greener Vacuum Insulation Panel, X-ray tomography measurements to understand fiber network as pressure decrease.

ELyT Global
ENERGY
Materials & Structure design, Simulation & Modeling

	**Prof. G. Foray**	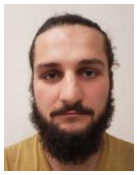	**M. Groux**		**J. Adrien**
	**Prof. F. Martoia**		**Prof P. Dumont**		**Prof A. Komiya**

Abstract

Energy efficiency is one of the significant challenges that need to be addressed for reducing impact on climate and meeting the emission targets as agreed (90% in 2040). Refrigerators accounted for a very large amount of residential electric energy consumption (up to 20%) in some countries and taking a larger view on the cold chain shows that the potentials energy saving equals 665 Mt eq. CO_2 /y worldwide (Gao 2018). For buildings, cold chain chambers, medical transportation systems, vacuum insulation panels (VIP) offer a unique way of reducing the transmission losses of with minimal insulation thicknesses so that it is possible to enhance the useful volume without changing their external dimensions (Verma 2019). VIP's exhibit thermal conductivity down to 1-2 $mW.m^{-1}.K^{-1}$ that are five times lower than that of the best polyurethane foams (20-29 $mW.m^{-1}.K^{-1}$) used for domestic appliances However, as consumer change their appliances every ten years a huge amount of 'aged VIP' are about to enter the recycling or upcycling market. This surges the need for greener core material.

At a first glance VIP's consist of a 400x400*10 mm^3 panel. This panel is sealed within a polymer-metal multilayer envelop under low internal pressure (0.006 to 0.1 mbar). The greater the pore size is, the lower the internal pressure should be to ensure low thermal conductivity. Efficient VIPS' also consist of a highly porous bearing core material that is usually made of an anisotropic network of glass fibers with diameter smaller than 5 microns. The overall thermal conductivity (Foray 2022) of the VIP's depends on residual gas conductivity, fibrous material conductivity, envelope conductivity. Specification to design greener core fiber material are

numerous (i) Geometry: smooth surface of the panel after compression, (ii) limited thickness deformation from atmospheric pressure down to 0.005 mbar (iii) low skeleton conductivity.
The purpose of this study is to measure 3D microstructure evolution while decreasing the pressure inside the envelop. Morphological features such as pore size distribution, fibers thickness distribution, and tortuosity are of interest. A specific protocol was successfully built, so as to allow comparative analysis of some multilayer composite sample while the pressure decrease. Samples are made of flax fibers or recycle textile fibers.

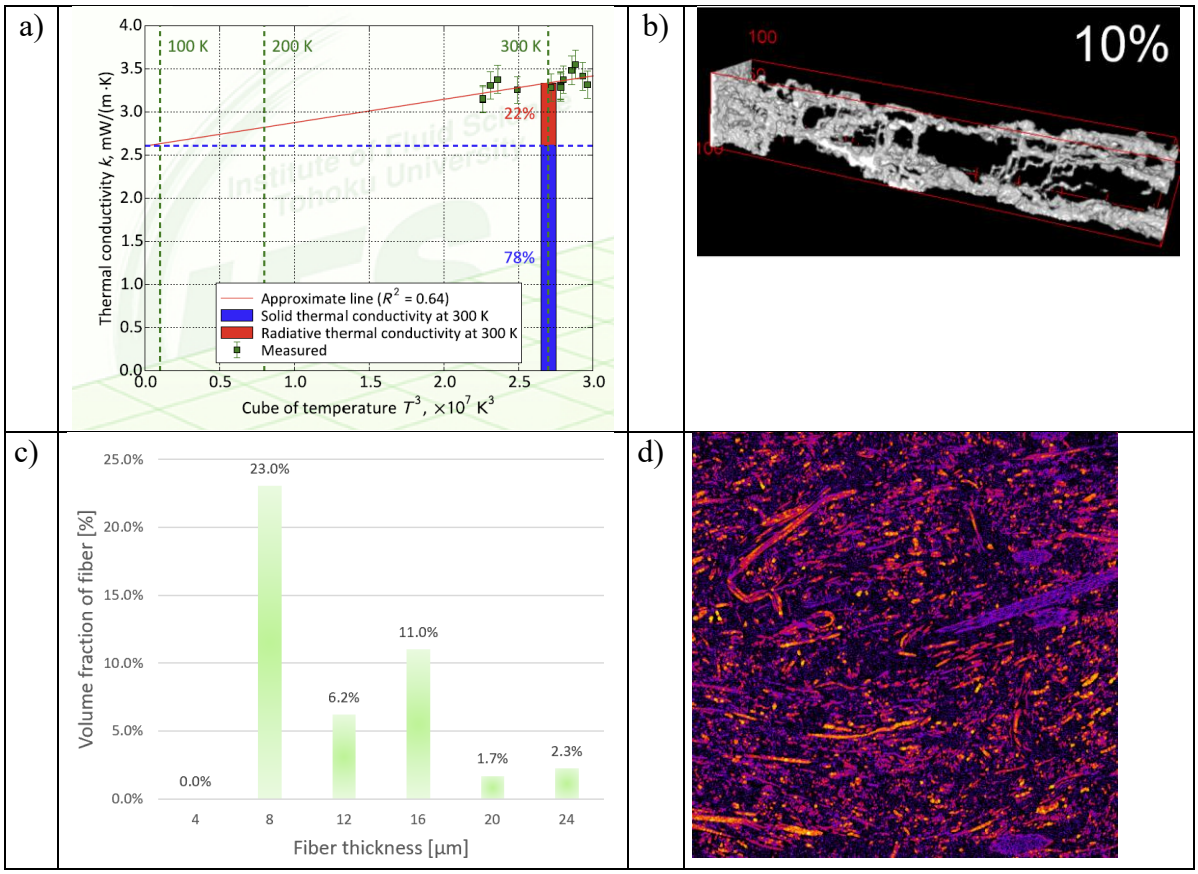

Figure 1 : a) thermal conductivity measured at IFS glass fiber panel b) connected thermal path in a commercial VIP parallel to thermal flux front gradient, c) VIP flax fiber: histogram of thickness d) thickness viewed as 3D volume (white: 24µm purple: 8µm)

Measurements on 3 commercial VIP (fig 1a) proof that thermal conduction is dominant. For our flax VIP Composite at ambient pressure (Fig 1c-d) tomography fiber size is in the range 4 to 20µm. Then, with a resolution of 4 microns, the pores and fibers network are characterised as pressure decrease in VIP. The best flax VIP composite reach a 220 kg.m^{-3} density, a porosity of 82.7%. As the anisotropic fibre board is compressed, its thickness reduced and the tortuosity, as well as the longest and shortest path perpendicular to XY plane increased. Comparative analysis of textile and flax composite shows that flax is more efficient for the VIP design: better geometry achieved, smaller vertical deformation under vacuum, higher network tortuosity.

Gao H., Analysis of New Energy-saving Technology for Cold Chain Logistics, *IOP Conf. Ser.: Earth Environ. Sci*., 2019, 252, 032007
Verma S., et al. Vacuum insulation in cold chain equipment: A review, *Energy Procedia*, 2019, 161, 232.
Foray, G., et al., X-ray Tomography Coupled with Finite Elements, A Fast Method to Design Aerogel Composites and Prove Their Superinsulation Experimentally. *Gels*, 2022, *8*(11), 732.

Advanced Computational Study of Liquid Ammonia Atomization and Spray Combustion Characteristics with Phase Change

ELyT Global

Theme: Energy

Scientific topic: High-Performance Computing

		**Prof. Jun ISHIMOTO** **IFS, Tohoku Univ.**	

Abstract

As global decarbonization efforts accelerate, the deployment of carbon-free or low-carbon fuels has emerged as a key pathway toward deep emission reductions in these hard-to-abate sectors. Among the various candidates currently under consideration, ammonia has attracted increasing attention as both a hydrogen energy carrier and a direct combustion fuel. From a systems perspective, ammonia offers several practical advantages: it is relatively easy to liquefy under moderate pressure, possesses a high volumetric hydrogen storage density, and can leverage existing global production, storage, and transportation infrastructures originally developed for fertilizer applications. In addition, ammonia does not emit CO_2 during combustion, making it an attractive option for reducing greenhouse gas emissions when supplied from low-carbon or renewable pathways. Japan has played a leading role in advancing ammonia energy technologies, particularly through large-scale demonstrations of ammonia co-firing in existing coal-fired power plants. Such co-firing strategies enable significant CO_2 reductions while extending the useful life of existing thermal assets, thereby offering a pragmatic transitional route toward carbon neutrality.

Among the many factors governing ammonia combustion, the spray and atomization characteristics of liquid ammonia (LNH_3) are central [1]. In direct liquid injection systems, spray behavior directly determines fuel–air mixing, local equivalence ratio distributions, ignition delay, and heat-release rates within the combustor. In the case of LNH_3, these processes are strongly influenced not only by aerodynamic breakup mechanisms but also by intense phase-change phenomena associated with ammonia's low boiling point. At atmospheric pressure, ammonia boils at approximately 240 K (−33 °C), meaning that near room temperature, even a modest pressure reduction can drive the liquid into a superheated state. When superheated LNH_3 is injected at high pressure into a lower-pressure environment, the sudden

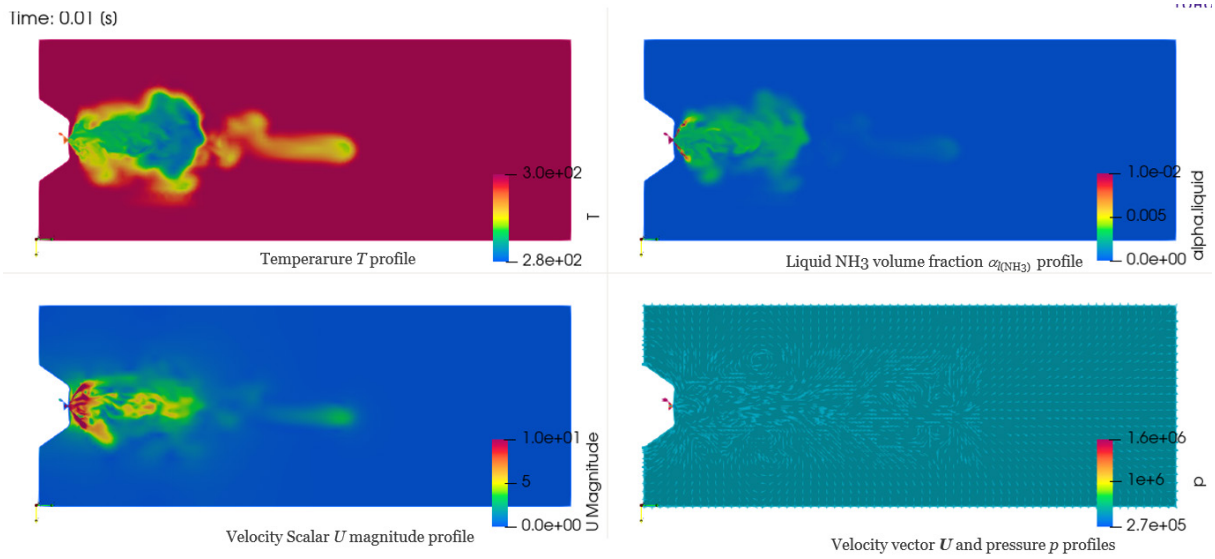

Figure 1 Instantaneous atomization and spray flow characteristics of LNH_3

pressure drop dramatically reduces the local boiling point, leading to rapid, non-equilibrium vaporization. This process triggers the simultaneous nucleation and growth of vapor bubbles within the liquid phase.

This phenomenon, commonly referred to as flash boiling or flash evaporation, results in an abrupt liquid-to-vapor phase change that occurs not only at the liquid–gas interface but also within the liquid core, including regions within the nozzle and immediately downstream of the orifice. Flash boiling can fundamentally alter both macroscopic and microscopic spray characteristics: it tends to increase spray cone angles, shift primary breakup locations closer to the nozzle, thin liquid films in hollow-cone sprays, and significantly reduce droplet sizes, thereby accelerating evaporation. At the same time, the strong evaporative cooling associated with rapid phase change can induce substantial temperature drops in the near-nozzle region. These temperature reductions may adversely affect ignition, flame stabilization, and overall combustion efficiency, while also influencing NO_x formation pathways. Despite its clear relevance to ammonia combustion, most traditional spray research has focused on hydrocarbon fuels under non-flashing conditions, and systematic experimental and numerical studies explicitly addressing flash boiling of liquid ammonia remain scarce.

This study extends the framework to a fully three-dimensional (3D) geometry based on CAD data of an actual hollow-cone nozzle used in experiments. This 3D model enables direct simulation of realistic hollow-cone LNH_3 sprays, including the formation of thin conical liquid sheets, their destabilization and breakup, and the development of a hollow spray core filled with vapor and entrained ambient gas. Numerical consistency between the 2D and 3D cases is maintained through the use of identical discretization strategies and turbulence modeling approaches, while the Hertz–Knudsen model is retained as the phase-change closure. The 3D simulations reveal how flash boiling promotes preferential phase change along the spray periphery, where the liquid film is relatively thin and exposed to strong shear and pressure gradients.

References

[1] Jun Ishimoto, Computational Study of Liquid Ammonia Atomization Characteristics with Phase Change in an Injector Nozzle, *Proceedings of the ILASS-Americas 35th Annual Conference on Liquid Atomization and Spray Systems*, May 18-21, 2025, Bozeman, Momtana, USA

Towards in vivo mechanical characterisation of intracranial aneurysms: a Coherent Point Drift-based approach

ELyT Global
Engineering for Health
Simulation & Modeling

	**Lise Fontalirant**[a]	**Jean-Baptiste Langlois**[b]	**Salim Si-Mohamed**[c,d]		**Jolan Raviol**[a]
	**Guillaume Plet**[a]		**Hélène Magoariec**[a]	**Cyril Pailler-Mattei**[a,e]	

[a] *Laboratoire de Tribologie et Dynamique des Systèmes, UMR CNRS 5513, École Centrale de Lyon, France*
[b] *CERMEP - Imagerie du Vivant, France*
[c] *University of Lyon, INSA Lyon, University Claude Bernard Lyon 1, UJM-Saint Etienne, CNRS, Inserm, CREATIS UMR 5220, U1206, F69621, France*
[d] *Département de Radiologie, Hôpital Louis Pradel, Hospices Civils de Lyon, France*
[e] *University of Lyon, University Claude Bernard Lyon 1, IPSB-Faculty of Pharmacy, France*

Abstract

Introduction

Intracranial aneurysm (IA) is a life-threatening pathology related to arterial wall deterioration. Although these mechanical alterations are a key factor in the rupture mechanism, no reliable method currently exists to predict rupture risk using in vivo biomechanical data. Developing tools to characterise these properties non-invasively is therefore essential for improving clinical risk assessment and guiding treatment decisions. This work, conducted on an animal model of aneurysm, represents a first step towards better understanding of vascular wall rupture risk. It presents the application of a procedure based on the Coherent Point Drift (CPD) algorithm to quantify the strain fields induced by a non-destructive vascular wall deformation device (DDP), enabling the acquisition of mechanical data to build a database for IA analysis.

Methods

A saccular aneurysm was induced on the bifurcation of a rabbit carotid artery to mimic a human IA. The DDP was designed as a catheter repurposed from its original use [1]. The Spectral Photon Counting Computed Tomography prototype system (SPCCT) was used for imaging. Two configurations were considered for the images acquisition: Configuration 1 (C1) with the DDP positioned in the aneurysm without flow, and Configuration 2 (C2) with flow applied by

the DDP (Figure 1). An original procedure was implemented to determine the mechanical properties of the aneurysm using the CPD algorithm, which aligns two point clouds by assuming that one is a probabilistic transformation of the other [2]. Extracting the aneurysm from SPCCT images as point clouds allows a direct comparison of the two configurations and provides mechanical characterisation of the aneurysm.

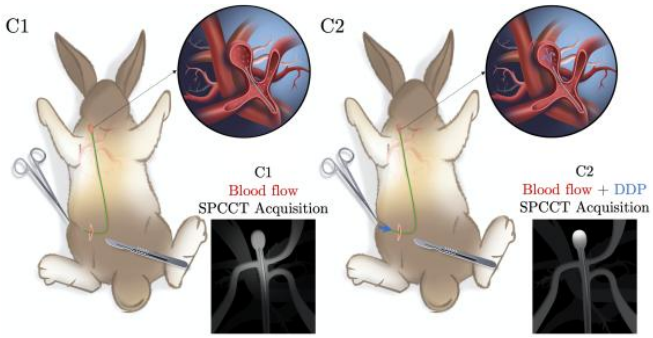

Figure 1. Configurations of the images acquisition

Results

Among the rabbits tested, several aneurysms were successfully created. Using the numerical procedure, it was possible to quantify the strain fields for a known mechanical loading. The average strain of aneurysms ranged from 7% to 40%.

Discussion

By combining the strain fields with material parameters representative of rabbit arteries, it would be possible to determine the corresponding stress fields, thereby pointing toward the definition of a rupture criterion.

References

1. Raviol, J. et al., Royal Society Open Science, 2024
2. Xie, H. et al., Journal of Biomechanics, 2024

Acknowledgements

This work was funded by the French ANR (PRAnevrisme, ANR-23-CE19-0034-01).

Towards Real-Time Whole-Brain Arterial 3D Hemodynamic Prediction — A Physics-Constrained Deep Learning Framework for the Internal Carotid Artery

ELyT Global
Engineering for Health Simulation & Modeling

	**Dr. Jing Liao** Institute of Fluid Science, Tohoku University, Japan.		**Keito Yanagisawa** Institute of Fluid Science, Tohoku University, Japan.		**Zhengbang Zhang** Institute of Fluid Science, Undergraduate School of Engineering, Tohoku University, Japan.
	**Dr. Carole Frindel** CREATIS, INSA Lyon, France.	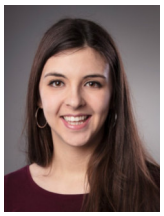	**Dr. Odyssée Merveille** CREATIS, INSA Lyon, France.		
	**Prof. Makoto Ohta** Institute of Fluid Science, Tohoku University, Japan.		**Dr. Hitomi Anzai** Institute of Fluid Science, Tohoku University, Japan.		.

Abstract

1. Introduction

Hemodynamic parameters play a critical role in diagnosis, risk assessment, and treatment planning of cerebrovascular diseases. However, acquiring high-resolution, whole-brain three-dimensional (3D) hemodynamics in real time remains challenging due to the inherent limitations of current medical imaging modalities and the high computational cost of conventional computational fluid dynamics (CFD) simulations. Although recent artificial intelligence (AI)-based methods have shown promise for fast hemodynamic inference, their performance in clinical practice is often constrained by severe data scarcity and ethical barriers to large-scale patient data collection.

2. Method

In this study, we propose a physics-constrained deep learning framework for real-time 3D hemodynamic prediction in the internal carotid artery (ICA), designed to operate effectively under limited patient-specific datasets. The framework integrates a tailored point cloud

preprocessing strategy with a physics-informed neural networks (PINNs) architecture. Specifically, spatial homogeneity of training data is ensured through voxel-based resampling and distance-weighted interpolation, enabling efficient learning from CFD-derived point cloud representations. The PINNs module further embeds the governing fluid dynamics into the learning process, transforming the model from a purely data-driven paradigm into a semi-data-driven framework and reducing dependency on labeled data.

3. Result & Discussion

Four controlled experiments were conducted on a limited dataset of 51 patient-specific CFD cases, with 11 cases reserved for testing, to systematically evaluate the contributions of point cloud preprocessing and physics constraints. The proposed combined approach demonstrates superior performance in predicting spatially anisotropic hemodynamic fields, including three velocity components and pressure. The model achieves strong visual consistency with CFD results while reducing inference time to approximately one second. On the test set, normalized mean absolute errors (NMAEs) of 7.79 ± 2.14% for velocity and 6.63 ± 2.80% for pressure were obtained, comparable to or better than previously reported methods trained on large synthetic datasets.

4. Conclusion

These results highlight the feasibility and robustness of the proposed framework for real-time, arterial hemodynamic modeling, offering a clinically practical solution for patient-specific flow analysis in whole-brain in the future.

Acknowledgements

This work was supported by JSPS Core-to-Core Program (grant num ber: JPJSCCA20210005), AMED（Grant Number JP23tm0524003), JST BOOST Program Japan (Grant Number JPMJBY24H7).

Cellulose Nanofiber-Reinforced Silk Fabrics via Silkworm Feeding: Tensile Properties and Dimensional Stability

ELyT Global

Sustainable Bio-Derived Materials Materials Design

Prof. Hiroki KURITA

Graduate School of Environmental Studies

Tohoku University

Abstract

Silk is a widely used biopolymer primarily produced by silkworms (Bombyx mori), with global production exceeding 120,000 tons annually. Owing to its excellent mechanical strength, flexibility, smooth texture, and biocompatibility, silk has long been utilized in textiles and biomedical applications. Raw silk consists of two fibroin filaments bonded by sericin; removal of sericin (degumming) yields silk fibroin (SF) fibers with improved flexibility and processability. Regenerated SF can be fabricated into various forms, including films, hydrogels, and porous structures, enabling applications in wearable electronics, biosensors, drug delivery systems, and tissue engineering.

In recent years, our group has explored the reinforcement of SF with cellulose nanofibers (CNF) by feeding silkworms artificial diets containing CNF. Wu et al. demonstrated that 5 wt.% CNF enhanced the Young's modulus and tensile strength of sericin-coated SF fibers, with CNF aligned along the fiber axis. Kobayashi et al. confirmed that high tensile properties were retained after degumming and that CNF formed fibrous structures on the SF surface. Furthermore, CNF-reinforced twisted yarns exhibited superior strength, optimal mechanical balance at 1,000 turns per meter, and excellent fatigue resistance. Interestingly, CNF-reinforced fibers remained straight after storage under high humidity, suggesting reduced moisture-induced shrinkage.

Based on these findings, the present study systematically evaluates the tensile properties and dimensional stability of CNF-reinforced SF at three textile processing stages: single filaments, twisted yarns, and woven fabrics. Specimens were immersed in deionized water, and dimensional changes after drying were quantified to assess swelling–drying-induced stability. The mechanical properties and dimensional stability of CNF-reinforced SF were systematically investigated across three hierarchical levels of textile processing: single filaments, twisted yarns,

and woven fabrics. By directly feeding silkworms with an artificial diet containing CNF, a bio-derived reinforcement strategy was realized without altering conventional silk production processes. At the single-filament level, the addition of 5 wt.% CNF resulted in substantial improvements in Young's modulus and ultimate tensile strength, while the fracture elongation remained nearly unchanged. These enhancements were maintained at higher structural levels, leading to improved tensile performance in both twisted yarns and fabrics (see Fig. 1).

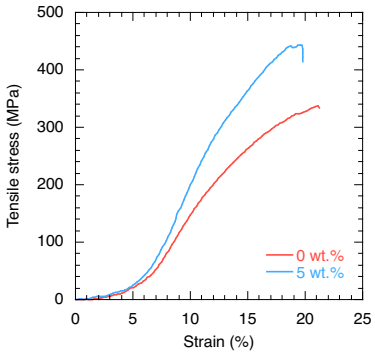

Fig. 1 Representative stress–strain curves of CNF0 and CNF5 silk fabrics.

The dimensional stability of CNF-reinforced silk was quantitatively evaluated through swelling and drying tests. While individual filaments exhibited negligible shrinkage regardless of CNF addition, twisted yarns and fabrics showed pronounced shrinkage due to their hierarchical assembly. Notably, CNF addition significantly suppressed moisture-induced dimensional changes in yarns and fabrics, with the shrinkage rate of CNF5 twisted yarns reduced to less than one-quarter of that of CNF0 yarns. A similar stabilizing effect was observed in woven fabrics. Fourier Transform Infrared Spectroscopy (FT-IR) analysis based on the amide III region revealed that CNF addition did not significantly increase the β-sheet crystallinity of single filaments within the investigated concentration range (see Fig. 2). This finding indicates that the improved dimensional stability does not originate from enhanced crystalline structure formation, contrary to the initial hypothesis. Overall, this study demonstrates that CNF addition via silkworm feeding is an effective and sustainable approach to simultaneously enhancing the mechanical performance of silk filaments and improving the dimensional stability of practical silk forms such as yarns and fabrics. The decoupling of crystalline structure modification from macroscopic dimensional stability provides new insight into the multiscale design of silk-based materials. These findings highlight the potential of CNF-reinforced silk for advanced textile and structural applications requiring both mechanical robustness and resistance to moisture-induced deformation.

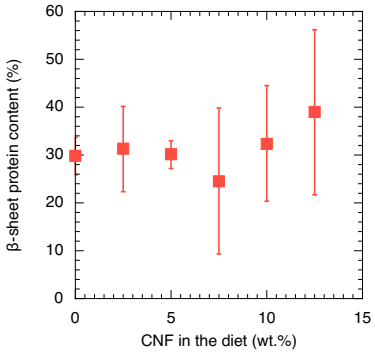

Fig. 2 β-sheet crystallinity of CNF–SF single filaments evaluated by FT-IR spectroscopy using the amide III absorption bands.

Table 1: Tensile properties of CNF0 and CNF5 silk fabrics.

Specimen	Young's modulus (GPa)	Ultimate tensile strength (MPa)	Fracture elongation (%)
CNF0-fabric	3.1±0.2	330±7.1	22.3±1.0
CNF5-fabric	4.4±0.4	425±22.9	18.3±1.3

Table 2: Shrinkage rates of CNF0 and CNF5 single filaments, twisted yarns, and fabrics induced by swelling and subsequent drying.

Specimen	Shrinkage rate (%)	Specimen	Shrinkage rate (%)
CNF0-single filament	0.21±0.22	CNF0-fabric	0.68±0.42
CNF5-single filament	0.19±0.05	CNF5-fabric	0.43±0.10
CNF0-twisted yarn	0.43±0.12		
CNF5-twisted yarn	0.10±0.08		

Mechano-Chemically-activated Tribofilm Growth at Nanoscale on DLC materials (**MeCaT-DLC**)

ELyT Global

Theme: Transportation, Energy

Scientific topic: Surfaces and interfaces & Materials

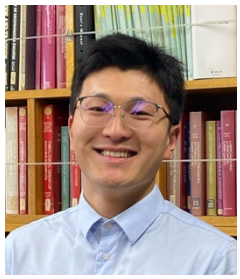	**Dr. Shaoli Jiang** Department of Mechanical Systems Engineering, Tohoku University, Sendai 980-8579, Japan		**Dr. Motoyuki Murashima** Department of Mechanical Systems Engineering, Tohoku University, Sendai 980-8579, Japan
	**Prof. Jean Michel Martin** Ecole Centrale de Lyon CNRS LTDS UMR551 » 69130 Ecully, France		**Dr. Maria-Isabel De Barros** Ecole Centrale de Lyon CNRS LTDS UMR551 » 69130 Ecully, France

Contact: jiang.shaoli.d1@tohoku.ac.jp, maria-isabel.de-barros@ec-lyon.fr

Abstract

Background

In general, the activation of chemical reactions requires energy, which is typically provided by heat, light or electrical potential. When mechanical contact generates a stress field at the interface between two surfaces, certain mechanically induced chemical reactions are initiated or accelerated. In the field of tribology, mechanochemical effects have been used to generate functional layers (known as tribofilms) on the surface of mechanical components, reducing wear and friction. In most tribological research experiments, these reactions are activated simultaneously at the tips of numerous microscopic asperities (surface roughness), where locally distributed tribofilms generate and eventually get mixed into a uniform layer. As a result, tribofilms form rapidly on uncertain areas under unquantified pressures, making it impossible to independently interpret the tribofilm growth kinetics. Here, we are going to explore zinc dialkyldithophosphate (ZDDP) tribofilms formation on varied diamond-like carbon coatings, which promotes a further understanding of mechanochemical effect-resulted phenomenon occurred on non-metallic surfaces.

Key scientific question

Influence of surface physic-chemical properties on ZDDP tribofilm formation.

Developing new analytical strategy to characterize tribofilms.

Research method

As the most successful antiwear additive ever invented, ZDDP is reported to decompose with physicochemical pathways, leading to protective tribofilm. However, there is no information on the evolution of their compositions and concentrations, as well as distribution within tribofilm. In this work, by mimicking sliding nanocontacts using atomic force microscopy (AFM), ZDDP tribofilms formation on varied DLCs (hydrogenated and nitrogen-doped) surface process was observed. The influence of surface morphology and chemical composition was discussed.

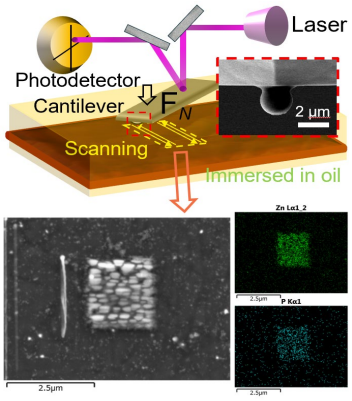

Achieving 30-fold friction anisotropy in liquids using rubber with inclined-groove texture

ELyT Global

Theme: Tribology

Scientific topic: Friction control in liquids

	**Asst. prof. Arata ISHIZAKO** **Tohoku University**		**Assoc. prof. Toshiaki NISHI** **Tohoku University**		**Prof. Takeshi YAMAGUCHI** **Tohoku University**

Abstract

Rubber is used in products requiring high friction, such as shoes, tires, brakes, and robotic hands. However, rubber friction decreases under liquid lubrication. This decrease in friction could lead to serious accidents, such as traffic accidents and slip-induced falling accident, thus maintaining high friction in rubber even in liquids is a critical issue.

The friction of rubber under lubrication is affected by various factors such as rubber's geometry and material properties[1], and sometimes negative fluid pressure (sub-ambient pressure) can be generated primarily due to reverse-wedge action, which decreases the fluid-film thickness and increases the friction force. Ishizako et al. [2] developed a rubber tread with inclined-groove texture intended to generate negative fluid pressure, demonstrating that the texture increased friction force within liquids. This finding suggests that friction under lubrication can be controlled by regulating fluid pressure through texture. By applying an anisotropic texture that generates different fluid pressures depending on the sliding direction, it may be possible to achieve both high- and low-friction using the same texture. Therefore, in this study, we conducted the friction tests on rubber tread with asymmetric inclined-groove textures in a glycerol solution by varying the sliding direction and investigated the effect of texture anisotropy on friction- and fluid pressure-anisotropy.

Fig. 1 shows the friction force of inclined-groove rubber specimen in glycerol solution lubrication. Here, when the specimen was fixed and the glass tank slides, the sliding direction in which the flow channel expands was defined as the expansion direction, and the opposite direction was defined as the contraction direction. As shown in Fig. 1(b), regardless of the normal load and sliding velocity, friction force in the expansion direction was higher than that in the contraction direction. The difference of friction force between the expansion direction and contraction direction increased with increasing normal load up to $W = 49$ N, and it reached

the 30-fold maximum value. Fig. 2 shows the cross-sectional shape of the specimen and fluid pressure distribution of each sliding direction. As shown in Fig. 2(a), in the expansion direction, negative pressure was generated at the contact interface between the rubber specimen and mating surface, while in the contraction direction as shown in Fig. 2(b), positive pressure was generated.

This bidirectional pressure response provides a mechanism for switching between high- and low-friction states using a single, simple surface texture. Our findings reveal a previously unexplored strategy by utilizing hydrodynamic pressure to control frictional behavior in soft materials. This opens new opportunities for designing liquid-mediated traction surfaces, adaptive grippers, biomedical interfaces, and high-performance footwear.

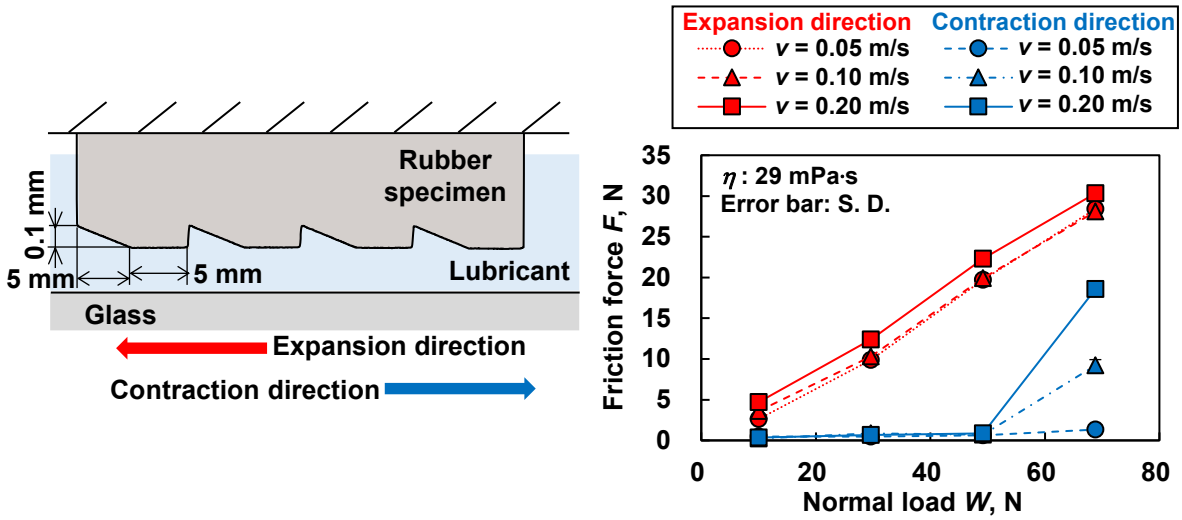

(a) Sliding direction (b) Friction force

Fig. 1 Friction anisotropy of inclined-groove-textured rubber

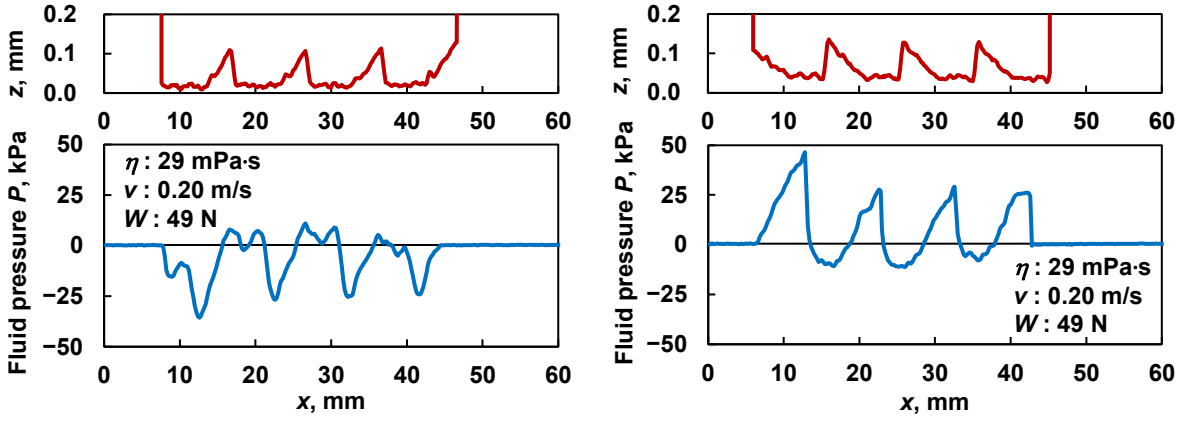

(a) Expansion direction (b) Contraction direction

Fig. 2 Cross-sectional shape of the specimen and fluid pressure distribution (v = 0.20 m/s, W = 49 N)

[1] Ishizako A, Nishi T, Yamaguchi T. Enhancing friction in rubber tread under lubrication: A review. Friction 2025. https://doi.org/10.26599/FRICT.2025.9441202.

[2] Ishizako A, Nishi T, Yamaguchi T. Increasing friction of tread rubber under lubrication by adjusting groove shape to control fluid flow. Tribol Int 2025;205:110531. https://doi.org/10.1016/j.triboint.2025.110531.

Anodization of aluminum for self-formation of low friction interfaces under severe tribological conditions: AnodiTribo project

ELyT Global
Transportation
Surfaces & Interfaces

	**Mr. Theo Yamana** **Tohoku University, Ecole Centrale de Lyon**		**Dr. Vincent Fridrici** **Ecole Centrale de Lyon**
	**Pr. Motoyuki Murashima** **Tohoku University**		**Pr. Clotilde Minfray** **Ecole Centrale de Lyon**
	**Pr. Koshi Adachi** **Tohoku University**		

Abstract

1. Introduction

Among the many properties required for sliding mechanical components, conformability requires materials with a certain softness. In this context, relatively ductile aluminum alloys are used in journal plain bearings in internal combustion engines. On the other hand, the increasing use of low-viscosity lubricants allowing reduction of hydrodynamic viscous losses implies more frequent occurrence of boundary lubrication, where high friction and wear can occur. This research aims to achieve low-friction and low-wear in a friction system using aluminum alloys in engine oil under boundary lubrication, by controlling the continuous formation of low-friction interface by engine oil additives via anodization. Anodization is a surface treatment that forms a thick oxide layer on the aluminum surface having a nano-scale porous structure that affects its mechanical properties at larger scales. In

this study, to better understand how the anodic oxide layer of aluminum affects its friction behavior in engine oil, specimens of anodized aluminum having different structures were prepared. Friction tests were carried out to study their friction and wear behaviors.

2. Experimental method

Pure aluminum (A1050) disks were anodized in oxalic acid. The porosities of the anodic oxide layers were estimated from SEM images of the anodized surfaces (see Fig.1). Friction tests were performed using a rotating ball-on-disk tribometer immersed in engine oil containing additives such as ZDDP and MoDTC. Bearing steel (JIS-SUJ2) ball was used as counter material. The engine oil was maintained at 80°C.

3. Experimental results

3.1 Friction reduction induced by anodization

Fig.2 shows the friction behaviors of untreated and anodized aluminum for P = 39%, 22% and 8%. In all cases, anodized aluminum showed lower and more stable friction than untreated one after a running-in period. The running-in behaviors of anodized aluminum were classified into the following three modes:

- Mode I where a high friction period (μ=0.15) occurs, followed by a sudden decrease of friction that stabilizes around μ=0.05 (Fig.2 (a)).
- Mode II where a high friction period is followed by a progressive and limited friction decrease (Fig.2 (b)).
- Mode III where friction immediately decreases and stabilizes around μ=0.05 (Fig.2 (c)).

3.2 Effect of anodic oxide layer porosity on friction and wear behaviors

Fig.3 shows the effect of porosity on the average friction coefficient and on the wear volume after 10000 friction cycles. When P < 27%, wear volume is negligible and Modes II and III occur with an average friction coefficient increasing with porosity. When P > 27%, Mode I occurs with a significant wear volume.

Cross-section samples of disk wear tracks were cut and profiles of oxide surface together with oxide / substrate interface were obtained from optical microscopy. They are shown for P < 27% (Fig. 4 (a_1)) and P > 27% (Fig. 4 (b_1)). The red line shows the oxide thickness at each point computed from the two profiles. For P < 27%, concavity is formed by substrate plastic deformation, leaving the nanoporous structure intact as shown in SEM image (Fig.4 (a_2)). On the other hand, when P > 27%, the concavity is formed mainly by the volume loss of the oxide layer whose porous structure is severely deformed.

Conclusions

- Low and stable friction can be achieved under boundary lubrication in engine oil with additives by anodizing aluminum.
- Wear can be significantly reduced by using anodic oxide layers having porosities P < 27%.
- When P < 27 %, friction can further be reduced by using anodic oxide layers with lower porosities.

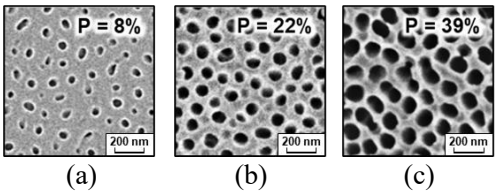

Fig.1 Nanoporous structure of anodic oxide layers with porosity (a) 5%, (b) 22% and (c) 39%

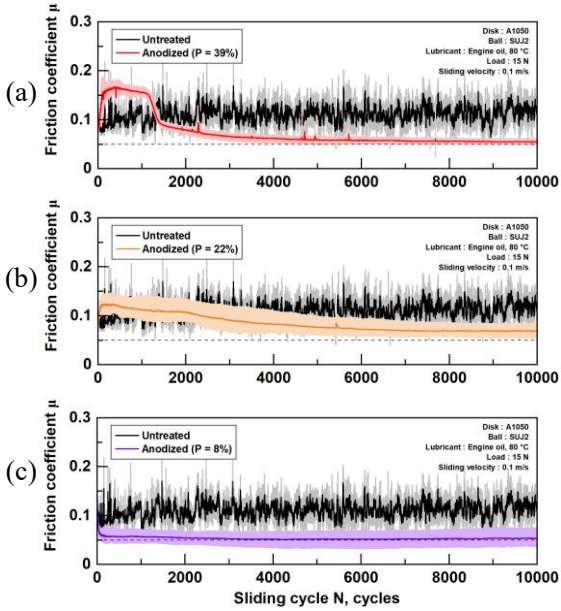

Fig.2 Friction behavior of anodized A1050 with porosity of (a) 39% (Mode I), (b) 22% (Mode II) and (c) 8% (Mode III)

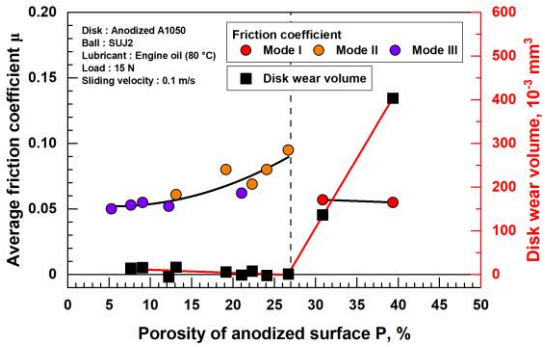

Fig.3 Effect of anodic oxide layer porosity on friction and on wear volume of anodized aluminum

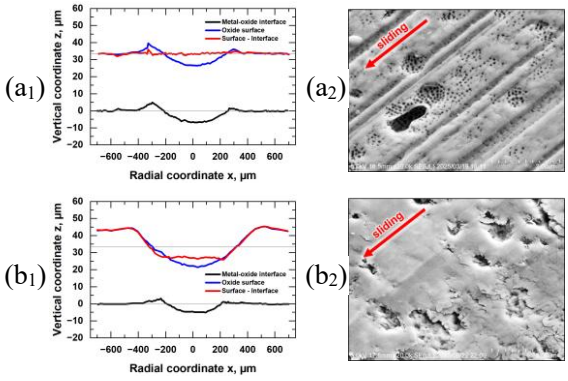

Fig.4 Cross-section profiles of oxide surface and oxide/metal interface and SEM images of oxide surface after friction for (a_1,a_2) P = 22% and (b_1,b_2) P = 39%

In-situ Synchrotron Quantification of Internal Strain Distribution in Rubber During Dry Sliding Against a Resin Sphere

ELyT Global

Theme: Tribology

Scientific topic: Friction of Rubber

Assoc. prof. Toshiaki NISHI

Tohoku University

Abstract

Rubber is widely used in tribological components such as automotive tires and shoe soles, where stable frictional performance is required under diverse environments and operating conditions. Rubber friction is often interpreted as the sum of an adhesion term, associated with interfacial shear over the real area of contact, and a hysteresis term, originating from viscoelastic energy dissipation during cyclic deformation beneath a moving contact. The relative contributions of these terms can change substantially with counter-surface texture, sliding conditions, and lubrication state. Because rubber is soft and viscoelastic, large internal deformation and strong rate dependence are intrinsic to friction generation; however, experimental quantification of the three-dimensional (3D) internal strain distribution during sliding remains limited. Existing approaches are frequently constrained by optical transparency, restricted measurement dimensionality, or practical difficulties in obtaining volumetric data during dynamic friction. Establishing an experimental method capable of measuring 3D internal strain fields in non-transparent rubber during friction is therefore crucial for advancing physically grounded friction control and for connecting deformation asymmetry to the hysteresis contribution. In this study, I develop and validate a synchrotron-based experimental framework to quantify the 3D internal strain distribution in a rubber block while sliding against a resin sphere without lubricant. Instead of in-situ X-ray computed tomography during sliding—impractical at typical sliding speeds—the method acquires high-frame-rate X-ray transmission images from two mutually perpendicular directions in separate but repeatable experiments (Fig. 1). Digital Image Correlation Method (DICM) is applied to time-resolved marker patterns to track internal motion. The two orthogonal measurements are then combined to reconstruct 3D displacement and strain fields in the marker plane. The method is first validated using a reference specimen and subsequently applied to friction tests on a non-transparent rubber specimen containing a metal-marker layer. By tracking hundreds of subsets

within the marker layer, spatially and temporally resolved 3D displacements (Fig. 2) and strain components are obtained, enabling direct visualization and quantitative discussion of deformation asymmetry between the leading and trailing sides of the sliding contact.

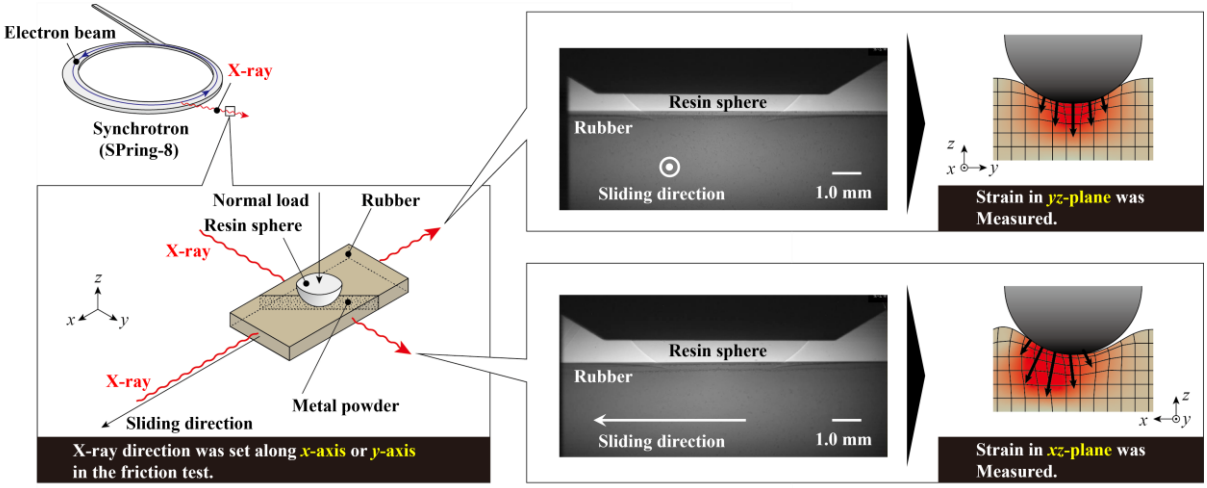

Fig. 1 Schematic view of friction test setup

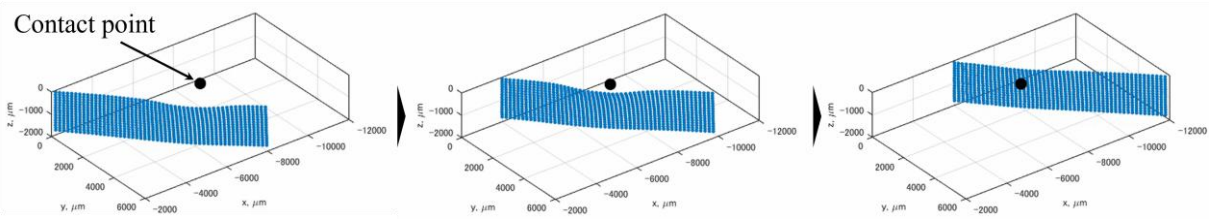

Fig. 2 3D displacement of the marker layer during sliding

Visco-elastic contact : rolling versus sliding, and the effect of multi-layered material and roughness on the apparent friction coefficient

ELyT Global

Tribology & Surface Engineering

Prof. Daniel Nélias

INSA Lyon, CNRS, LaMCoS, UMR5259,
69621 Villeurbanne, France

Abstract

First we will investigate the frictionless rolling contact problem between a rigid sphere and a viscoelastic half-space. The problem is equivalent to the frictionless sliding of a spherical tip over a viscoelastic body. The model presented here is three dimensional and based on semi-analytical methods. In order to take into account the viscoelastic aspect of the problem, contact equations are discretized in the spatial and temporal dimensions. The frictionless rolling of the sphere, assumed rigid here for the sake of simplicity, is taken into account by translating the subsurface viscoelastic fields related to the contact problem. A Conjugate Gradient Method and the Fast Fourier Transforms are used to reduce the computation cost. The model is validated by a finite element model of a rigid sphere rolling upon a homogeneous viscoelastic half-space, as well as through comparison with reference solutions from the literature. Transient and steady-state solutions are obtained. Numerical results about the contact pressure distribution, the deformed surface geometry, the apparent friction coefficient as well as subsurface stresses are presented, with or without heterogeneous inclusion.

In a second part we present a numerical approach to investigate the hysteretic friction phenomenon occurring in sliding contact of viscoelastic materials on rough surfaces. This formulation is implemented in both transient and steady-state regime assuming periodic contact: the rough surface is reduced to a representative unit-cell, which reduces computational effort as the contact is computed within a window of fixed dimensions. This

work first investigates on the parameters that drive the apparent friction and confirms that the frequency ratio and the amplitude-to-wavelength ratio are of primary influence. This is particularly stressed when considering multi-scale surfaces with different levels of roughness. The transient formulation is then employed to investigate the evolution of the friction coefficient over time. We show that depending on contact conditions, friction can exhibit unusual non-monotonic behaviour, at times exceeding the steady-state asymptotic value.

Some results with a multi-layered visco-elastic body will be also presented.

References

[1] Koumi, Koffi Espoir, Nelias, Daniel, Chaise, Thibaut, Duval, Arnaud (2014) 'Modeling of the contact between a rigid indenter and a heterogeneous viscoelastic material', *Mechanics of Materials* **77**, 28-42 https://doi.org/10.1016/j.mechmat.2014.07.001

[2] Koumi, Koffi Espoir, Chaise, Thibaut, Nelias, Daniel (2015) 'Rolling contact of a rigid sphere/sliding of a spherical indenter upon a viscoelastic half-space containing an ellipsoidal inhomogeneity', *Journal of the Mechanics and Physics of Solids* **80**, 1-25 https://doi.org/10.1016/j.jmps.2015.04.001

[3] Wallace, Efoe Rodrigue, Chaise, Thibaut, Nelias, Daniel (2020) 'Three-dimensional rolling/sliding contact on a viscoelastic layered half-space', *Journal of the Mechanics and Physics of Solids* **143**, ARTN 104067 https://doi.org/10.1016/j.jmps.2020.104067

[4] ER Wallace, T Chaise, D Nelias (2022) 'Rolling contact on a viscoelastic multi-layered half-space', *International Journal of Solids and Structures* **239**, 111388 https://doi.org/10.1016/j.ijsolstr.2021.111388

[5] Durand, Nicolas, Platzer, Auriane, Duval, Arnaud, Nelias, Daniel, Chaise, Thibaut (2025) 'Coupled effect of viscoelasticity and roughness scales on hysteretic friction in sliding periodic contact', *Journal of the Mechanics and Physics of Solids* **205**, ARTN 106261 https://doi.org/10.1016/j.jmps.2025.106261

Investigation of bulk and interface mechanical properties; correlations for hard on soft contacts

ELyT Global

Theme: Transportation

Scientific topic: Surfaces & Interfaces

 Sylvain DANCETTE[1]	 Antoine NORMANT[2]	 Jérôme ADRIEN[1]	 Davy DALMAS[3]
 Eric MAIRE[1]	 Masashi MIZUKAMI[2]	 Kazue KURIHARA[2]	

1 - Univ. Lyon, INSA Lyon, CNRS UMR5510, Laboratoire MATEIS, Villeurbanne, France
2 - New Industry Creation Hatchery Center, Tohoku University, Sendai, Miyagi, Japan
3 - CNRS, Ecole Centrale de Lyon, ENTPE, LTDS, UMR5513, Ecully, France

Abstract

This research focuses on soft contact mechanics, more specifically on the deformation of soft solids indented by comparatively much stiffer counterparts. Those systems can be found in real-life applications such as rubber-road grip or medical implants durability. For contacts founds in such systems, the elasticity of the deformable surface is expected to influence many tribological aspects: friction, stick-slip transition, interaction with a lubricant *etc*…

The aim of this study is to demonstrate whether the interface elasticity can be modulated or not in a hard-on-soft contact by precise control of the deformable material's properties. We will use the combination of Resonance Shear Measurement (RSM) in Japan and X-ray Computed Tomography (XRCT) in France to investigate samples of tailored bulk stiffness.

In previous works, Kurihara Group (Japan) has demonstrated that contact stiffness can be quantitatively measured using Resonance Shear Measurement (RSM) experiments, specifically designed for such contact system. This innovative method allows for the determination of the interface elasticity, which has been shown to differ from the bulk elasticity constants, highlighting the unique characteristics of the material at the interface level.

Additionally, the work carried out at MatéIS/LTDS laboratories (France) has introduced an approach for imaging deformations in the local sub-surface area. By using *in situ* X-ray Computed Tomography (XRCT) combined with Digital Volume Correlation (DVC), the setup enables 3D plotting of deformation and stress fields under loaded sliding contacts.

The combined RSM–XRCT approach is expected to open new perspectives on the control of interfacial mechanics in soft contacts.

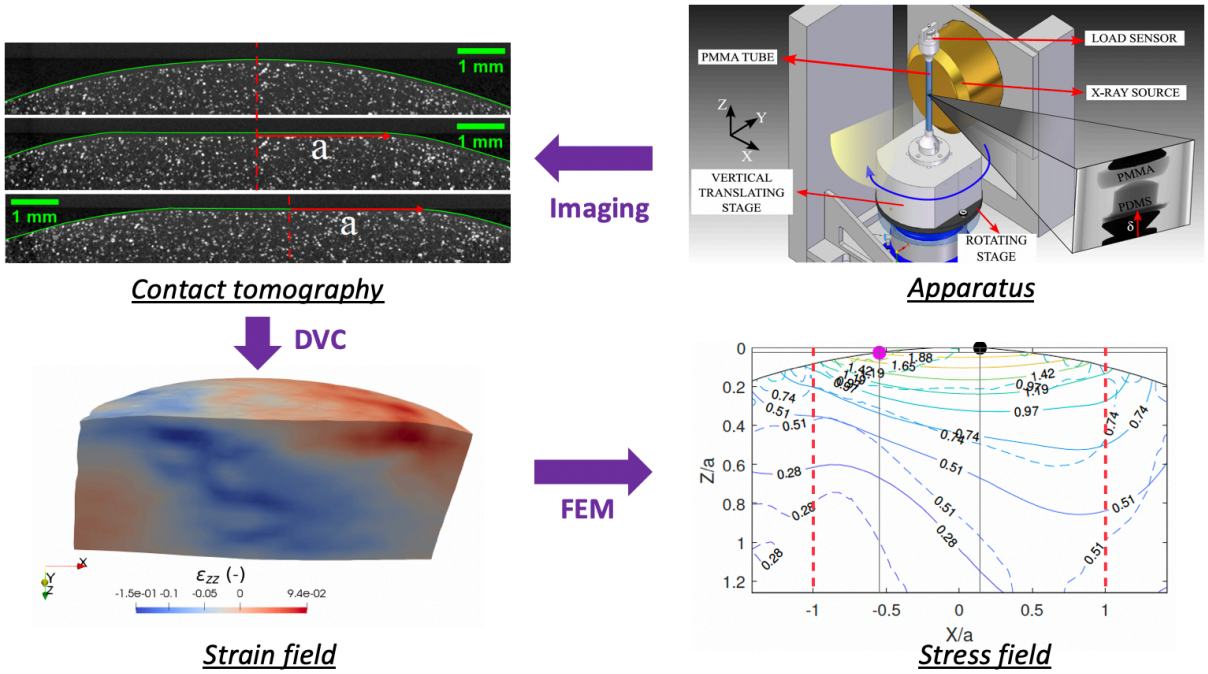

Figure 1 : XRCT/DVC method - apparatus and methodology

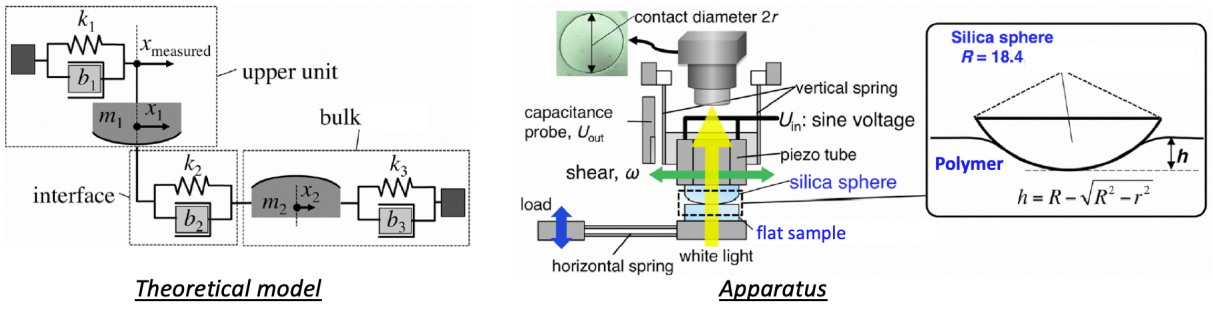

k_2 : stiffness *(resistance to deformation)*
b_2 : viscosity *(energy dissipation)*

Friction force → *Elastic component*
Friction force → *Viscous component*

Figure 2 : RSM model for dry interface analysis and apparatus

Saturday, March 7th

Poser Session

SOLYDIC project: Effect of hydrogen pre-charging on the tribological behavior of lubricated 100Cr6/100Cr6 contacts

ELyT Global

Theme (Transportation, Energy)
Scientific topic (Surfaces and interfaces, Materials & Structure design)

		
Gaël ZAVALETA[a]	**Ana C. PONTES RODRIGUES[a]**	**Nicolas MARY[b]**
		
Tetsuya UCHIMOTO[c]	**Fabrice VILLE[d]**	**Clotilde MINFRAY[a]**

[a] *Ecole Centrale de Lyon, Laboratory of Tribology and System Dynamics CNRS, UMR5513, Ecully, France*

[b] *ELyTMaX IRL3757, CNRS, Univ Lyon, INSA Lyon, Centrale Lyon, Tohoku University, Sendai, Japan*

[c] *University of Tohoku, Institute of Fluid Science, Sendai, Japan*

[d] *INSA Lyon, CNRS, LaMCoS, UMR5259, 69621 Villeurbanne, France*

Abstract

Rolling element bearings are particularly vulnerable to hydrogen embrittlement, a phenomenon that significantly degrades the mechanical properties of metallic materials [1]. This is notably the case for 100Cr6 bearing steel, in which hydrogen has been shown to drastically reduce rolling contact fatigue life [2]. Hydrogen is also known to facilitate the formation of white etching cracks, ultimately leading to premature failure through sub-surface-initiated macro pitting [3]. However, while most studies to date have focused on sub-surface fatigue mechanisms, the consequences of hydrogen on wear and surface damage are less explored. Furthermore, the role of lubricant additives in modulating such damage is largely unexplored. The present study addresses these gaps by examining the effect of hydrogen charging on

surface-initiated damage in lubricated contacts.

To introduce hydrogen into the samples, an electrochemical hydrogen charging procedure was designed, allowing for fast, reproducible, and controlled hydrogen concentration charging.

Tribological tests are conducted on multiple tribometers to capture the full influence of hydrogen on the tribological behavior of 100Cr6 bearing steel. Tests on a High Frequency Reciprocating Rig (HFRR) solicit the material in pure sliding conditions to assess the effect on friction coefficient and wear. Then, tests on a Mini Traction Machine (MTM) in rolling/sliding configuration aim to understand the effect of hydrogen on the initiation of surface damage, and Twin Disc Machine tests are carried out to investigate the effect of hydrogen on the propagation of surface damage.

To support the interpretation of tribological results, mechanical characterizations and non-destructive testing will be employed. Mechanical characterizations consist of tensile testing (slow strain rate testing), fatigue testing (compact tension samples), and hardness measurements (micro/nano). Non-destructive testing is used for the detection and observation of cracks and serves to correlate mechanical and tribological results.

Hydrogen pre-charging of HFRR and MTM samples (Figure 1) was achieved using a three-electrode setup in a solution of 1M NaOH + 8 g/L thiourea (SCN_2H_4). Using the method of Ozdirik [5], cyclic voltammograms allowed visualization of hydrogen desorption, confirming that hydrogen was successfully introduced into the samples.

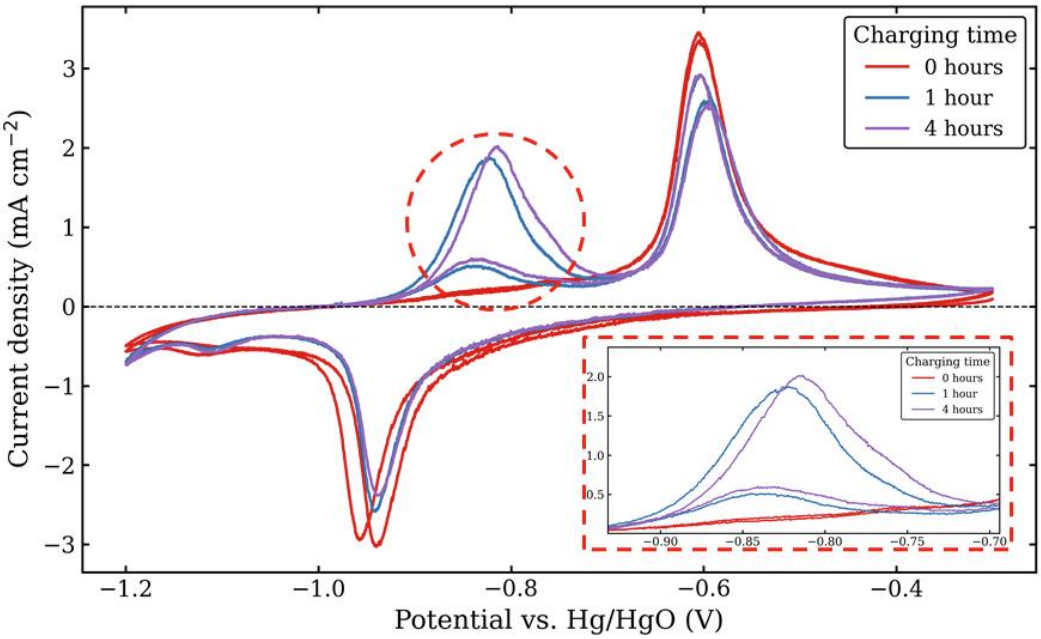

Fig. 1 Cyclic Voltammograms before and after hydrogen charging.

To further verify this, hardness measurements were conducted on charged and non-charged samples using both micro and nano indentations. The observed effects differed depending on the technique and indentation depth, as micro-indentation probes deeper regions than nano-indentation. These behavioral differences could also be attributed to hydrogen diffusion into the specimens, as the degradation mechanisms (HEDE or HELP) are linked to hydrogen concentration in the indented regions, which varies with charging time.

The following steps include a campaign of tribological testing on pre-charged samples, followed by mechanical and non-destructive testing. Thermal Desorption Spectroscopy measurements are also anticipated to quantify the hydrogen concentration within specimens.

References

[1] Y.-S. Chen *et al.*, « Hydrogen trapping and embrittlement in metals – A review », *International Journal of Hydrogen Energy*, vol. 136, p. 789-821, juin 2025, doi: 10.1016/j.ijhydene.2024.04.076.

[2] J. A. Ciruna et H. J. Szieleit, « The effect of hydrogen on the rolling contact fatigue life of AISI 52100 and 440C steel balls », *Wear*, vol. 24, nº 1, Art. nº 1, avr. 1973, doi: 10.1016/0043-1648(73)90207-X.

[3] A. R. D. Créhu, « Tribological analysis of White Etching Crack (WEC) failures in rolling element bearings », phdthesis, INSA de Lyon, 2014. Consulté le: 10 mars 2025. [En ligne]. Disponible sur: https://theses.hal.science/tel-01153235

[4] B. Ozdirik *et al.*, « Development of an Electrochemical Procedure for Monitoring Hydrogen Sorption/Desorption in Steel », *J. Electrochem. Soc.*, vol. 164, nº 13, Art. nº 13, sept. 2017, doi: 10.1149/2.0521713jes.

HLEBI Induced Fracture Toughness of 3D-Printed Short CFR-PLA

ELyT Global

*Effects of HLEBI to Polymers & its Composites

*EBI Induced Adhesive Force of CF/Polymers

Hirotaka IRIE[1], Helmut Takahiro UCHIDA[1], Kouhei SAGAWA[1], Hideki KIMURA[1],

[1]Tokai University, 259-1292, 4-1-1, Kitakaname, Hiratsuka, Kanagawa, JPN. [2]KISTEC, JPN., [3]Tokyo City Univ. JPN,

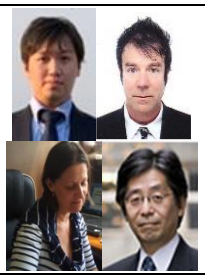

Eiichi MIURA[1,2], Michael C. Faudree[1,3,4], Michelle Salvia[5], Yoshitake NISHI[1,2,5]

[4]Case Western Reserve Univ., USA
[5]Ecole Centrale de Lyon, Ecully Cedex 69134, France.

Abstract

It is a serious problem that 3D-printed short carbon fiber reinforced polylactic acid (3D-SCFRPLA) articles are brittle for practical usages. As a countermeasure, homogeneous low potential electron beam irradiation (HLEBI) was performed to both side surfaces of 3D-SCFRPLA samples. The small dose below 38 +/-5 kGy apparently increased fracture toughness, although additional HLEBI dosage above 86+/-43 kGy decayed tensile strength at endpoint of hardening (σ_{ts}) and fracture strain at start point of heterogeneous deformation (ε_f) as usual radiation damage. Slight HLEBI dose below 27.5 +/-5.5 kGy apparently increased the ε_f values, more than two times higher than those untreated. Improvement in ductility can be explained by polarization, dangling bond generation, and shortening with relaxation of the polymeric chains by the HLEBI.

1. Introduction

Lately, 3D printing has been known as additive manufacturing (AM) of materials for a more sustainable environment and circular economy [1]. It is the construction of 3D objects that can have complex shapes, from a computer-aided design (CAD), or other digital 3D model eliminating scrap generation. The process involves the deposition, joining, or solidification of materials under computer control, typically in a layer-by-layer manner. Although the fracture toughness of polymers is mainly caused by polymer-entanglement with molecular forces [1], 3D-printing articles often exhibit brittleness with weak fracture toughness due to the presence of incoherent interface between solidified and liquid layers in solidification texture. To date, little or no research has been conducted on improvement of mechanical properties of 3D-SCFRPLA through HLEBI. Research has included: adhesion behavior between CF and PLA [2], comparative mechanical performance, shear test property evaluation, flow, diffusion behavior, and the effect of manufacturing-induced interfaces on the tensile properties of 3D-SCFRPLA. For this reason, we employ the novel method for 3D-SCFRPLA using HLEBI treatment to relax polymers by polarization and to expand the texture, resulting in recovering the interface, as well as to form the dangling bonds on poymers and carbon fiber, resulting in strengthening the 3D-SCFRPLA [3,4,5]. The development of 3D-SCFRPLA composites with enhanced fracture toughness for 3D printing would enable a wide range of applications in : aerospace, automotive, sports equipment, electronics, and medical use. HLEBI generally cleaves atomic bonds at the weak chemical bond sites of PLA ($[–C(CH_3)HC(=O)O–]_n$), resulting in dangling bonds at low dissociation energy terminal atom lone pairs [3,4,5,6]. Based on CF single-fiber tensile tests, HLEBI is expected to enhance both tensile strength and its strain. The purpose of the present work is to improve the fracture toughness of 3D-SCFRPLA treated by HLEBI. Therefore, we apply this novel HLEBI treatment to 3D-SCFRPLA, aiming to improve ductility for 3D printing applications.

2. Experimental Procedure

2.1. Preparation of 3D-SCFRPLA & Characterization: The composite samples were shaped by both 3D-printer (Kobra Neo, Anycubic Ltd. Tokyo, Japan) and its filament of short carbon fiber reinforced polylactic acid (3D-SCFRPLA: Polymaker® PolyLite PLA-CF filament, Ltd., Changshu, China) ejected at 503K, less than 70 deg. higher than the melting point. Infill was not used. The 3D-SCFRPLA dog bone samples had 20 mm of gauge length, 4mm thickness, 10mm of width and 100 mm of total length. Volume fraction (V_f) of CF was approximately 10%. Mechanical properties were evaluated by tensile test (JIS K7161). Intron type tensile tester (Instron 5900R

5582 ; Instron Japan, Kawasaki, Japan). The strain rate (load speed) was 1 mm/min.To evaluate static fracture toughness, initial elasticity, as well as tensile strength and its strain for 3D-SGFRPLA samples with and without HLEBI were measured. The strain rate (load speed) was 5 mm/min. The morphology was observed by SEM. To obtain more precise information on atomic-scale structural changes in the 3D-SCFRPLA, chemical bonding state and the dangling bond density were obtained using XPS analysis .

2.2. Homogeneous low voltage electron beam irradiation (HLEBI) : Samples were homogeneously irradiated using an electron-curtain processor (Type LB250/15/180L), Energy Science, Inc., Woburn, MA, Iwasaki Electric Group, Ltd., Tokyo) [3-6] with the electron beam through a titanium thin film window attached to a vacuum chamber, ~240 mm in diameter. A tungsten filament in the vacuum was used to generate the electron beam at an acceleration potential of 210 kV and irradiating current of 2.68 mA. To prevent oxidation, the samples were kept in a 1 atm N_2 atmosphere with a residual O_2 concentration below 300 ppm. The N_2 gas molar flow rate was 89 L/min. The distance between sample and Ti window was 30 mm. Samples were transported in a 200 x 150 mm aluminum plate holder on a conveyor at a speed of 10 m/min. One sweep going one way was 42.3 kGy for the short time of 0.20 s to avoid excess heating of the sample. Repetitive applications to both side surfaces were applied to achieve the desired dose of HLEBI, with a gap interval of 20 s between each sweep. The resulting EB dosage ($Dose = 0.216(I/S)N$) was proportional to the yield value determined from the irradiation current, I (mA) conveyor speed, S (mmin^{-1}), and number of irradiations, N. The yield value was calibrated by FWT nylon dosimeters (Far West Technology, Inc. 330-D South Goleta, CA 93117). Although the anode potential could be controlled from 100 to 250 kV for the equipment, the 210 kV-HLEBI with 129 and 215 kGy to both side surface of the 3D-SCFRPLA samples was performed in the present work.

3.Experimental Results & Discussion : Although the slight HLEBI dose below 27.5 +/-5.5 kGy to both sides of 3D-SCFRPLA samples apparently increased the ε_f (fracture strain, that is assumed to be the start point of heterogeneous deformation), more than two times longer than that untreated, the small HLEBI dose of 38 +/-5 kGy to both sides of 3D-SCFRPLA samples apparently increased the σ_{ts} (tensile strength, that is the endpoint of hardening), whereas decreased the ε_f. Both σ_{ts} and ε_f were 1.09 & 1.7 times higher than those untreated, respectively. Higher dosage of more than 86+/-43 kGy decay the σ_{ts} and ε_f, as usual radiation damage. On the other hand, the ε_{ts} (the strain at tensile strength corresponding to homogeneous deformation) was not largely changed by HLEBI. Improvement in ductility can be explained by polarization, dangling bond generation, shortening and relaxation of the polymeric chains by the HLEBI.

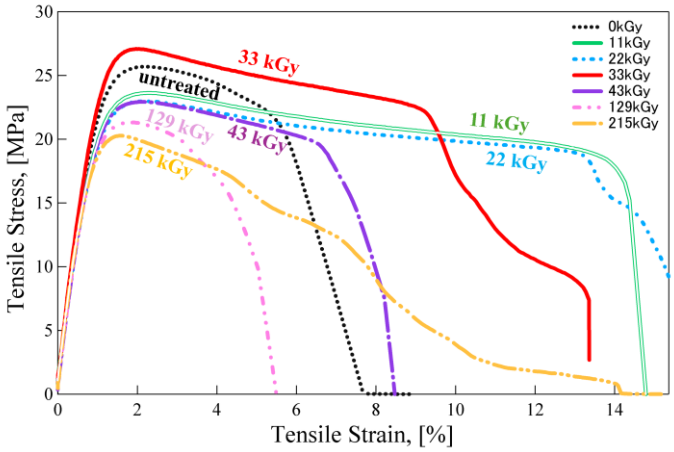

Fig. 1. Changes in tensile stress-strain curves of 3D-SCFRPLA at each irradiation dose of electron

4.Conclusion: To improve the brittleness, HLEBI was performed to both sides of 3D-SCFRPLA samples.
①Although higher HLEBI dosage of more than 86+/-43 kGy decay the σ_{ts} (tensile strength) & ε_f (fracture nominal strain, defined by the start point of heterogeneous deformation), as usual radiation damage, the dose below 38 +/-5 kGy to both sides of 3D-SCFRPLA samples increased the ductility.
②The slight HLEBI dose of less than 27.5 +/-5.5 kGy to both sides of 3D-SCFRPLA samples apparently increased the ε_f values, more than two times higher than those untreated.
③Improvement in ductility can be explained by polarization, dangling bond generation, shortening and relaxation of the polymeric chains by the HLEBI.

References

[1] H.C. Kim *et al.*, "Room temperature 3D printing ---structures", *Compos Part B-Eng*, **279** (2024)1-9.
[2] Zhaobing Liu, et.al., Mechanical-PLA composites-FDM, *J. Mater. Research Technol.*, **8** (2019) 3741.
[3] Y. Nishi, H. Takei K. Iwata, M. Salvia, A. Vautrin, *Maters. Trans.*, **50** (2009) 2826.
[4] H. Takei, K. Iwata, M. Salvia, A. Vautrin, Y. Nishi, *Mater. Trans.*, **51** (2010) 2259.
[5] E. Miura, H. T. Uchida, T. Okazaki, K. Sagawa, M.C.Faudree, M.Salvia, H. Kimura, Y.Nishi, *Polymers*, **16** (2024) 3408.
[6] Y. Nishi, N. Tsuyuki, M. C. Faudree, H. T. Uchida, K. Sagawa, Y. Matsumura, M. Salvia, H. Kimura, *Polymers*, **17** (2025) 1034.

Probabilistic Evaluation Method for Cracks on Divertor Armors in Fusion Reactors Using Direct Current Potential Drop Technique

ELyT Global

Theme: Energy

Scientific topics: Materials & Structure design

	**Mr. Kazushi HONJO** **Graduate School of Engineering, Tohoku University, Sendai, Japan**		**Prof. Noritaka YUSA** **Graduate School of Engineering, Tohoku University, Sendai, Japan**
	**Prof. Masayuki TOKITANI** **National Institute for Fusion Science, Gifu, Japan**		

Abstract

Non-destructive testing is essential to ensure the long term safe and efficient operation of large-scale structures, such as fusion reactors. The divertor is one of the most critical engineering components in the fusion reactors and consists of a large number of tungsten blocks (tungsten monoblocks) that protect the heat removal components from intense thermal loads. Previous studies have reported that thermal loading from fusion plasma can cause fatigue cracks on monoblock surfaces. These cracks reduce the divertor's cooling performance and may result in the local melting of tungsten. Therefore, early detection and reliable evaluation of the cracks are necessary. Although eddy current testing can detect the cracks, it struggles to size deep cracks because the induced current does not sufficiently penetrate highly conductive tungsten. Ultrasonic testing, which is widely used for crack sizing, is also unsuitable for the vacuum environment of fusion reactors as it requires a liquid couplant. In contrast, the direct current potential drop (DCPD) technique is a promising method for evaluating the cracks on monoblocks. However, DCPD signals are sensitive to variations in the geometry of the monoblocks, uncertainty in the location of the cracks, and uncontrollable environmental factors (e.g., noise and variability in contact). These factors cause signal fluctuations that hinder uniform, deterministic evaluation, so a probabilistic approach is required to quantify the

uncertainty of the evaluation.

In this study, we develop a probabilistic crack-sizing framework based on a parallel ensemble model, which is used to estimate class probabilities of crack surface length and maximum depth from DCPD signals. The ensemble comprises of multiple shallow classification neural networks. Each network is trained using DCPD signals generated by 3D finite element simulations and augmented with uniform noises at various levels that emulate measurement and evaluation errors. The final output is obtained by averaging the class probabilities across these networks, enabling robust estimation under unknown noise levels. The proposed method is validated using test DCPD signals using brass specimens with machined slits that mimic the monoblock cracks. Brass is selected here because its electrical conductivity is similar to that of tungsten. A direct current is injected through two surface terminals, and the test DCPD signals are measured using ten electrodes across the slit. The results demonstrate that the proposed method successfully estimates both slit geometries and uncertainty as a probability distribution, with the estimated slit geometries being particularly close to those in the specimens for deep slits.

Evaluation of Natural Rubber Crystallization Effect on Variation in Elastocaloric Coefficient

ELyT Global

Theme: Energy

Scientific topic: Materials and Structures Design

			
Takuma OIRI[a,b]	Gildas COATIVY[c]	Gaël SEBALD[d]	Atsuki KOMIYA[b,d]

[a] *Graduate School of Engineering, Tohoku University, Japan*
[b] *Institute of Fluid Science, Tohoku University, Sendai, Japan*
[c] *INSA Lyon, LGEF, UR682, Villeurbanne, France*
[d] *ELyTMaX IRL 3757, CNRS, Univ. Lyon, INSA Lyon, Centrale Lyon, Université Claude Bernard Lyon 1, Tohoku University, Sendai, Japan*

Abstract

Cooling technology is essential in many industrial fields, and is particularly for food storage and human life. The most common cooling technology is the vapor compression refrigeration system, which contains a series of refrigerants such as freons. However, refrigerants previously used have significant toxicity issues and cause major environmental problems such as ozone layer destruction and global warming. Therefore, development is underway for freon-free cooling systems with low ozone destruction potential, low global warming potential, and no adverse effects on human health. As freon-free cooling systems, materials demonstrating caloric effects have drawn attention. Caloric effects are a phenomenon where heat generation or absorption occurs by changing a change of external magnetic field, electric field, or mechanical stress. Specifically, these include the magnetocaloric effect, electrocaloric effect, barocaloric effect, and elastocaloric effect. This study adopted the elastocaloric effect Among these, research on cooling systems using shape memory alloys is actively conducted, showing substantial temperature increases. However, they have disadvantages such as requiring very large forces and having short fatigue lifetimes. Conversely, cooling systems using the elastocaloric effect of natural rubber hold great potential as environmentally friendly materials due to their low cost and small tensile stress.

Previous research has demonstrated a cooling method combining the elastocaloric effect of natural rubber with a working fluid to transport heat to a heat exchanger [1]. This converts the thermal response generated by the natural rubber into a spatial temperature gradient between high and low-temperature regions. However, the optimal temperature conditions and elongation for this cooling system remain unclear. Therefore, this study focuses on the elastocaloric

coefficient, a coefficient representing the entropy change associated with natural rubber deformation. This is because the temperature difference generated by the elastocaloric effect is likely significantly influenced by the elastocaloric coefficient. The temperature and elongation dependency of the elastocaloric coefficient are shown in Figure 1. The figure reveals that the elongation at which the elastocaloric coefficient increases sharply becomes larger as the temperature increases. A change in the internal structure is considered a possible reason for this change. Therefore, this study clarified the relationship between the variation of the elastocaloric coefficient and crystallization. By using room temperature as a parameter, hysteresis and Young's modulus were determined, and experimental evaluation was performed.

The stress-strain curve for natural rubber is shown in Figure 2. Natural rubber was heated using a heater, and one cycle of stretch and relax was conducted at a very low strain rate. The figure shows that as the temperature increases, the stress difference between stretch and relax for the same elongation decreases, indicating that hysteresis, which represents delays in crystallization and melting, becomes smaller. This suggests that at high temperatures, increased molecular motion makes crystals easier to melt, preventing the formation of crystalline structures. Furthermore, it was confirmed that at higher temperatures, no plateau region occurs in either the stretch or relaxation processes. This suggests that the latent heat released during crystallization cancels out the stress increase due to entropy. Comparing Figures 1 and 2, the elongation where the plateau began to form corresponded to the elongation where the elastocaloric coefficient increased sharply. Therefore, the sharp increase in the elastocaloric coefficient can be explained as an effect of strain-induced crystallization.

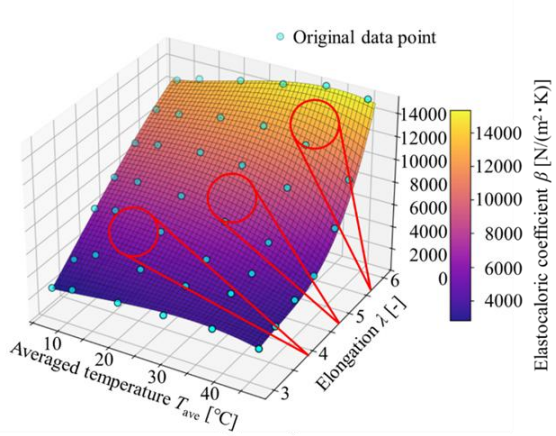

Fig. 1 Temperature and elongation dependency of the elastocaloric coefficient

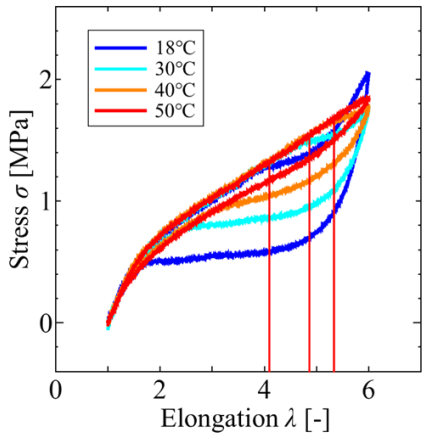

Fig. 2 Stress-strain curve using room temperature as a parameter.

Acknowledgement

This experiment was supported by LGEF, INSA Lyon, France.

Reference

[1] Sebald G, Lombardi G, Coativy G, Jay J, Lebrun L, Komiya A, Appl. Therm. Eng., 223, (2023), 120016.

Annealing the Adhesive Film Increases the Local Shear Stiffness of the Formula SAE Carbon Monocoque Without Increasing Weight.

ELyT Global

***Effects of HLEBI to Polymers & its Composites**
****HLEBI Induced Adhesive force of CF/Polymers**

Tsubasa Nakayasu [*], **Helmut Takahiro UCHIDA**[*], **Kousuke SAGAWA**[*], **Hideki KIMURA**[*],

[*]**Tokai University**, 〒259-1292, 4-1-1, Kitakaname, Hiratsuka, Kanagawa, **Japan.** #Tokyo City Univ. **Japan.** [$]Case Western Reserve University, **USA**

Michael C. Faudree[*#$], **Michelle Salvia**[@], **Jean-Yves Cavaille**[+], **Yoshitake Nishi**[*@+].

[@]**Ecole Centrale de Lyon**, Ecully Cedex 69134, **France**.
[+]**INSA Lyon**, *Bât. B. Pascal, 5° étage, 7, Avenue Jean Capelle, 69621 Villeurbanne cedex,* **France**

Abstract

In recent years, technological innovations in aerodynamics and power units have been remarkable, significantly increasing top cornering speeds.[1,2] Under these circumstances, reducing the weight of carbon monocoques and improving their safety performance are urgent issues. Conventional approaches to improve safety have relied on increasing the amount of carbon fiber used [3,4]. However, this approach inherently increases the overall weight, creating a fundamental design trade-off. By using a bond film that had been annealed at 36.5°C to bond CFRP and aluminum honeycomb and form a panel, we confirmed that the rigidity improvement rate in the elastic deformation region under shear load was twice. The toughening of the carbon panel due to this treatment is thought to be due to the smoothing of the adhesive film surface caused by the annealing treatment. As a result of introducing five research results, including this one, we succeeded in reducing the weight by 16 kg with a monocoque of the same shape, and won first place in the Best Composite Award [5].

1. Introduction

Electron beam irradiation of bond film is a promising method for improving rigidity in the low-load region (elastic deformation region) during shear testing. Shear test results confirmed that electron beam irradiation of bond film improved rigidity in the elastic deformation region by 40 percent without any change in the weight of the panel itself. In this study, we focus on the temperature increase, a secondary effect of electron beam irradiation, and investigate whether annealing can achieve a similar effect. Annealing can be performed using simple heating equipment, and is expected to shorten processing time, reduce costs, and be applicable to large components. Furthermore, by elucidating the effects of molecular chain reorientation and residual stress relaxation caused by heat treatment on material properties, we aim to propose a new method for improving the adhesive interface properties of CFRP.

2. Experimental Procedure

2.1 Sample preparation Sandwich panel specimen's representative of actual Formula SAE vehicle monocoques were fabricated using 3K twill prepreg (Daiko Shokai), thermosetting adhesive Bond Film (GH Craft), and aluminum honeycomb core (Suzuei Co., Ltd.). The CFRP prepreg employed in this work featured a 3K twill weave structure with a resin content of 42%, a thickness of 0.37 mm, and an areal density of 200 g/m^2. These specifications conform to the standard materials used in Formula SAE monocoque manufacturing, providing an optimal balance of mechanical properties and formability. The adhesive Bond Film is characterized by a curing temperature of 130°C, a basis weight of 300 g/m^2, and a thickness of 0.06 mm. It is supplied in 50-inch (1270 mm) wide rolls. The aluminum honeycomb core was AL1/8-5052-.001 grade, exhibiting a density of 0.072 g/cm^3, a compressive strength of 4.5 MPa, and a shear strength of 0.7 MPa. In selecting materials, we

chose a combination that would achieve both light weight and formability while ensuring safety performance in accordance with Formula SAE regulations. The CFRP The CFRP laminate fiber orientation followed a quasi-isotropic layup [0°/±45°/90°], while the honeycomb core thickness of 20 mm represents the standard specification used in actual racing vehicles. This material configuration was selected to accurately reproduce the structural characteristics of production monocoque designs.

To prepare the specimen, we first placed a 3K twill prepreg as the CFRP primary laminate in bagging film and heat-cured it in a vacuum at 120°C for two hours. The baked CFRP primary laminate, aluminum honeycomb, and CFRP secondary laminate were then attached using the Bond Film. The assembly was then vacuum-bagged and heat-cured for an additional two hours to complete specimen preparation.

2.2. Annealing of Bond Film The annealing protocol was designed to minimize adverse effects from thermal shock while allowing sufficient time for molecular relaxation. A controlled temperature ramp rise rate of 1°C/min. was employed to ensure gradual heating. The target temperature of 36.5°C was selected to remain below the glass transition temperature, thereby modifying surface characteristics without significantly altering the bulk molecular structure of the resin.

2.3. Mechanical Testing In the tests, specimens containing bond film irradiated with electron beams and specimens containing annealed bond film were used to measure the response to punching loads, as well as shear strength and fracture load. The test data will be useful for evaluating the reliability of CFRP components under local load conditions and for formulating design guidelines, contributing to improving performance and ensuring safety in the structural use of CFRP. Test specimens were 120 mm x 120 mm, with a punch diameter of 25mm, and the test was performed at a test speed of 0.01 mm/s.The Shimadzu AGX-100kNX Plus testing machine was used, as was the case for the three-point bending and shear tests.

3.Experimental Results & Discussion

Low-temperature annealing at 36.5°C demonstrated significant improvements in shear stiffness within the elastic deformation region during punching shear testing compared to untreated controls (Fig. 1). Notably, no significant change in bending stiffness was observed in three-point bending tests. The selective improvement in shear stiffness without corresponding enhancement in bending stiffness strongly suggests that the mechanism involves improvements in the interfacial adhesive bond strength between the skin and core rather than bulk material property changes. Surface observations using a stereomicroscope and SEM confirmed that the surface irregularities seen in the untreated sample were smoothed out in the sample after low-temperature annealing. It is presumed that a reduction in voids at the adhesive interface and an increase in the effective adhesive area resulted in an improvement in the interfacial shear strength between the skin and core. Based on the successive results, we got the Best Composite Award, on Sept. 13th, 2025, as shown in Fig.1.

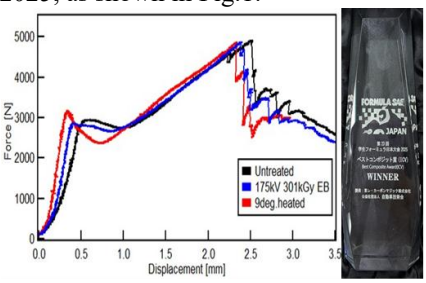

Fig.1 Shear load-displacement curves with the prize of '**FORMULA SAE.JAPAN**' -"**Best Composite Award (ICV) WINNER**" Supported by Toray Carbon Magic Co. Ltd. [TCM] & Society of Automotive Engineers of Japan Inc. [JSAE]

4.Conclusion

Punching shear testing of annealed specimens demonstrated a 0.27 mm reduction in maximum displacement within the elastic deformation region, corresponding to twice improvement in rigidity compared to untreated controls. Microstructural analysis via stereomicroscopy and SEM confirmed that the visible surface roughness present in untreated samples was eliminated following annealing treatment, yielding a smooth, uniform surface morphology. Since the annealing temperature remains below the glass transition temperature, the observed surface modification is attributed to low-temperature viscous flow of the adhesive film without inducing crystallization. This thermal treatment promotes surface planarization while preserving the amorphous structure and bulk mechanical properties of the adhesive.

References

[1] Dallara Automobili, Altair. Speed and Safety: Composite Materials in Motorsport. 2012.
[2] L. Hamilton *et al*., "Production of a Composite Monocoque Frame For a Formula SAE Racecar.", SAE International, (2013), *SAE Technical Paper*, 2013-01-1173.
[3] A. Mizutani and Y. Nishi, "Improved Strength in Carbon Fiber Reinforced Plastics due after Electron Beam Irradiation", *Mater. Trans*., **44**, (2003); 1857.
[4] Y. Kajiwara, "Structure Property: Joining Techniques for CFRP.", *Seikei-Kakou*, **33**, (2021), 235-238.
[5] "Tokai Formula Club" won the "Best Composite Award" for the first time at the Student Formula SAE Competition in Japan."(Article in Japanese) https://www.u-tokai.ac.jp/news-challenge/1357111/ (Accessed on 2025/12/10)

A Molecular Dynamics Approach to Computing the Work of Adhesion at Various Surfaces

Molecular Dynamics, Wetting

	**T. Tanaka** **Institute of Fluid Science, Graduate School of Engineering, Tohoku University**		**Assoc. Prof. D. Surblys** **Institute of Fluid Science, Tohoku University**		**Prof. T. Ohara** **Institute of Fluid Science, Tohoku University**

Abstract

The work of adhesion is a fundamental thermodynamic quantity that characterizes the wettability of solid–liquid interfaces and plays a key role in many technologies, including coatings, nanofluidics, and surface functionalization. Molecular dynamics (MD) simulations are widely used to investigate wetting behavior at the nanoscale. Traditionally, wettability has been evaluated by simulating liquid droplets on solid surfaces and measuring the contact angle [1]. However, droplet-based approaches require large simulation systems and long computation times, and they suffer from intrinsic ambiguity on heterogeneous or structurally complex surfaces, where the contact angle is not uniquely defined.

An alternative approach is to evaluate wettability through the work of adhesion, which can be calculated directly from interfacial free energy changes. Thermodynamic integration [2] provides a framework for computing free energy differences by integrating the ensemble average of the derivative of the Hamiltonian with respect to a coupling parameter. One established implementation is the phantom-wall (PW) method [3], in which a virtual repulsive wall that interacts only with the liquid phase is introduced to reversibly separate the liquid from the solid surface. The work of adhesion, W_{adh}, is evaluated from the free-energy change associated with this separation process. In this method, W_{adh} is obtained by integrating the pressure exerted on the wall, $p_{\mathrm{w}}(z)$, with respect to its position, z, and is expressed as

$$W_{\mathrm{adh}} = \int_{z_0}^{z_1} p_{\mathrm{w}}(z)\, dz - \frac{p\Delta V}{A} \tag{1}$$

where p is the system pressure, ΔV is the change in system volume during the separation, and A is the cross-sectional area of the simulation cell. The parameters z_0 and z_1 denote the initial and final positions of the wall, respectively.

Despite its simplicity, the conventional PW method has notable limitations. Because the liquid is completely detached from the solid surface, a vacuum forms during the separation process, neglecting effects from vapor pressure or adsorption layer. Moreover, the method is difficult to apply to complex interfaces where the solid and liquid phases are not clearly separable, such as

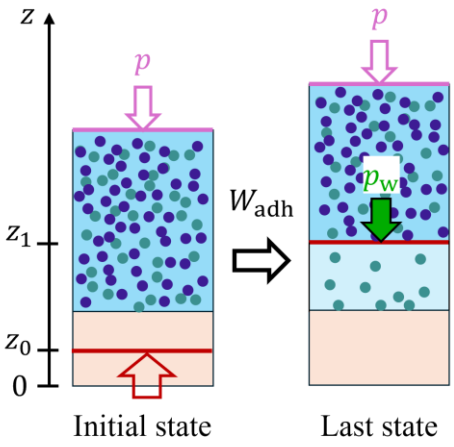

Fig. 1. Schematic of the caluculation of the work of adhesion using a partially permeable phantom wall. Blue dots represent the fluid molecules interacting with the wall, while green dots represent molecules permeating thtough the wall.

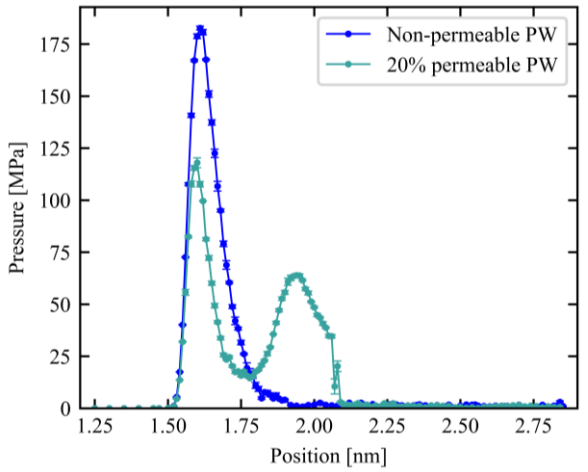

Fig. 2. Pressure exerted on the phantom wall as a function of wall position for the Pt–Ar solid–liquid interface, obtained using non-permeable and partially permeable phantom walls.

surfaces modified by molecular layers into which liquid molecules can penetrate.

In this study, we extended the PW method by introducing a partially permeable phantom wall that interacts with only a fraction of the liquid molecules. By allowing some molecules to pass through the wall, the separation process becomes more flexible and physically realistic. We first applied this method to a simple flat-surface Pt–Ar system and systematically examined both weak and strong solid–fluid interaction regimes. For weak interactions, we demonstrated that the work of adhesion can be evaluated using a partially permeable wall with accuracy comparable to that of the conventional non-permeable PW method. Even in the strong interaction (complete wetting) case, the method remains applicable by appropriately adjusting the fraction of liquid molecules permeating through the wall, as demonstrated by the pressure–position profiles shown in Fig. 2.

We then applied the partially permeable PW method to a more complex solid–liquid interface: a water system in contact with an Au surface modified by self-assembled monolayers (SAMs), using the model reported by Imaizumi et al. [4]. In this system, water molecules can penetrate into the SAM layer, making the conventional PW method unsuitable. The proposed method enables the calculation of the work of adhesion while leaving the water molecules inside the SAM intact, thereby preserving the essential interfacial structure.

These results demonstrate that the partially permeable phantom-wall method significantly broadens the applicability of thermodynamic integration for computing the work of adhesion. The approach provides a robust and versatile framework for evaluating wettability at both simple and structurally complex solid–liquid interfaces using molecular dynamics simulations.

References

[1] H. Jiang and A. J. Patel, *Curr. Opin. Chem. Eng.*, vol. 23, pp. 130–137, (2019).
[2] F. Leroy, D. J. V. A. dos Santos, and F. Müller-Plathe, *Macromol. Rapid Commun.*, vol. 30, no. 9–10, pp. 864–870, (2009).
[3] F. Leroy and F. Müller-Plathe, *J. Chem. Phys.*, vol. 133, no. 4, p. 044110, (2010).
[4] T. Imaizumi *et al.*, *Langmuir*, vol. 41, no. 27, pp. 18200–18212, (2025).

Transition of Momentum Transport Pathways under Shear: A Molecular Dynamics Insights

ELyT Global

Theme: Molecular dynamics

Scientific topic: Momentum transport

		
Masaharu YOSHIDA[a, b]	Donatas SURBLYS[a]	Taku OHARA[a]

[a] *Institute of Fluid Science, Tohoku University, 980-8577, Sendai, Japan*

[b] *Graduate School of Engineering, Tohoku University, 980-8579, Sendai, Japan*

Abstract

Small-molecule liquids can exhibit non-Newtonian behavior such as shear thinning at high shear rates, yet the microscopic origin of this nonlinear viscosity response remains less understood than in simple monatomic fluids or entangled polymer melts. In particular, how molecular structure reorganizes momentum transport pathways under shear is still unclear. Molecular dynamics (MD) simulations provide a powerful framework to address this issue, as they enable direct access to microscopic stress, molecular configurations, and momentum transport under controlled shear conditions. This study aims to clarify the molecular-scale mechanisms governing shear dependent viscosity in liquids with intermediate molecular complexity.

Equilibrium and non-equilibrium molecular dynamics (EMD and NEMD) simulations were performed for liquids with different molecular rigidity and chain length, including H_2O, C_6H_6, and linear alkanes (C_4H_{10}, C_8H_{18}, $C_{16}H_{34}$). Shear viscosities were evaluated under zero-shear and steady-shear conditions, and the stress was decomposed into molecular-scale momentum transport contributions, such as kinetic, intra-molecular (bond, angle, dihedral, etc.), and inter-molecular components (van der Waals, Coulomb). To directly relate macroscopic rheology to microscopic rearrangements, shear-induced anisotropy of local structure and momentum transport was analyzed using two-dimensional radial distribution functions and spatially resolved momentum transport (shear stress) maps on an r–θ framework.

As a result, molecular-level momentum transfer mechanisms contributing to viscosity and it's non-linear response to shear were eculcidated. In $C_{16}H_{34}$, increased molecular anisotropy under shear leads to a reorganization of momentum transport pathways, characterized by a decrease in intra-molecular contributions and an increase in inter-molecular contributions.

AI-assisted symmetry-informed topology optimization of woven materials for broadband sound absorption
Acronym of the ELyT project MuORode

ELyT Global

Project ELyT lab: R7 – Robust Multi Objective optimization design approaches

	**Koji SHIMOYAMA[1]**		**Frédéric GILLOT[2]**
	**Hiroshi, SUITO[3]**		**Sébastien BESSET[2]**
	**Sonia MAHMOUDI[3,4]**		**Thanasak, WANGLOMKLANG[2]**

[1] *Department of Mechanical Engineering, Kyushu University, Japan*

[2] *Ecole Centrale de Lyon, LTDS DySCo Team, Lyon, France*

[3] *Advanced Institute for Materials Research, Mathematical Science Group, Tohoku University, Japan*

[4] *RIKEN, Center for Interdisciplinary Theoretical and Mathematical Sciences (iTHEMS), 2-1, Hirosawa, Wako, Saitama 351-0198, Japan*

Abstract

This work presents an AI-assisted, symmetry-informed framework for the inverse design of woven micro-structured materials aimed at achieving enhanced broadband sound absorption. The design space of binary woven topologies exhibits severe combinatorial growth, which hinders conventional optimization and random sampling approaches. To address this challenge, crystallographic wallpaper symmetries, feasibility constraints, and topological equivalence relations are embedded directly into the pattern generation process, enabling efficient and physically valid data generation. Acoustic performance is evaluated using numerical

simulations based on the Johnson–Champoux–Allard (JCA) equivalent fluid model coupled with finite element analysis. A semi-supervised convolutional autoencoder is developed to compress high-dimensional discrete topologies into a low-dimensional latent representation, which is subsequently used for surrogate modeling via Gaussian process regression. This hybrid learning strategy effectively leverages both limited labeled data and abundant unlabeled samples. The proposed approach enables rapid exploration of large design spaces and supports efficient optimization using genetic algorithms. Optimized woven patterns are obtained within short computational times, with FEM-validated prediction errors below 5%. The results demonstrate that symmetry-informed, constraint-aware artificial intelligence provides a scalable and interpretable pathway for the data-driven design of advanced acoustic materials with improved broadband absorption performance.

References:

[1] Wanglomklang, T., Shimoyama, K., Gillot, F., & Besset, S. (2025). Neural-network-based two stage robust shape optimization for acoustic noise reduction in an aircraft cabin. Engineering Optimization, 1–19.

[2] Wanglomklang, T., Gillot, F., Besset, S., and Mahmoudi, S. (2025). Vibro-Acoustic Modelisation of Periodic Woven Structures Dedicated to Multi-Objective Shape Optimization. ICFD 2025, Sendai, Japan, November 10-13, 2025.

Metamodel-based Robust Shape Optimization for Aircraft Cabin Noise Reduction
Acronym of the ELyT project MuORode

ELyT Global

Project ELyT lab: R7 – Robust Multi Objective optimization design approaches

	**Koji SHIMOYAMA[1]**		**Frédéric GILLOT[2]**
	**Hiroshi, SUITO[3]**		**Sébastien BESSET[2]**
	**Sonia MAHMOUDI[3,4]**		**Thanasak, WANGLOMKLANG[2]**

[1] *Department of Mechanical Engineering, Kyushu University, Japan*

[2] *Ecole Centrale de Lyon, LTDS DySCo Team, Lyon, France*

[3] *Advanced Institute for Materials Research, Mathematical Science Group, Tohoku University, Japan*

[4] *RIKEN, Center for Interdisciplinary Theoretical and Mathematical Sciences (iTHEMS), 2-1, Hirosawa, Wako, Saitama 351-0198, Japan*

Abstract

This study presents a metamodel-based robust shape optimization framework for aircraft cabin noise reduction under mid–high frequency vibro-acoustic excitation. Under cruise conditions, turbulent boundary layer (TBL) pressure fluctuations induce structural vibrations that are transmitted through acoustic treatment layers into the cabin, where noise levels are highly sensitive to geometric uncertainties. These uncertainties significantly affect acoustic performance and limit the reliability of conventional deterministic optimization approaches. To address this challenge, a mid–high frequency modeling strategy based on the Simplified Energy Method (SEM) is employed to capture steady-state energy transport and dissipation in coupled structural–acoustic systems. Both differential and integral SEM formulations are used to

describe vibro-acoustic coupling between the fuselage structure and the three-dimensional cabin cavity. Free-form deformation is adopted for geometric parameterization, enabling flexible and efficient shape control. A Gaussian process regression model is constructed to approximate the acoustic response and quantify uncertainty, allowing rapid evaluation of performance statistics, including mean and standard deviation. These metrics are incorporated into a robust multi-objective optimization framework to identify designs that balance noise reduction and robustness. Numerical results demonstrate that the optimized cabin shapes achieve improved acoustic performance while maintaining robustness against geometric variations, providing a practical pathway for industrial-scale vibro-acoustic design.

References:

[1] Wanglomklang, T., Shimoyama, K., Gillot, F., & Besset, S. (2025). Neural-network-based two stage robust shape optimization for acoustic noise reduction in an aircraft cabin. Engineering Optimization, 1–19.

[2] Wanglomklang, T., Gillot, F., Besset, S., and Mahmoudi, S. (2025). Vibro-Acoustic Modelisation of Periodic Woven Structures Dedicated to Multi-Objective Shape Optimization. ICFиD 2025, Sendai, Japan, November 10-13, 2025.

Towards Large-Scale Realistic Cerebral Artery Generation

ELyT Global
Engineering for Health Simulation & Modeling

	**Vedhino Bima Aryaputra Ahnaf** Institute of Fluid Science, Graduate School of Engineering, Tohoku University, Japan.		**Kazuyoshi Jin** Institute of Fluid Science, Graduate School of Biomedical Engineering, Tohoku University, Japan.		**Dr. Jing Liao** Institute of Fluid Science, Tohoku University, Japan.
	**Yurika Doi** Institute of Fluid Science, Graduate School of Biomedical Engineering, Tohoku University, Japan.		**Carole Frindel** CREATIS, INSA Lyon, France.		**Odyssée Merveille** CREATIS, INSA Lyon, France.
	**Prof. Makoto Ohta** Institute of Fluid Science, Tohoku University, Japan.		**Dr. Hitomi Anzai** Institute of Fluid Science, Tohoku University, Japan.		.

Abstract

1. Introduction

Large-scale, realistic cerebral artery data are crucial for data-driven vascular modeling, medical AI, and device development. However, such datasets remain difficult to obtain due to ethical and cost constraints. Here, we focus on the internal carotid artery (ICA), a major cerebral inflow vessel and a representative target with substantial anatomical variability. Previous work has proposed Multivariate Normal Distribution (MVND)–based synthetic population generation to mitigate data scarcity [1], but it was demonstrated on a small dataset. As a result, it remains difficult to rigorously assess how realistic the generated ICAs are and whether they capture population-level variability. This motivates the use of a larger and more diverse parent dataset, together with scalable, automated evaluation methods for comparing large real and synthetic populations.

2. Method

We extend MVND-based synthetic population generation by leveraging a substantially larger (≈100×) and more diverse community cohort as the parent dataset. Synthetic ICA geometries (centerlines with corresponding diameter profiles) were generated, and geometric

descriptors (e.g., vessel length, tortuosity, and curvature-related metrics) were automatically extracted from both real and synthetic populations. Population-level distributions were evaluated separately for left and right ICAs using Kullback–Leibler (KL) divergence to preserve side-dependent morphology.

3. Result & Discussion

The proposed pipeline enabled automated, side-specific comparison between the real and synthetic populations. Similar trends were observed for both left and right ICAs: all descriptors showed low-to-moderate KL divergence, indicating good agreement between real and synthetic distributions. However, vessel length and tortuosity exhibited higher divergence, suggesting that global scale–related variability is harder to capture under the current MVND parameterization. This may be influenced by landmarking choices and the Gaussian assumption, which can underrepresent tail behavior in length-related features.

4. Conclusion

Using a larger cohort enabled the construction of a large-scale, statistically grounded synthetic ICA population that better captures population-level shape diversity under an MVND framework, providing a stronger foundation for downstream vascular research. Future work will incorporate additional segment-wise geometric descriptors to better capture local variability and will systematically examine how landmark placement in the MVND framework affects the resulting population distributions.

Acknowledgements

This work was supported by CNRS and Region Auvergne Rhône Alpes, and JSPS Core-to-Core Program (grant number: JPJSCCA20210005) and AMED under Grant Number JP23tm0524003.

REFERENCES

[1] Jin et al., Int J Numer Meth Biomed Eng, 2025

Strengthening and deformation mechanisms of high strength biodegradable Fe–10Mn alloy

ELyT Global

Theme (Engineering for Health)
Scientific topic (Materials & Structure Design)

	**Hiroya Ishii** **Biomedical Engineering, Tohoku University**		**Manami Mori** **National Institute of Technology, Sendai College**
	**Shigeo Sato** **Ibaraki University**		**Damien Fabregue** **Université de Lyon, INSA Lyon**
	**Kenta Yamanaka** **Institute for Materials Research, Tohoku university**		

Abstract

Conventional metallic biomaterials, such as stainless steels, Co−Cr alloys, and titanium alloys, possess excellent corrosion resistance but remain permanently in the human body. In contrast, biodegradable metals are attracting significant attention because they degrade in the body over time, thereby eliminating the long-term complications associated with permanent implants. However, a major challenge for current biodegradable metals is their inferior strength compared to conventional metallic biomaterials.

Fe−Mn alloys are promising candidates as they exhibit mechanical properties comparable to

stainless steel, with potential for strengthening via the transformation-induced plasticity (TRIP) effect [1]. Medium-Mn (5−10 wt.% Mn) steels have been extensively studied as Advanced High-Strength Steels (AHSS)[2], and their strengthening mechanisms could allow biodegradable alloys to surpass the strength of Co−Cr and titanium alloys. Achieving such high strength would extend the application of biodegradable metals to load-bearing devices, such as bone fixation plates. Although Maeda et al. [3] reported on the heterogeneous deformation behavior of these steels, the specific impact of hot rolling on these properties remains unclear. Therefore, the objective of this study is to elucidate the plastic deformation mechanism of this alloy, specifically examining the effects of hot rolling.

Ingots of Fe−10Mn−0.1C (mass%)alloys were prepared by induction melting. After homogenization treatment in vacuum at 1100 °C for 2 h, a 23 mm-diameter rod was subjected to hot-caliber rolling at 1100 °C to finally obtain a 7 mm-diameter rod (reduction in area: about 91 %), forrowed by air cooling. The microstructures of the specimen were observed by SEM, EBSD, STEM. In-situ neutron diffraction measurements during tensile deformation were conducted at the iMATERIA (BL20) beamline of J-PARC [4]. Dislocation density, crystallographic texture and phase fraction were quantitatively evaluated from the obtained diffraction spectra using the Convolutional Multiple Whole Profile (CMWP) fitting method [5] and Rietveld texture analysis (RTA) [6].

Fig. 1 shows a bright-field (BF) image of the Fe−10Mn alloy. A martensitic microstructure containing a high density of dislocations was observed. These defects were originally introduced into the parent austenite phase during severe hot rolling and were subsequently inherited by the martensite. This high density of dislocations is considered to contribute significantly to the strengthening of the alloy [7].

Fig. 2 shows the evolution of phase fractions during tensile deformation, evaluated by RTA. The fraction of ε martensite, which was initially approximately 25%, decreased to less than 5% at fracture. Conversely, the fraction of α’ martensite increased with deformation. These results suggest the occurrence of strain-induced ε to α’ martensitic transformation.

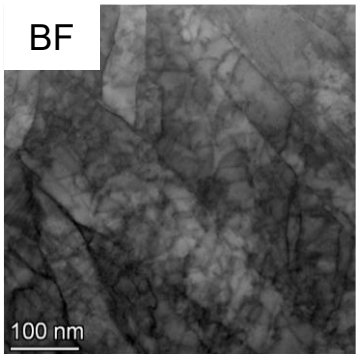

Fig. 1 BF image of the hot-rolled Fe−10Mn alloy.

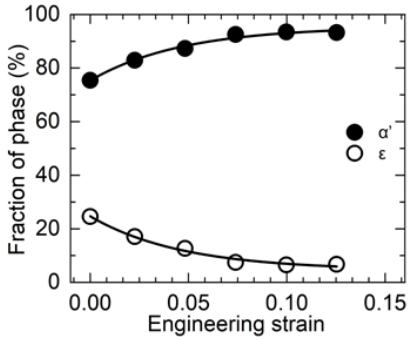

Fig. 2 Evolution of phase fractions during tensile deformation as evaluated by RTA.

[1] H. Hermawan et al., Advanced Materials Research, 15-17 (2007) 107-122.
[2] B. Hu et al., Journal of Materials Science & Technology, 33 (2017) 1457-1464
[3] T. Maeda et al., Tetsu-to-Hagane, 110 (2024) 268-278.
[4] Y. Onuki et al., Journal of Applied Crystallography, 49 (2016) 1579-1584.
[5] K. Yamanaka et al., Additive Manufacturing, 37 (2021) 101678.
[6] Y. Onuki et al., Quantum Beam Science, 2 (2018) 11.
[7] I. Tamura, Transactions of the Iron and Steel Institute of Japan, 6 (1966) 249-262.